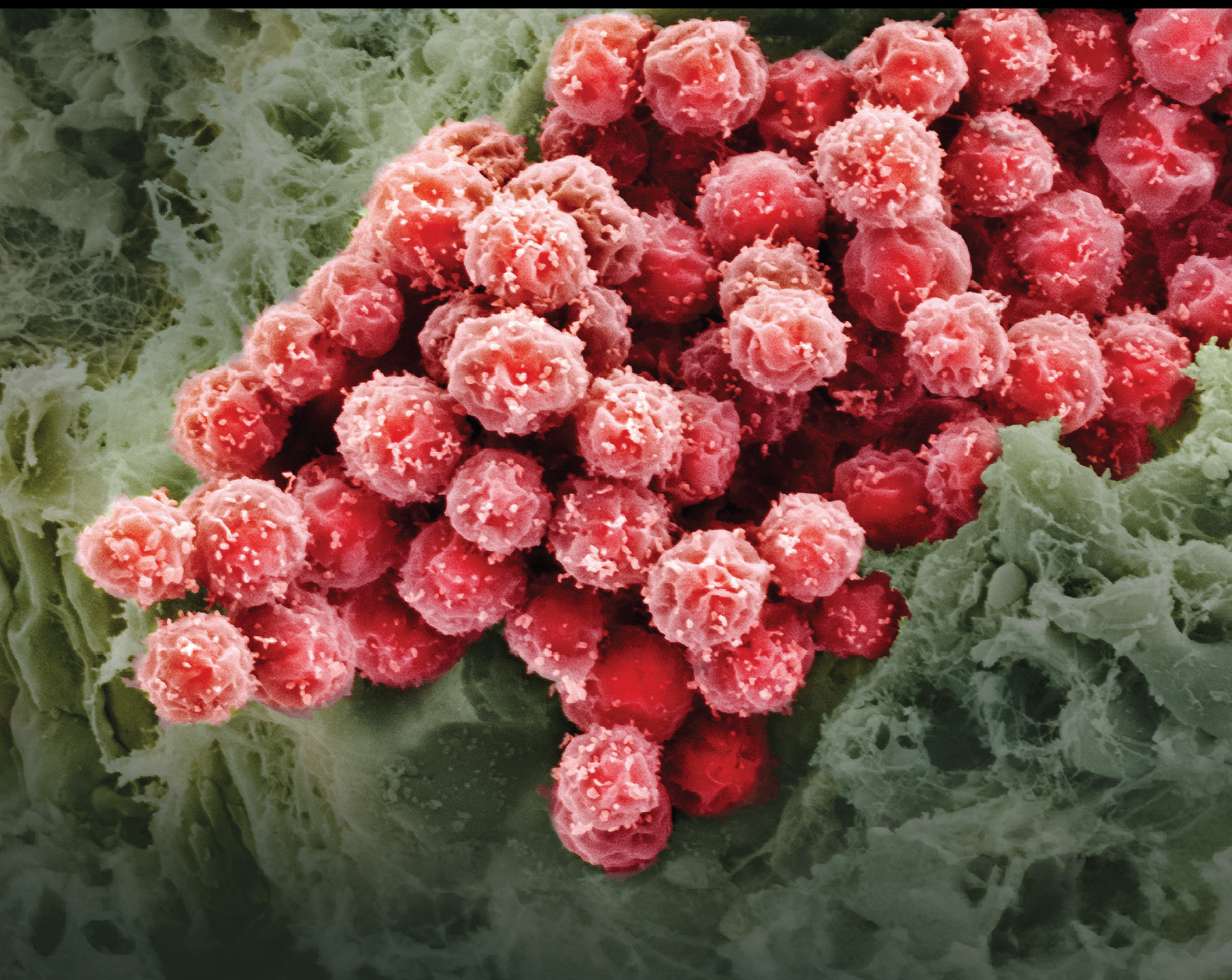


Regenerative Medicine Approaches for Lung Tissue Regeneration

Lead Guest Editor: Nicholas R. Forsyth

Guest Editors: Wei Zuo and Ying Yang





Regenerative Medicine Approaches for Lung Tissue Regeneration

Stem Cells International

Regenerative Medicine Approaches for Lung Tissue Regeneration

Lead Guest Editor: Nicholas R. Forsyth

Guest Editors: Wei Zuo and Ying Yang







Copyright © 2022 Hindawi Limited. All rights reserved.

This is a special issue published in “Stem Cells International.” All articles are open access articles distributed under the Creative Commons Attribution License, which permits unrestricted use, distribution, and reproduction in any medium, provided the original work is properly cited.



Chief Editor

Renke Li , Canada

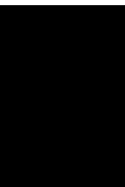
Associate Editors




James Adjaye , Germany
Andrzej Lange, Poland
Tao-Sheng Li , Japan
Heinrich Sauer , Germany
Holm Zaehres , Germany

Academic Editors

Cinzia Allegrucci , United Kingdom
Eckhard U Alt, USA
Francesco Angelini , Italy
James A. Ankrum , USA
Stefan Arnhold , Germany
Marta Baiocchi, Italy
Julie Bejoy , USA
Philippe Bourin , France
Benedetta Bussolati, Italy
Leonora Buzanska , Poland
Stefania Cantore , Italy
Simona Ceccarelli , Italy
Alain Chapel , France
Sumanta Chatterjee, USA
Isotta Chimenti , Italy
Mahmood S. Choudhery , Pakistan
Pier Paolo Claudio , USA
Gerald A. Colvin , USA
Joery De Kock, Belgium
Valdo Jose Dias Da Silva , Brazil
Leonard M. Eisenberg , USA
Alessandro Faroni , United Kingdom
Ji-Dong Fu , USA
Marialucia Gallorini , Italy
Jacob H. Hanna , Israel
David A. Hart , Canada
Zhao Huang , China
Elena A. Jones , United Kingdom
Oswaldo Keith Okamoto , Brazil
Alexander Kleger , Germany
Laura Lasagni , Italy
Shinn-Zong Lin , Taiwan
Zhao-Jun Liu , USA
Valeria Lucchino, Italy
Risheng Ma, USA
Giuseppe Mandraffino , Italy

Katia Mareschi , Italy
Pasquale Marrazzo , Italy
Francesca Megiorni , Italy
Susanna Miettinen , Finland
Claudia Montero-Menei, France
Christian Morszeck, Germany
Patricia Murray , United Kingdom
Federico Mussano , Italy
Mustapha Najimi , Belgium
Norimasa Nakamura , Japan
Karim Nayernia, United Kingdom
Toru Ogasawara , Japan
Paulo J Palma Palma, Portugal
Zhaoji Pan , China
Gianpaolo Papaccio, Italy
Kishore B. S. Pasumarthi , Canada
Manash Paul , USA
Yuriy Petrenko , Czech Republic
Phuc Van Pham, Vietnam
Alessandra Pisciotta , Italy
Bruno P#ault, USA
Liren Qian , China
Md Shaifur Rahman, Bangladesh
Pranela Rameshwar , USA
Syed Shadab Raza Raza , India
Alessandro Rosa , Italy
Subhadeep Roy , India
Antonio Salgado , Portugal
Fermin Sanchez-Guijo , Spain
Arif Siddiqui , Saudi Arabia
Shimon Slavin, Israel
Sieghart Sopper , Austria
Valeria Sorrenti , Italy
Ann Steele, USA
Alexander Storch , Germany
Hirotaka Suga , Japan
Gareth Sullivan , Norway
Masatoshi Suzuki , USA
Daniele Torella , Italy
H M Arif Ullah , USA
Aijun Wang , USA
Darius Widera , United Kingdom
Wasco Wruck , Germany
Takao Yasuhara, Japan
Zhaohui Ye , USA



Shuiqiao Yuan , China
Dunfang Zhang , China
Ludovic Zimmerlin, USA
Ewa K. Zuba-Surma , Poland




Contents

Fabrication and Characterization of Alveolus-Like Scaffolds with Control of the Pore Architecture and Gas Permeability

Lanxin Lü , Hongxian Shen, Daichi Kasai, and Ying Yang 


Research Article (12 pages), Article ID 3437073, Volume 2022 (2022)

Spidroin-Based Biomaterials in Tissue Engineering: General Approaches and Potential Stem Cell Therapies

Qi Zhang , Min Li , Wenbo Hu, Xin Wang, and Jinlian Hu 

Review Article (16 pages), Article ID 7141550, Volume 2021 (2021)

Stable Long-Term Culture of Human Distal Airway Stem Cells for Transplantation

Yueqing Zhou, Yujia Wang, Dandan Li, Ting Zhang, Yu Ma, and Wei Zuo 

Research Article (11 pages), Article ID 9974635, Volume 2021 (2021)

Research Article

Fabrication and Characterization of Alveolus-Like Scaffolds with Control of the Pore Architecture and Gas Permeability

Lanxin Lü ¹, Hongxian Shen,¹ Daichi Kasai,² and Ying Yang ^{2,3}

¹Emergency Center of the Affiliated Hospital of Xuzhou Medical University, Laboratory of Emergency Medicine, Xuzhou Medical University, Xuzhou 221002, China

²School of Pharmacy and Bioengineering, Keele University, Stoke-on-Trent ST4 7QB, UK

³School of Life Sciences, Guangzhou University, Guangzhou, China

Correspondence should be addressed to Ying Yang; y.yang@keele.ac.uk

Received 27 May 2021; Accepted 30 December 2021; Published 20 January 2022

Academic Editor: Andrea Ballini

Copyright © 2022 Lanxin Lü et al. This is an open access article distributed under the Creative Commons Attribution License, which permits unrestricted use, distribution, and reproduction in any medium, provided the original work is properly cited.

The micrometer scale sac-like alveoli are the most important and essential unit for gas exchange in the lung. Thus, design and fabrication of scaffolds for alveoli regeneration by tissue engineering approach should meet a few topography and functional requests such as large surface area, flexibility, and high gas permeability to their native counterpart. Testing the gas permeability of scaffolds through a fast and simple technique is also highly demanded to assist new scaffold development. This study fabricated alveolus-like scaffolds with regular pore shape, high pore connectivity, and high porosity produced by inverse opal technique alongside randomly distributed porous scaffolds by salt leaching technique from two different materials (polyurethane and poly(L-lactic acid)). The scaffold surface was modified by immobilization of VEGF. A facile and new technique based on the bubble meter principle enabling to measure the gas permeability of porous scaffolds conveniently has been developed specifically. The cellular response of the scaffolds was assessed by culturing with bone marrow mesenchymal stem cells and coculturing with lung epithelial NL20 and endothelial HUVECs. Our results showed that the newly designed gas permeability device provided rapid, nondestructive, reproducible, and accurate assessment of gas permeability of different scaffolds. The porous polyurethane scaffolds made by inverse opal method had much better gas permeability than other scaffolds used in this study. The cellular work indicated that with VEGF surface modification, polyurethane inverse opal scaffolds induced alveolus-like tissues and have promising application in lung tissue engineering.

1. Introduction

The prevalence of lung diseases has been increasing because of smoking, air pollution (high dust and chemical particles in air), and genetic disorders [1]. Chronic obstructive pulmonary disorder (COPD), acute lung injury/acute respiratory distress syndrome (ALI/ARDS), pulmonary hypertension (PH), cystic fibrosis (CF), and lung cancer are among the lung diseases with high mortality [2–6]. However, human lungs have very limited capacity to regenerate. Once the lung is subjected to damage or degeneration, the function of the lung will undergo irreversible impairment. Lung tissue transplantation is the gold standard for treating damaged lungs and helping to save lives. It is an effective and safe therapy for the patients suffering from a variety of end-stage

pulmonary diseases. Meanwhile, more than 50,000 adult lung transplants have been entered into the International Society of Heart and Lung Transplantation Registry by 2014 [7]. However, this treatment faces big challenges: shortage of donor organs, expensive surgery, and short transplant life due to chronic lung allograft dysfunction, along with the recurrence of the underlying pathology in some cases [8]. The late mortality following lung transplantation presents in approximately 50% of patients at 5 years after transplantation [7]. Therefore, tissue engineering approach which is able to generate biologically compatible substitutes to restore and support lung tissue functions [9] becomes a very promising therapy.

Good gas permeability is the key feature of the lung. Alveoli are the basic and essential unit of gas exchange.

Scaffolds for alveoli regeneration through tissue engineering approach should have multiple connective pores and excellent gas permeability in the pore wall. Many scaffolds, such as decellularized, Gelfoam sponge, and collagen microcapsule [10–12], have been explored to fabricate tissue engineering lung with growing lung cells such as epithelial and endothelial cells in them. Previously, inverse opal scaffolds with uniform and controllable pore size, high pore connectivity, and thin pore wall were employed to investigate the blood vessel infiltration [13]. The structural features of inverse opal scaffolds can mimic topographic alveoli of the lung and make itself a promising scaffold candidate for lung tissue engineering.

To characterize whether a scaffold is suitable for alveoli production, gas permeability tests should be undertaken. A few reliable gas permeability testers for food packaging, textiles, and papers are available based on the manometer principle and ASTM standards, for example, the Permeance Testing Device, type GDP-C; Differential Pressure Air Permeability tester, Frazier; and ASTM 1434-82 and ASTM D737 [14, 15]. However, they are not suitable for testing the gas permeability of porous scaffolds in tissue engineering due to their small bulk size, relatively large pore, and unique architecture [16, 17]. Considering the high gas permeability of porous scaffolds, the high-precision flowmeter of gas is needed in gas measurement of the test. Levy reported the bubble meter technique as a simple but reliable method of measuring the volume flow rate of gases in application [18]. The aim of the current study is to fabricate and compare multiple alveolus-like scaffolds used for lung tissue engineering and design a convenient and facile device capable of testing the gas permeability of these produced scaffolds in order to guide better fabrication of alveolus-like scaffolds.

2. Materials and Method

2.1. Fabrication of Alveolus-Like Scaffolds. Two types of porous scaffolds with different architectures were fabricated. One type was gelatin-based inverse opal scaffolds with uniform pore structures, denoted as IOS, and the other one was salt leaching porous scaffolds with randomly distributed pore structures, denoted as SLS. Two types of polymers, polyurethane (PU) (Sigma-Aldrich, US) and poly(L-lactic acid) (PLLA) (Purac BV, Gorinchem, the Netherlands) have been used to fabricate the scaffolds.

IOS scaffolds were generated following the established protocol with slight modification as shown in Figure 1 [13]. Firstly, uniform gelatin microspheres with sizes ranging from $180\ \mu\text{m}$ to $430\ \mu\text{m}$ through altering experimental parameters (flow rate of toluene and gelatin solution and diameter of capillary) (Table 1) were produced using a microfluidic device shown in Figure 1(a). Secondly, the template moulds with multilayered hexagonally packed gelatin microspheres were formed (Figure 1(b)). Then 15% (w/v) PU solution in 1,4-dioxane (Sigma-Aldrich, US) was dropped into the moulds (Figure 1(c)). The compounded moulds were frozen at -20°C for 6 hours and then lyophilized overnight in a freeze-dryer to remove the solvent.

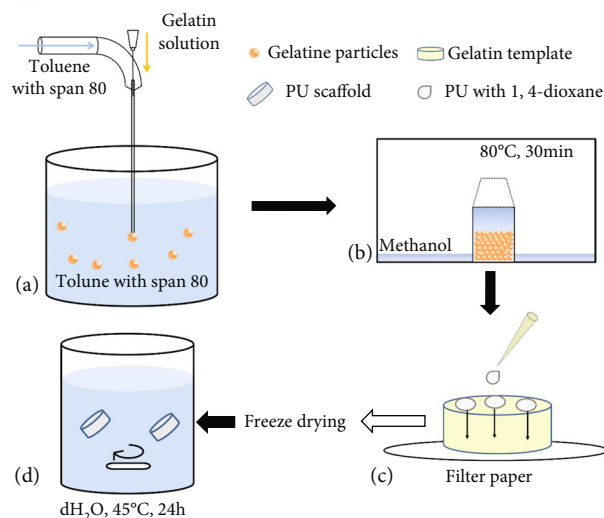


FIGURE 1: The schematic of 3D porous scaffold fabrication by inverse opal method. (a) Gelatin particle generation by the microfluidic device; (b) gelatin template formation in methanol atmosphere at a 80°C oven for 30 minutes; (c) PU solution penetration through gelatin template and filling the gaps between each gelatin particle; (d) PU scaffold collection after freeze drying for 6 hours and removal of gelatin particles by immersing in a water bath at 45°C for 24 hours.

Finally, the gelatin microspheres were removed through immersing the moulds in a water bath at 43°C with gentle stirring overnight (Figure 1(d)). PU-IOS scaffolds with 5 mm height and 5 mm diameter were obtained.

To generate SLS scaffolds, sodium chloride (NaCl) particles with the diameter between $250\ \mu\text{m}$ and $350\ \mu\text{m}$ were collected by sieves and then mixed with 15% PU solution or 6% (w/v) PLLA solution (in chloroform, Sigma, UK) for PU and PLLA scaffolds, respectively, with the weight ratio of polymer solution and NaCl at 1 : 9. The salt and polymer composites were kept in a cylinder-shaped mould for 3–5 days to evaporate the organic solvent, after which the composites were immersed in a water bath to leach out the salt particles thoroughly. The SLS scaffolds with diameter of 5 mm and height of 5 mm were collected.

2.2. Device Design for Gas Permeability Test. The convenient and simple device to assess gas permeability of porous scaffolds based on the bubble meter principle was designed [18, 19]. The device consisted of 4 parts as schematically drawn in Figure 2. The part 1 was used for gas transportation; it was composed a syringe pump (KD Scientific) and a 50 mL syringe (Norm Ject). The part 2 was utilized for sample holding. The porous scaffolds with defined dimension and a larger surface area than that of the vent of the 50 mL syringe were placed against the vent stably. The part 3 was the displaying component consisting of a flow direction changer via a three-way adaptor, a 2 mL syringe (Norm Ject) without plunger, and a floater which was made by the detergent film generated from a mixture viscous solution of detergent and distilled H_2O at the ratio of 4 : 1. A digital camera recorded the floater movement as the part 4. After the detergent film

TABLE 1: Experimental parameters to control different diameters of gelatin particles.

Diameter of gelatin particles (μm)	Flow rate of toluene solution (mL/h)	Flow rate of gelatin solution (mL/h)	Diameter of capillary (mm)
180 ± 18	24	4.8	0.5
250 ± 25	24	3.6	1
310 ± 45	24	6	0.5
430 ± 51	24	6	1

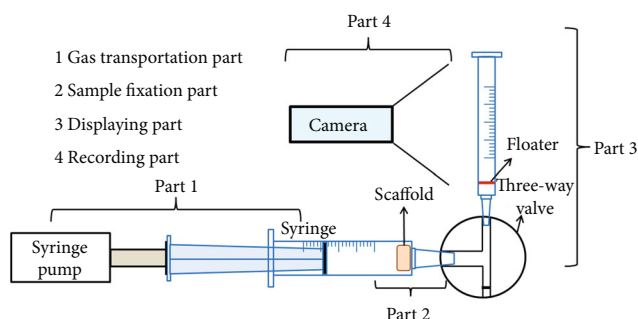


FIGURE 2: Schematic of designed gas permeability test device with four parts. 1: gas transportation part composed of a syringe pump and a syringe; 2: sample fixation part, enabling samples against the vent stably; 3: displaying part which uses a detergent film as the gas floater; 4: recording part composed of a digital camera.

was placed near the bottom of the 2 mL syringe, the syringe pump was set up to push the air inside the syringe through the scaffold by various flow rates. The movement rate of the floater was used as the readout of the different types of gas permeability of the scaffolds.

2.3. Characterization of Alveolus-Like Scaffolds

2.3.1. Observation of Scaffolds. The morphology of IOS and SLS scaffolds made by PU and PLLA, gelatin microspheres, and hexagonally packed gelatin moulds was observed by bright field microscope (Olympus, US) and SEM (FEI Teneo VS, US).

2.3.2. Gas Permeability. The gas permeability of PU-IOS scaffolds with various pore sizes and SLS scaffolds made from PLLA and PU was measured by the designed device. Firstly, the scaffolds ($\phi 5 \times 5$ mm) were placed inside the 50 mL syringe with stable attachment. The flow rate of the syringe pump was set up as 5, 10, 20, 30, and 40 mL/min, for each sample. For each flow setting and test, the movement distances of floater indicating as the initial height, H_0 , and the final height, H_1 , corresponding to initial time, T_0 , and final time, T_1 , respectively, were recorded by the camera. The movement rate of the floater (v) was calculated by the following formula:

$$v = \frac{H_1 - H_0}{T_1 - T_0}. \quad (1)$$

Each experiment was repeated at least three times. The gas permeability between the scaffold samples was compared by the floater movement rate.

2.3.3. Mechanical Property. The mechanical property of IOS and SLS scaffolds ($\phi 5 \times 5$ mm) was measured by mechanical testing machine (BOSE Electro Force 3200 Series, UK) at a speed of 10 mm/min under the compression mode. The stress and strain were plotted from original force-deformation curves according to the following formulas. Young's modulus was calculated accordingly.

$$\text{Stress} = \frac{\text{Force applied}}{\text{Area of specimen surface}},$$

$$\text{Strain} = \frac{\text{Original height} - \text{Final height}}{\text{Original height}}, \quad (2)$$

$$\text{Young's modulus} = \frac{\text{Stress}}{\text{Strain}}.$$

2.4. Fabrication of Tissue-Engineered Alveoli

2.4.1. Surface Modification. In order to enhance the cell attachment to PU-IOS, surface modification was conducted through introduction of vascular endothelial growth factor (VEGF) to scaffolds covalently [20]. Firstly, ammonia plasma treatment was applied to introduce the amine group to PU scaffolds. To do so, PU scaffolds were put into the plasma reaction chamber whose pressure was increased from 21 mbar to 50 mbar with ammonia gas pumping. The plasma treatment lasted for 5 minutes. Scaffolds were immersed into 70% ethanol for 2 hours for sterilization. Secondly, heparin was introduced onto the scaffold surface through crosslinking reaction with 1-ethyl-3-(3-dimethylaminopropyl) carbodiimide hydrochloride (EDC) and N-hydroxysulfosuccinimide (Sulfo-NHS). Ammonia plasma-treated PU scaffolds were immersed into the solution of EDC (2 mM), Sulfo-NHS (5 mM), and heparin (1 mg/mL) in 2-(morpholino)ethanesulfonic acid (MES) buffer and incubated for 2 hours at room temperature to bind heparin. After washing three times with PBS, the scaffolds were immersed into 100 μL of VEGF solution (100 ng/mL) for grafting at 4°C overnight. The grafted scaffolds were washed with PBS and kept at 4°C for further application.

2.4.2. MSCs Culture. MSCs isolated from rat bone marrow as described in our previous study [21] were used in this study. In brief, bone marrow in tibias and femurs from 4-week-old Sprague–Dawley rats was flushed with 10 mL of cell culture medium and transferred into two T25 culture flask (NUNC, US) and incubated by α -MEM medium (Hyclone, USA) supplemented with 10% fetal bovine serum (FBS, BI, Israel) and 1% antibiotics (Hyclone, USA) at 37°C with 5% CO_2 . The medium was replaced every 3 days until cells reached confluence. Cells were subcultured at a 1:2 plate ratio. Passage 3-5 MSCs were seeded onto the VEGF-modified alveolus-mimicking porous scaffolds with cell seeding density of $10^4/\text{mm}^3$. Neat PU-IOS scaffolds seeded with MSCs were used as the control group. The constructs were cultured

by the above-mentioned α -MEM medium at 37°C with 5% CO₂, and the medium was changed every two days.

2.4.3. Coculture. Human umbilical vein endothelial cells (HUVECs, Lonza) and human bronchial epithelial cell lines (NL20, ATCC) were cocultured to observe the localization of the two types of cells in the alveolus-like scaffolds. The media for NL20 contained Ham's F12 (Lonza, UK), with 4% FBS, 1.3% of 1.5 g/L NaHCO₃, 1% of 2 mM L-glutamine, 1% of 0.1 mM nonessential amino acids, 1% of antibiotic antimetabolic, and 0.05% of 0.5 μ g/mL hydrocortisone. The media for HUVECs was composed of Media 200 (M200, Thermo Fisher) with 2% low serum growth supplement (LGSS, Thermo Fisher). The NL20 and HUVECs with the ratio of 4:1 and cell density of 10⁵/mm³ were seeded onto scaffolds with a dimension of 50 mm³. NL20 were labelled with the PKH26 cell linker (Red, Sigma-Aldrich) following the product instruction before cell seeding, and HUVECs were identified by staining with CD31 after termination of the culturing. The cell-scaffold constructs were cultured in a mixed medium (with the ratio of 1:1), and the medium was changed every 2 days.

2.5. Characterization of Tissue-Engineered Alveoli

2.5.1. CCK-8 Assay. The viability and proliferation of MSCs on VEGF modified and nonmodified PU-IOS scaffolds were tested by cell counting kit-8 (CCK-8, Dojindo, Japan) as described in our previous study [20]. Briefly, at 1, 3, and 5 days after cell seeding, CCK-8 solutions at a dilution of 1:10 with media were added to each sample and cultured at 37°C with 5% CO₂. Two hours later, 100 μ L of media were transferred into a 96-well plate to measure the absorption value at a wavelength of 450 nm using a microplate reader (Synergy HT, BioTek, USA).

2.5.2. Confocal Observation of Cell Viability and Morphology. The viability of MSCs cultured on VEGF modified and nonmodified PU scaffolds at day 7 was determined by live and dead staining assay according to the product manual (Viability/Cytotoxicity Kit, Invitrogen, USA). Confocal microscopy (Leica, Germany) was used to observe the live and dead MSCs on PU scaffolds. Live cells were imaged as green color at an excitation of 488 nm and dead cells as red at an excitation of 535 nm. The three-dimensional (3D) images were reconstructed by *z*-stacking two-dimensional images with 10 μ m steps.

After 21 days of coculturing, the location and distribution of NL20 and HUVECs within the scaffolds were examined by expressed fluorescence; NL20 was displayed as red color by labelling with the PKH26 cell linker dye, whilst the HUVECs were stained with CD31 antibody. To stain the CD31 marker, the constructs were fixed by 4% paraformaldehyde (PFA) first at room temperature for 30 minutes. After removal of PFA, the constructs were washed with PBS twice, put into 1% BSA blocking solution, and incubated for one hour. After washing twice with PBS, the CD31 primary antibody (goat-antihuman, Santa Cruz, UK), diluted with 1% BSA with the ratio of 1:100, was added and incubated for at least 16 hours at 4°C. Constructs were washed with

PBS three times and incubated with secondary antibody (FITC-donkey antigoat, 1:100, Santa Cruz, UK) at 37°C for 3 hours. Finally, constructs were washed 3 times with PBS and counterstained by DAPI for the nucleus, then observed by confocal microscopy.

2.6. Statistical Analysis. All quantitative results were expressed as mean \pm standard deviation. At least 6 replicates were used for each group. Statistical analysis was carried out using one-way ANOVA and *t*-test for each two-group comparisons to determine significance. A value of *P* < 0.05 was considered to be statistically significant.

3. Results

Figure 3 shows the images of porogen particles and formed pores in the scaffolds. It can be seen that the microfluidic device generated uniform gelatin microspheres with diameter of 180 \pm 18, 250 \pm 25, and 310 \pm 45 μ m (Figures 3(a)–3(c)) compared with the sieving method (250–350 μ m, Figure 3(d)). Figures 3(e)–3(g) show the PU porous scaffolds with uniform pores, and Figure 3(h) shows the PLLA SLS scaffold with irregular pores.

Figure 4 shows the multilayered hexagonally packed gelatin microspheres (Figure 4(a) and PU-IOS scaffolds (Figures 4(b) and 4(c) used for MSC culturing. It can be seen that the gelatin microspheres we obtained had uniform diameters and the packed microspheres formed a hexagonal connection. Figure 4(C1) shows the cross-section of PU-IOS scaffolds with uniform pores and pore connection, and Figure 4(C2) shows the morphology of PU-IOS scaffolds with small pores inside big pores, indicating that the PU material did not cover the full surface of gelatin microspheres and tightly packed gelatin microspheres created the pore connections.

The reliability of the gas permeability testing device we designed was assessed by analyzing the relationship of the gas flow rate and the floater movement rate. We tested the device without scaffolds by setting the flow rate of the syringe pump at 5, 10, 20, 30, and 40 mL/min and found that the detergent film as a floater of device went up at a constant rate under the corresponding pump rate condition and was reproducible (data not shown). Figure 5 shows the results of gas permeability measurements of IOS and SLS scaffolds under different gas transportation rates. PU-IOS with pore size of 180, 310, and 430 μ m, PU-SLS, and PLLA-SLS with pore size of 250–350 μ m were used to validate the designed device. It can be seen from Figure 5 that there was no distinct difference between each groups when the gas transportation rate was 5, 10, and 20 mL/min. Whereas when the flow rate was increased to 30 mL/min, the gas permeability of PLLA-SLS was also obviously lower than the other groups, which indicated that PU had better gas permeability than PLLA. By closely monitoring the floater moving rate between 28 and 32 mL/min (Figure 5(b)), it was found that the PU-IOS had better gas permeability than PU-SLS. Furthermore, the gas permeability of PU-IOS increased gradually along with the increase of pore size. These results

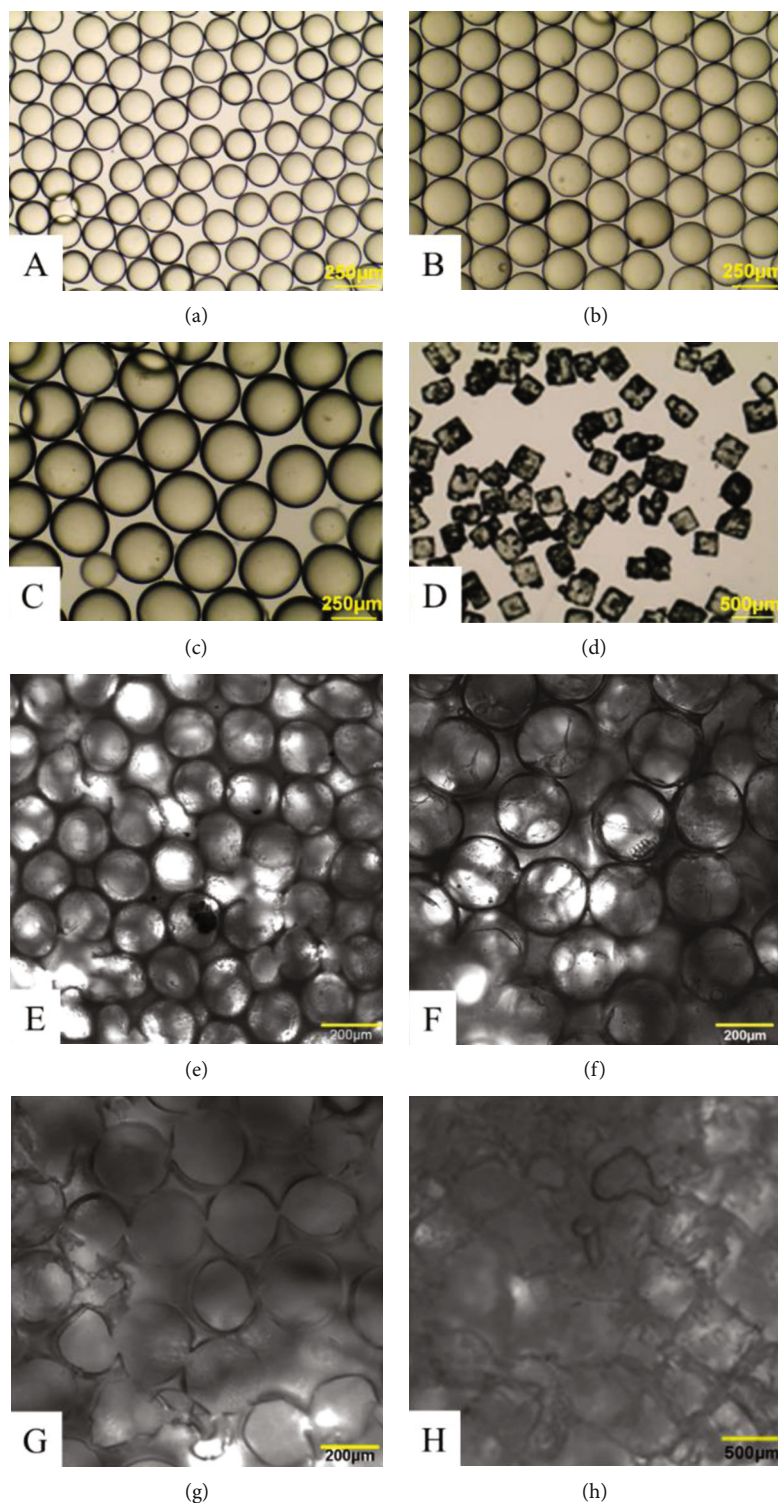


FIGURE 3: Visible images of porogens and the pores within scaffolds. Gelatin particles generated by the microfluidic device with different diameters (a–c), NaCl particles (d), and porous scaffolds (e–h). Gelatin particles with diameter of $180 \pm 18 \mu\text{m}$ (a), $250 \pm 25 \mu\text{m}$ (b), $310 \pm 45 \mu\text{m}$ (c), and NaCl particle with size of $250\text{--}350 \mu\text{m}$ (d). Scaffolds produced from inverse opal technique (e–g) and from salt leaching method (h).

indicated that the type of material, pore morphology, and size contributed significantly to gas permeability.

The mechanical properties of PU-IOS and PU-SLS and PLLA-SLS are shown in Figure 6. It was clear that PU-IOS

with a pore size of 310 and $430 \mu\text{m}$ had similar stiffness, while the stiffness of PU and PLLA porous scaffolds produced by the salt leaching method was much higher than that of inverse opal scaffolds. Compared with PLLA, PU salt

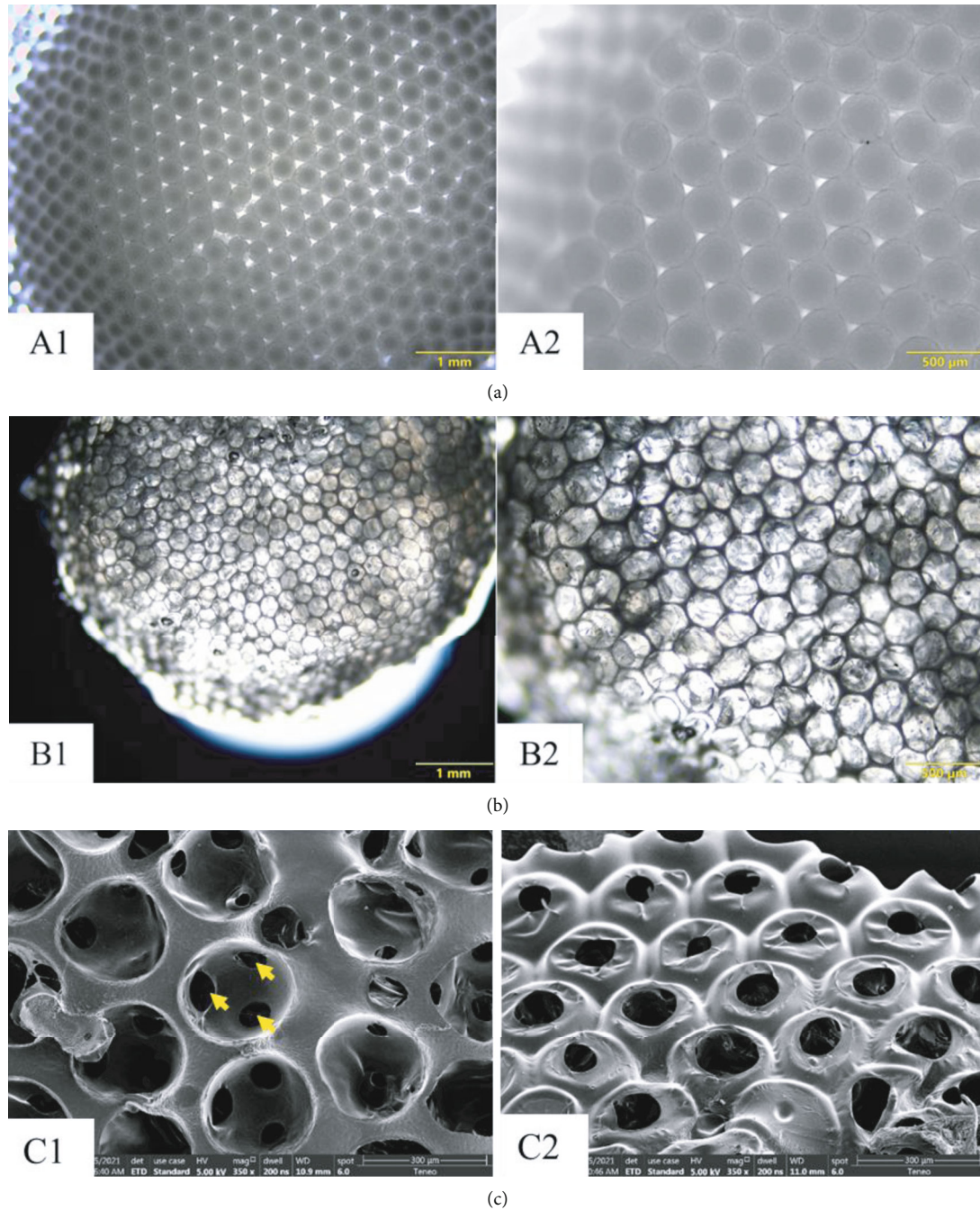


FIGURE 4: Images of gelatin microspheres packed moulds and formed scaffolds. Multilayered hexagonally packed gelatin microspheres (a) (A1, A2) and PU-IOs scaffolds (b) (B1, B2) from bright field microscopy. (c) (C1, C2) The formed PU scaffold observed by SEM. Arrows showed the smaller pores within big pores, which were created through connected gelatin microspheres.

leaching-formed scaffolds were softer. Figure 6(b) shows that PLLA-SLS scaffolds had the highest Young's modulus compared with PU scaffolds.

In Figures 7(a) and 7(b), the live and dead staining images show more live and less dead MSCs on VEGF-modified PU scaffolds Figure 7(b) than on neat PU scaffolds Figure 7(a) at day 7. Furthermore, it can be seen that MSCs spread well on VEGF-modified PU-IOs scaffolds instead of the round shape on PU neat scaffolds. Figure 7(c) shows the CCK-8 results of MSCs cultured on PU-IOs scaffolds

at days 1, 3, and 5. It is evident that MSCs on VEGF-modified PU-IOs scaffolds had better cell compatibility than those on unmodified PU scaffolds ($P < 0.05$). From the 3D images, we can see that MSCs grew along the wall of the pores and formed alveolus-like structures on VEGF-modified PU-IOs scaffolds (Figure 8(b)).

Figure 9 shows the NL20 attachment on day 3 and colocalization of NL20 and HUVECs on day 21 after being seeded. The red fluorescence in Figures 9(a) and 9(b) showed the NL20 cell tracking by PKH26 and the green

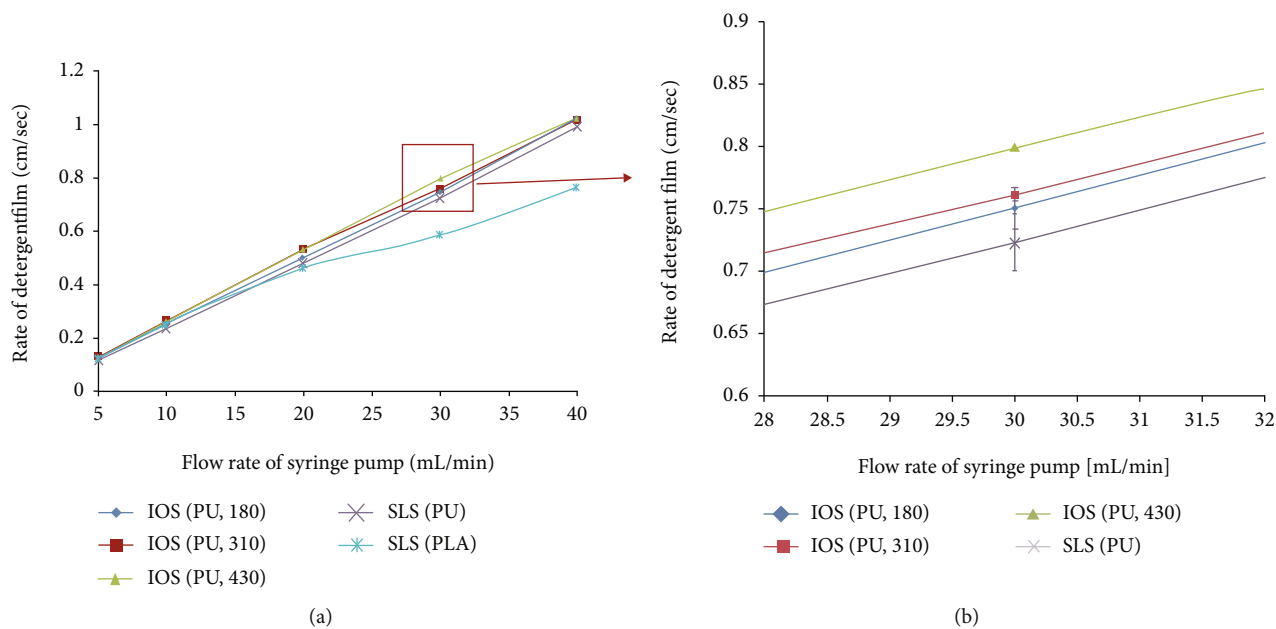


FIGURE 5: Gas permeability results of polyurethane scaffolds (IOS) made by inverse opal technique with different pore diameters and PLLA scaffolds (SLS) made from salt leaching method. (b) is the magnified image of the square part in (a).

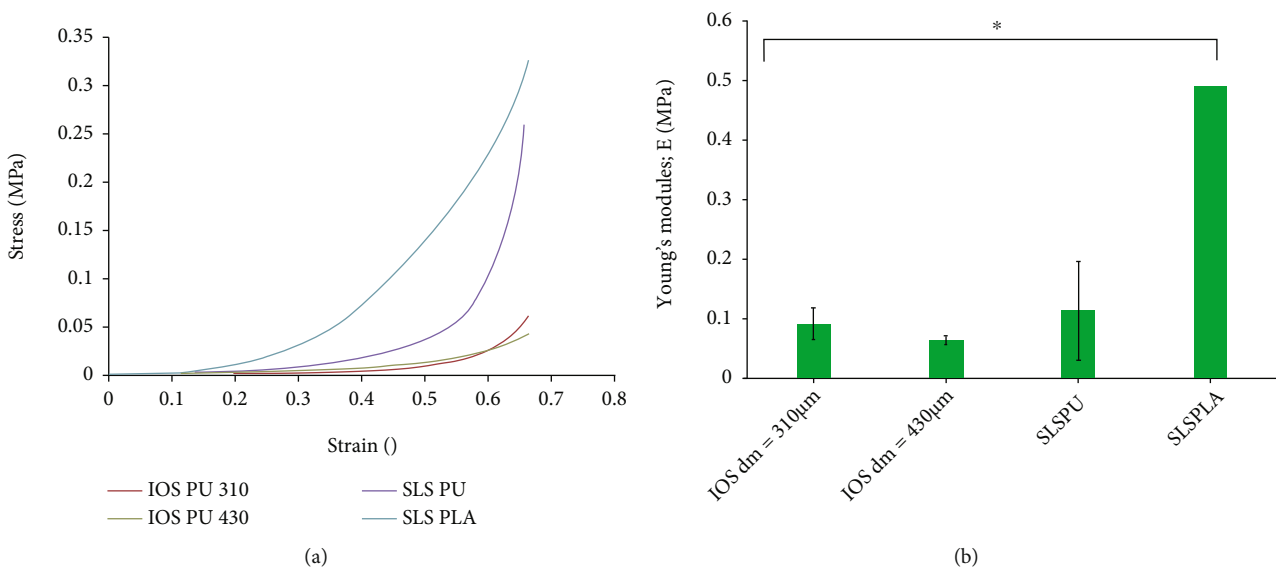


FIGURE 6: Mechanical property of polyurethane scaffolds made from inverse opal technique (IOS) and salt leaching method (SLS), and PLLA scaffolds made from salt leaching method (SLS). (a) Stress-Strain curves drawn according to compression data. (b) Young's modulus of scaffolds. $n = 3$; $*P < 0.05$.

color from the HUVEC stained by CD31 antibody (Figure 9(c)). In the merged image of Figure 9(d), we can see the yellow color which meant the colocalization of NL20 cells and HUVECs.

4. Discussions

Chronic lung diseases, such as COPD, CF, PH, and cancer, have no cure apart from lung transplantation. However, the critical shortage of donor lungs as well as the potential

immunorejection limits the usage of lung transplantation. Generation of functional lung tissue through tissue engineering approach already demonstrates high promise to meet the clinical demands. Replication of the complex three-dimensional architectural structure and function of alveolar units becomes a challenge for successful tissue engineering of the lung. In this study, we adapted the inverse opal fabrication technique to produce porous scaffolds using highly elastic polyurethane (PU-IOS) in comparison to scaffolds made from the salt leaching technique by stiff

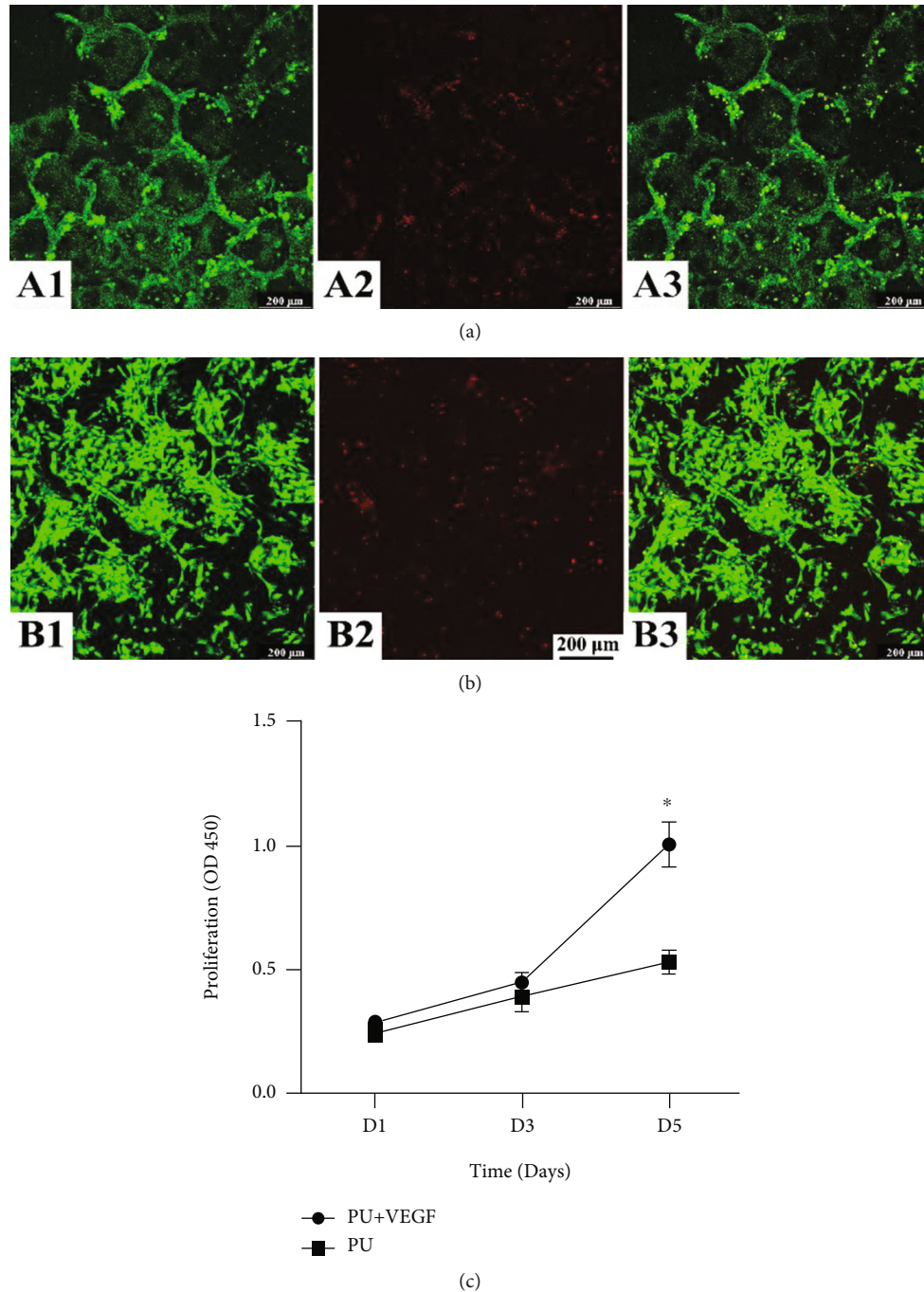


FIGURE 7: Confocal 2D images of the live and dead MSCs cultured in PU-IOS scaffolds for 7 days. (a) (A1–A3) Neat PU scaffolds; (b) (B1–B3) VEGF-modified PU-IOS scaffolds. Green color: live cells; red color: dead cells; (A3, B3) merged images. The quantitative cell viability cultured in the two types of scaffolds on days 1, 3, and 5 assessed by CCK-8 kit is presented in (c).

polylactic acid with focus on the gas permeability and cellular attachment capacity between the scaffolds. PU-IOS scaffolds with VEGF modification generated consistent superior outcomes than other types of scaffolds. The new gas permeability test device demonstrated reliable measurement outcomes of various scaffolds.

Gelfoam as a hemostatic surgical material has been widely used in clinics for decades. As the temporal scaffolds, Gelfoam will be completely degraded or absorbed in vitro

and in vivo quickly. Its porous structure and appropriate pore size similar to alveoli have been used in tissue engineering of the lung including us [11, 22–24]. Andrade et al. used Gelfoam sponge and fetal rat lung cells to regenerate an alveolus-like structure and explored the potential application for lung regeneration [11]. Gelfoam made from gelatin has low stability in an aqueous solution and enzyme environment. Compared with Gelfoam sponge, using the inverse opal fabrication technique can generate scaffolds with

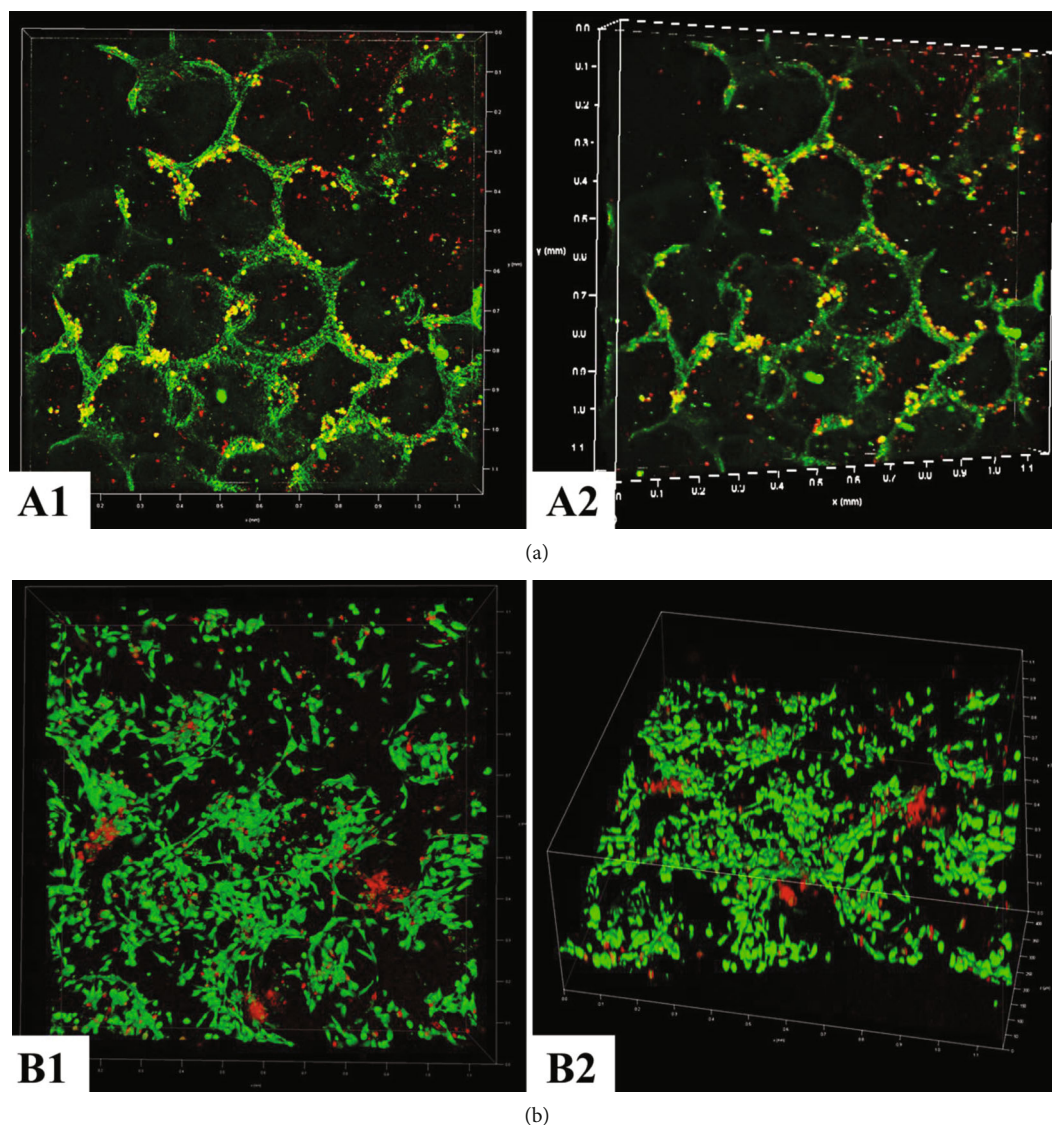


FIGURE 8: Confocal 3D images of the live and dead MSCs cultured in PU-IOS scaffolds for 7 days. (a) (A1, A2) Neat PU scaffolds; (b) (B1, B2) VEGF-modified PU IOS scaffolds; (A1, B1) top view; (A2, B2) side view. Green color: live cells; Red color: dead cells.

uniform and controllable pore size and regular pore connection, which mimics the alveolar cluster better and is therefore appropriate for lung tissue engineering.

Because of the elastic and permeability properties, PU and its family members have been used as an airway stent in bronchotracheal cancer and dynamic culture chamber in lung tissue engineering [25, 26]. To improve the biocompatibility, PU was modified by VEGF in this study, which can enhance the attachment and proliferation of MSCs. The results of CCK-8 at days 1, 3, and 5 and live and dead staining at day 7 showed that the modification of VEGF was very effective, which was also verified in our previous study [20]. Interestingly, when coculturing endothelial cells, HUVEC, with epithelial cells, NL20, colocalization of the two types of cells was clearly visible (Figure 9), which indicated that the inverse opal-fabricated scaffolds supported multiple cell populations on the alveolus-like structure.

We successfully grew MSC in PU-IOS scaffolds aiming to explore new cell sources for lung regeneration. It is clinically difficult to obtain autologous lung cells (endothelial, epithelial, fibroblasts) to treat patients with the aforementioned lung diseases. Induction and differentiation of MSC or lung progenitor cells [27] represent a promising and realistic direction to generate alveolar tissues by the lung tissue engineering approach. Figures 7 and 8 show that MSCs proliferated along with the wall of pores; it can still be found that MSCs cannot form a whole pore structure like alveoli, which was probably due to the short culture time enabling to form the cell sheet and also the static culture method. This is a limitation of our study. A longer culture time and dynamic culture method should be used to form an alveolar structure in future studies.

Gas permeability is one essential feature of lung tissue. However, there were few studies to test the gas permeability

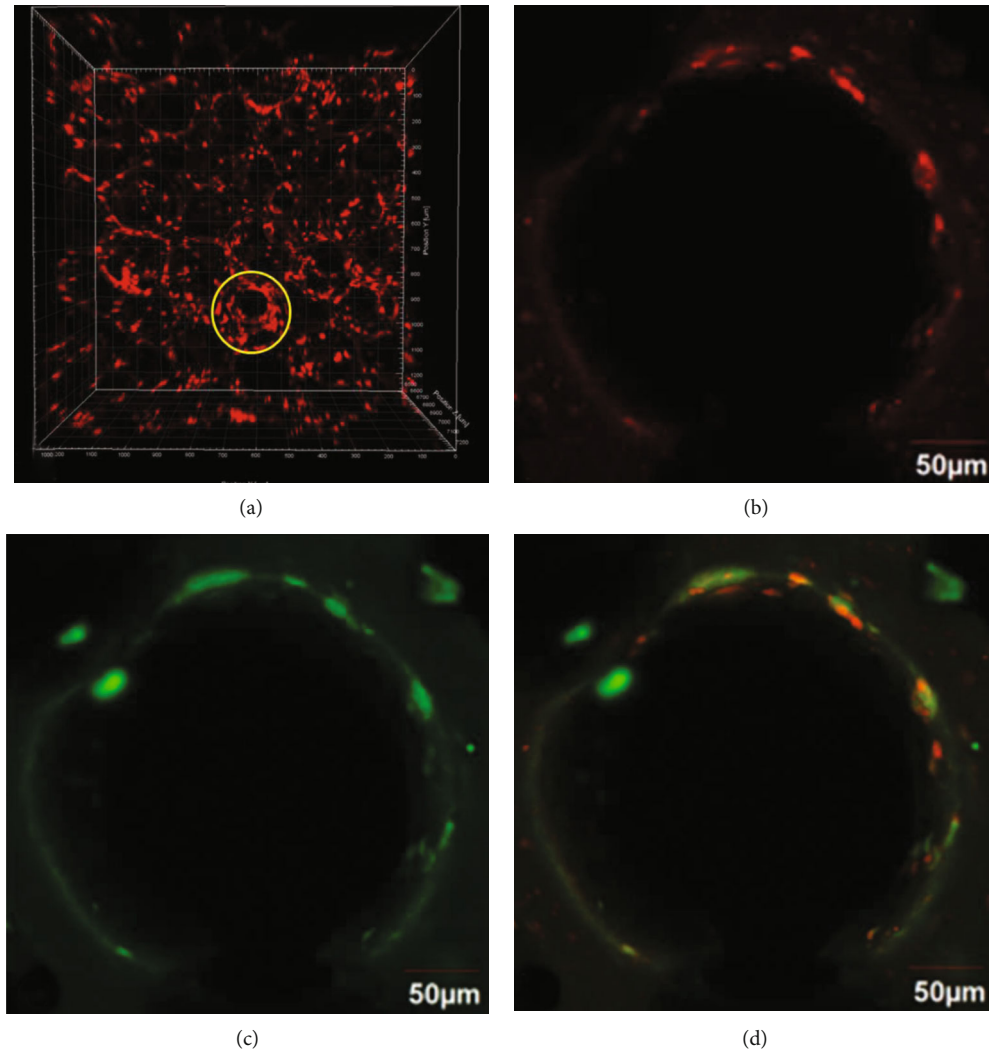


FIGURE 9: Confocal images of coculturing NL20 cells and HUVECs on VEGF modified PU-IOS scaffolds. NL20 cells were imaged live with labelling by PKH26 cell tracker (red color) on day 3 and day 21, whilst HUVECs were identified by CD31 staining (green color) on day 21. (a) Confocal live z-stacking 3D images of the construct cultured for 3 days. Yellow circle showed the cells attached onto the pore surface. (b) Confocal live 2D image of the construct cultured for 21 days; (c) confocal 2D image of the construct cultured for 21 days with CD31 staining showing the location of HUVECs cells; (d) merged images.

of 3D lung porous scaffolds [26], although the mature methods for permeability testing in the food packaging field have already been established [17]. In this study, we designed a facile device to evaluate gas permeability of porous scaffolds for lung tissue engineering with a syringe pump as the gas transportation component and detergent film. According to Levy's research, the bubble meter method showed an accuracy of 99.75% in the measurement [18]. We conducted three sets of experiments to confirm the feasibility and accuracy of our device. The testing results without scaffolds showed the linear relation of the gas flow rate and the movement rate of the detergent film. Then, the scaffolds' pore morphology and materials on gas permeability were analyzed.

We fabricated PLLA salt leaching porous scaffolds, PU salt leaching porous scaffolds, and PU inverse opal scaffolds with different pore sizes for gas permeability tests. It has been reported that various techniques including solvent

casting/particulate leaching, gas foaming, and phase separation technology could produce porous scaffolds (with porosities of ~35-60%) but with limited interconnectivity between pores [28]. Zhang et al. demonstrated that inverse opal scaffolds (porosity of ~74%) with higher interconnectivity (window size of 60-70 μm) had a higher diffusion rate of macromolecules (FITC-dextran, $M_w \approx 20\text{k}$), in comparison to scaffolds with nonuniform pores and a window size of 30 μm [29]. Our results of gas permeability were consistent with these reports. With a higher pore connection rate, PU inverse opal scaffolds had higher permeability than PU salt leaching scaffolds, which indicated the reliability of our device for gas permeability testing.

Next, we compared the materials' effect on gas permeability. We found that the PU salt leaching scaffolds had better gas permeability than PLLA scaffolds produced by the same technique, which demonstrated that PU has a better gas permeability property and is much more suitable for

lung tissue engineering in comparison to PLLA. Bao et al. reported that the O₂ and CO₂ permeation of PLLA used for packaging was 0.14 Barrers (at 22.8°C) and 1.1 Barrers (at 30°C), respectively [30], while the O₂ and CO₂ permeation of PU reported by Turan and colleagues was 5.17 Barrers and 78.69 Barrers at 25°C, respectively [31]. Overall, considering our gas permeability results and previous studies, we conclude that the gas permeability of scaffolds was determined not only by the fabrication methods but also by the characteristics of the materials used. Our new gas permeability device accurately detected the individual and combinational factors for the gas permeability.

The applied flow rate of gas can also affect the detection results. We set up the flow rate as 5, 10, 20, 30, 40, and 50 mL/min to observe the floater's movement and noticed that it was hard to distinguish the permeability property of scaffolds when the rate was lower than 20 mL/min. The lower gas flow rate might not generate sufficient pressure. Because of the delicate detergent bubble, the flow rate cannot set higher than 50 mL/min as this would have led to the breaking of the detergent film. Therefore, the gas flow rate set at 30 or 40 mL/min was suitable for testing permeability of the porous scaffolds. This is a limitation of the new device. A more durable and sensitive floater needs to be discovered.

5. Conclusions

In the current work, we presented a useful strategy for fabrication of scaffolds for lung tissue engineering and designed a gas permeability tester to assist the fabrication. The polyurethane scaffolds produced by the inverse opal technique resulted in highly connective pores and elastic property and demonstrated high cellular attachment and colocalization of epithelial and endothelial cells on them into alveolus-like tissues. VEGF-modified scaffolds enhanced the outcomes. The designed gas permeability tester with the detergent film floater can distinguish the gas permeability in scaffolds with different pore morphologies and made from different materials.

Data Availability

All study data are included in the article.

Conflicts of Interest

The authors declare no competing financial interests.

Acknowledgments

This work was supported by the EC FP7 Marie Curie International Incoming Fellowship; the Natural Science Foundation of China (grant number 31800810); the Natural Science Foundation of Jiangsu Province, China (grant number BK20180998); the Postdoctoral Science Foundation of China (grant number 2019M651973); and the Jiangsu Planned Projects for Postdoctoral Research Funds (grant number 2018K055B).

References

- [1] G. D'Amato, C. E. Baena-Cagnani, L. Cecchi et al., "Climate change, air pollution and extreme events leading to increasing prevalence of allergic respiratory diseases," *Multidisciplinary Respiratory Medicine*, vol. 8, no. 1, p. 12, 2013.
- [2] X. Liu, Q. Fang, and H. Kim, "Preclinical studies of mesenchymal stem cell (MSC) administration in chronic obstructive pulmonary disease (COPD): a systematic review and meta-analysis," *PLoS One*, vol. 11, article e0157099, 2016.
- [3] H. Zhu, Y. Xiong, Y. Xia et al., "Therapeutic effects of human umbilical cord-derived mesenchymal stem cells in acute lung injury mice," *Scientific Reports*, vol. 7, no. 1, p. 39889, 2017.
- [4] M. M. Hoepfer, M. Humbert, R. Souza et al., "A global view of pulmonary hypertension," *The Lancet Respiratory Medicine*, vol. 4, no. 4, pp. 306–322, 2016.
- [5] J. C. Davies, "Cystic fibrosis in 2016: considerable progress, but much more to do," *The Lancet Respiratory Medicine*, vol. 4, no. 12, pp. 943–945, 2016.
- [6] F. R. Hirsch, G. V. Scagliotti, J. L. Mulshine et al., "Lung cancer: current therapies and new targeted treatments," *Lancet*, vol. 389, pp. 299–311, 2017.
- [7] D. Van Raemdonck, R. Vos, J. Yserbyt, H. Decaluwe, P. De Leyn, and G. M. Verleden, "Lung cancer: a rare indication for, but frequent complication after lung transplantation," *Journal of Thoracic Disease*, vol. 8, no. S11, pp. S915–S924, 2016.
- [8] T. H. Petersen, E. A. Calle, L. Zhao et al., "Tissue-engineered lungs for in vivo implantation," *Science*, vol. 329, pp. 538–541, 2010.
- [9] A. Doryab, G. Amoabediny, and A. Salehi-Najafabadi, "Advances in pulmonary therapy and drug development: lung tissue engineering to lung-on-a-chip," *Biotechnology Advances*, vol. 34, pp. 588–596, 2016.
- [10] E. V. Kuevda, E. A. Gubareva, I. S. Gumenyuk et al., "Modification of rat lung decellularization protocol based on dynamic conductometry of working solution," *Bulletin of Experimental Biology and Medicine*, vol. 162, no. 5, pp. 703–706, 2017.
- [11] C. F. Andrade, A. P. Wong, T. K. Waddell, S. Keshavjee, and M. Liu, "Cell-based tissue engineering for lung regeneration," *American Journal of Physiology. Lung Cellular and Molecular Physiology*, vol. 292, pp. L510–L518, 2007.
- [12] W. J. Zhang, Q. X. Lin, Y. Zhang et al., "The reconstruction of lung alveolus-like structure in collagen-matrigel/microcapsules scaffolds in vitro," *Journal of Cellular and Molecular Medicine*, vol. 15, pp. 1878–1886, 2011.
- [13] S. W. Choi, Y. Zhang, M. R. Macewan, and Y. Xia, "Neovascularization in biodegradable inverse opal scaffolds with uniform and precisely controlled pore sizes," *Advanced Healthcare Materials*, vol. 2, pp. 145–154, 2013.
- [14] B. F. GMBH, "GDP-C - Gas Permeability Tester," 2021, <https://www.brugger-feinmechanik.com/en/products/permeation-testers/gdp-c-gas-permeability-tester/>.
- [15] F. P. I. Company, "Frazier precision instrument company, Inc., makers of precision testing instrumentation," 2021, <http://www.frazierinstrument.com/>.
- [16] F. Boschetti, F. Gervaso, G. Pennati, G. M. Peretti, P. Vena, and G. Dubini, "Poroeleastic numerical modelling of natural and engineered cartilage based on in vitro tests," *Biorheology*, vol. 43, no. 3,4, pp. 235–247, 2006.
- [17] V. Siracusa, "Food packaging permeability behaviour: a report," *International Journal of Polymer Science*, vol. 2012, Article ID 302029, 11 pages, 2012.

- [18] A. Levy, "The accuracy of the bubble meter method for gas flow measurements," *Journal of Scientific Instruments*, vol. 41, pp. 449–453, 1964.
- [19] L. Lyu, D. Kasai, Y. Yang, and T. Xu, *A device and method for detecting permeability of tissue engineering porous scaffolds*, S.I.P. Office, China, 2018.
- [20] L. Lu, A. Deegan, F. Musa, T. Xu, and Y. Yang, "The effects of biomimetically conjugated VEGF on osteogenesis and angiogenesis of MSCs (human and rat) and HUVECs co-culture models," *Colloids and Surfaces. B, Biointerfaces*, vol. 167, pp. 550–559, 2018.
- [21] L. X. Lu, X. F. Zhang, Y. Y. Wang et al., "Effects of hydroxyapatite-containing composite nanofibers on osteogenesis of mesenchymal stem cells in vitro and bone regeneration in vivo," *ACS Applied Materials & Interfaces*, vol. 5, pp. 319–330, 2013.
- [22] A. Kyoseva, Y. Yang, and N. Forsyth, "An alveolar structural mimic: a tissue engineering solution for emphysema," in *UK Society for Biomaterials, 16th annual conference*. 52, June 2017.
- [23] J. Y. Kasper, M. I. Hermanns, R. E. Unger, and C. J. Kirkpatrick, "A responsive human triple-culture model of the air-blood barrier: incorporation of different macrophage phenotypes," *Journal of Tissue Engineering and Regenerative Medicine*, vol. 11, pp. 1285–1297, 2017.
- [24] N. K. Paschos, W. E. Brown, R. Eswaramoorthy, J. C. Hu, and K. A. Athanasiou, "Advances in tissue engineering through stem cell-based co-culture," *Journal of Tissue Engineering and Regenerative Medicine*, vol. 9, pp. 488–503, 2015.
- [25] W. Chen, J. Clauser, A. L. Thiebes et al., "Selection and fabrication of a non-woven polycarbonate urethane cover for a tissue engineered airway stent," *International Journal of Pharmaceutics*, vol. 514, pp. 255–262, 2016.
- [26] A. A. Tomei, F. Boschetti, F. Gervaso, and M. A. Swartz, "3D collagen cultures under well-defined dynamic strain: a novel strain device with a porous elastomeric support," *Biotechnology and Bioengineering*, vol. 103, pp. 217–225, 2009.
- [27] W. Zuo, T. Zhang, D. Z. Wu et al., "p63⁺Krt5⁺ distal airway stem cells are essential for lung regeneration," *Nature*, vol. 517, no. 7536, pp. 616–620, 2015.
- [28] R. Farajzadeh, S. Vincent-Bonnieu, and N. Bourada Bourada, "Effect of gas permeability and solubility on foam," *Journal of Soft Matter*, vol. 2014, Article ID 145352, 7 pages, 2014.
- [29] Y. S. Zhang, S.-W. Choi, and Y. Xia, "Inverse opal scaffolds for applications in regenerative medicine," *Soft Matter*, vol. 9, no. 41, pp. 9747–9754, 2013.
- [30] L. Bao, J. R. Dorgan, D. Knauss, S. Hait, N. S. Oliveira, and I. M. Maruccho, "Gas permeation properties of poly(lactic acid) revisited," *Journal of Membrane Science*, vol. 285, pp. 166–172, 2006.
- [31] D. Turan, S. Sangerlaub, C. Stramm, and G. Gunes, "Gas permeabilities of polyurethane films for fresh produce packaging: response of O₂ permeability to temperature and relative humidity," *Polymer Testing*, vol. 59, pp. 237–244, 2017.

Review Article

Spidroin-Based Biomaterials in Tissue Engineering: General Approaches and Potential Stem Cell Therapies

Qi Zhang ¹, Min Li ¹, Wenbo Hu,² Xin Wang,² and Jinlian Hu ¹

¹Department of Biomedical Engineering, City University of Hong Kong, Kowloon, Hong Kong

²Biological Science Research Center, Southwest University, Chongqing 400716, China

Correspondence should be addressed to Jinlian Hu; jinliahu@cityu.edu.hk

Received 30 June 2021; Revised 25 September 2021; Accepted 10 November 2021; Published 20 December 2021

Academic Editor: Ying Yang

Copyright © 2021 Qi Zhang et al. This is an open access article distributed under the Creative Commons Attribution License, which permits unrestricted use, distribution, and reproduction in any medium, provided the original work is properly cited.

Spider silks are increasingly gaining interest for potential use as biomaterials in tissue engineering and biomedical applications. Owing to their facile and versatile processability in native and regenerated forms, they can be easily tuned via chemical synthesis or recombinant technologies to address specific issues required for applications. In the past few decades, native spider silk and recombinant silk materials have been explored for a wide range of applications due to their superior strength, toughness, and elasticity as well as biocompatibility, biodegradation, and nonimmunogenicity. Herein, we present an overview of the recent advances in spider silk protein that fabricate biomaterials for tissue engineering and regenerative medicine. Beginning with a brief description of biological and mechanical properties of spidroin-based materials and the cellular regulatory mechanism, this review summarizes various types of spidroin-based biomaterials from genetically engineered spider silks and their prospects for specific biomedical applications (e.g., lung tissue engineering, vascularization, bone and cartilage regeneration, and peripheral nerve repair), and finally, we prospected the development direction and manufacturing technology of building more refined and customized spidroin-based protein scaffolds.

1. Introduction

Spider silk has attracted much attention for thousands of years due to its resilience, toughness, and biocompatibility. Since ancient Greeks, natural spider silks have been well documented in medical applications as bandages owing to their outstanding hemostatic performance [1, 2]. The antibacterial phenomena and hypoallergenic properties have also been found from natural spider silks [3], which indicate spider silk material's great potential in biomaterial and tissue engineering areas. In nature, spiders produce various types of silk fibers from separate glands for multiple purposes of creating shields for protection from predators, encasing their eggs, and weaving webs. As shown in Figure 1, up to seven types of silk-producing glands extrude proteins through spinnerets to produce spider silks, e.g., dragline/major ampullate silk, minor ampullate silk, flagelliform silk, tubuliform silk, aciniform silk, aggregate silk, and piriform silk.

Each type of silk fiber presents unique mechanical properties, internal structure, and composition, all determined by their functions [4, 5]. Among these kinds of spider silks, the major ampullate silk (also called dragline silk) has been extensively investigated due to its excellent comprehensive mechanical properties [6, 7]. Compared with natural fibers and synthetic materials, spider silks exhibit a well-balanced combination of stiffness and elasticity, which perfectly satisfies scaffold biomaterial's mechanical and biological requirements for tissue engineering. However, the natural sources of spider silks and processing methods are limited. Therefore, technological strategies in genetic engineering have long been used to integrate specific genes and recombinantly engineered natural spider silk proteins.

Spider silk is a protein biopolymer that varies in physicochemical and biological properties due to a variation in structure and composition. Based on this processability, researchers manage to use natural or recombinant spider silk

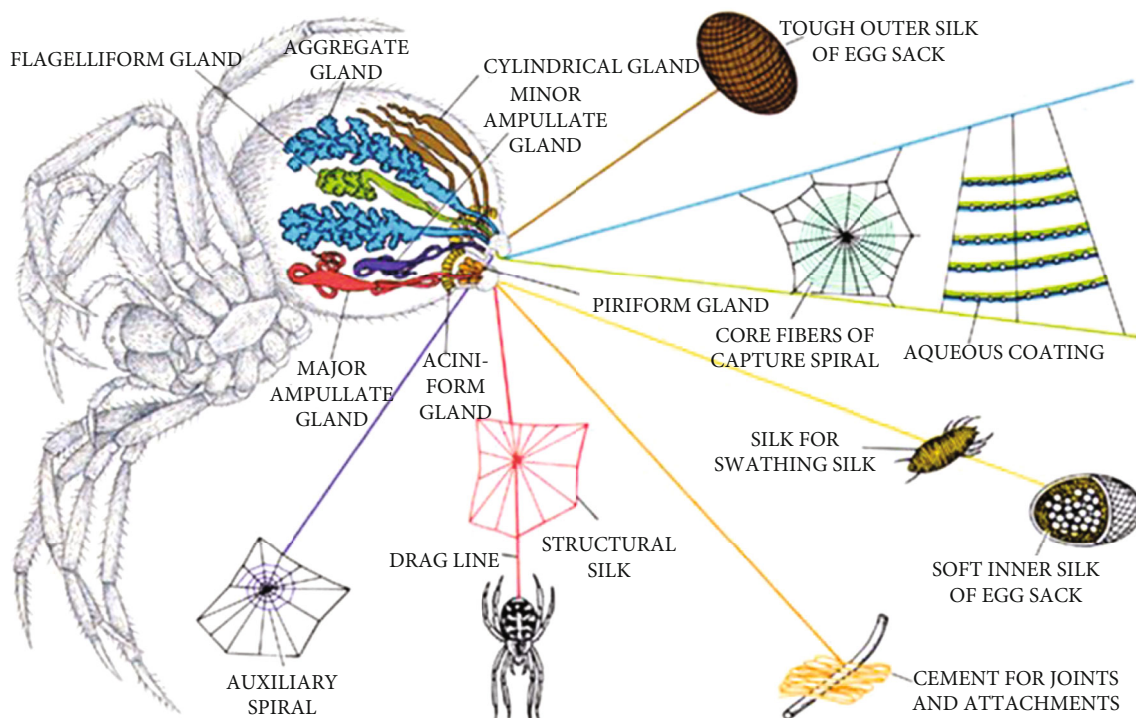


FIGURE 1: Seven types of spider silk glands and spider silks from spider *Araneus diadematus*: dragline/major ampullate silk (red), minor ampullate silk (purple), flagelliform silk (green), tubuliform silk (brown), aciniform silk (yellow), aggregate silk (blue), and piriform silk (orange). Reproduced from F. Vollrath, 2000, Copyright © 2000, Elsevier Science B.V. All rights reserved.

proteins as raw material to manufacture tailor-made scaffolds with controllable structures and outstanding properties for diverse tissues or applications.

As an essential part of tissue engineering, scaffolds are usually used for functional reconstruction of damaged organs and defective tissues, including promoting cell adhesion and proliferation, extracellular matrix regeneration, and recovery of vessels and nerves around newly generated tissues, which requires that scaffold materials should be processible to be manufactured into different forms and structures to provide sufficient space for substance and information interexchange between tissue and cells. In addition, scaffolds should also have good biocompatibility to reduce inflammation and cytotoxicity. As the center of tissue regeneration and carrier of stem cells and cell signals, the corresponding mechanical strength of scaffold materials should be also guaranteed to maintain the complex structure of the scaffold during tissue regeneration [8, 9]. For many biomedical applications, spidroin has been modified to form specific structures, including thin films, fibers, hydrogels, microspheres, and sponges. And the further understanding of the internal characteristics of spider silk protein structure-function will also help to design new polymer materials inspired by nature.

In this review, we will discuss spidroin-based scaffolds with different dimensions and their applications in tissue engineering and regenerative medicine as shown in Figure 2, to demonstrate the great potential of spidroin-based material in the biomedical engineering field. Because of the complexity of lung tissue regeneration, there is a lack

of research on the application of spidroin-based materials to lung tissue repair. What is exciting is that we still see the great possibility of using spidroin-based biomaterials for lung tissue engineering from many researches on spidroin-based scaffolds, and they are also summarized in this review. Meanwhile, we also make an outlook about the development of the next-generation multifunctional spidroin-based scaffold through the manufacturing process, genetic engineering, and molecular biology.

2. Spider Silk as a Matrix for Tissue Engineering

2.1. Extracellular Matrix (ECM) and Requirement for Scaffold Design. The extracellular matrix (ECM) is the tissue-specific three-dimensional network architecture on or between cells. It is mainly composed of cell secretory products in each tissue and organ, including collagen, fibronectin, laminin, glycosaminoglycan, and growth factor. Each component has its own role and function. As the most abundant protein in ECM, collagen provides the connection between ECM and actin cytoskeleton to promote the exchange of nutrients and information. In general, ECM not only offers the necessary structural strength required for common tissue activities but also adjusts the cell living, apoptosis, proliferation, differentiation, shaping, and migration through growth factors and cytokines [10–13].

For scaffold design in tissue engineering, many factors should be carefully considered to mimic the ECM function and create a favorable living environment for tissue and

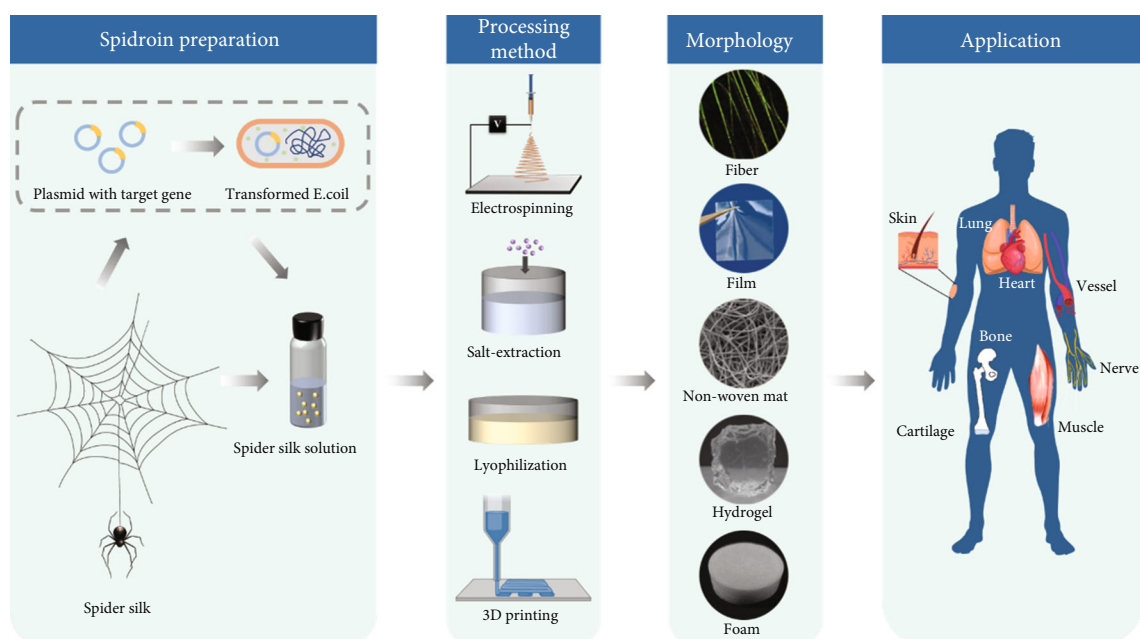


FIGURE 2: Schematic diagram of scaffold preparation using recombinant spidroins manufactured by transformed *E. coli* and their applications in the tissue engineering area. Reproduced from S. Salehi et al., 2020, under the Creative Commons Attribution License.

organ regeneration [11]. Firstly, biocompatibility and biosafety are particularly important to scaffold material. There should be no cytotoxicity and immunoreaction when scaffolds are implanted into the human body [14, 15]. Secondly, the appropriate mechanical properties of scaffolds also need to be emphasized. During treatment, most scaffolds need to temporarily bear tension or pressure to remodel and induce the differentiation of stem cells, so their mechanical properties are preferred to be similar with surrounding tissues [16]. Thirdly, the processability of biomaterial is also necessary, which allows biomaterials to be precisely designed and processed into various effective structures. In order to simulate the ECM function mentioned above, porous or fibrous architecture is more suitable for intercellular communication and nutrient transport. On the one hand, this scaffold architecture has relatively high specific surface area, which offers more connecting sites for fibronectin proteins to adhere to stem cells. On the other hand, a porous structure scaffold with appropriate porosity provides space for neovascularization and the nervous system and reconstructs metabolic and information channels between new tissues and their surrounding [11, 17, 18]. Finally, the degradation rate of the scaffold should match the rate of secretion and generation of new ECM and tissue, and this processing rate can be adjusted through modifying scaffold composition, structure, etc. Meanwhile, the degradation products must also be non-cytotoxic to ensure that there will be no secondary damage due to degradation in the process of tissue regeneration. With the development on the research about tissue engineering and interaction between biomaterials and tissues, higher and higher requirements are put forward for scaffold design, which is both a challenge and an opportunity to provide better scaffolds for tissue engineering [19, 20].

2.2. Interactions between Spider Fibroin and Cells. Over the past years, researchers have generated extensive evidence that biochemical cell-matrix interactions can improve cell survival and function. Many approaches, including chemical modification of the primary structure of spidroin, gene modification with cell-binding motifs, and the change of the material surface topographies, have been adapted to improve cell behaviors (e.g., cell attachment, proliferation, and differentiation) to scaffolds made of spider silk proteins [21–24].

Chemical coupling techniques rely on certain chemicals that are not always biocompatible with cells, and the efficiency of this nonspecific adhesion on *in vitro* culture is relatively low for some types of cells [25]. To further improve the interactions between cells and biomaterials, the cell-binding peptide motif, such as RGD (Arg-Gly-Asp), has been extensively incorporated in materials. Widhe et al. demonstrated the viability of fibroblast-cultured RGD films using a two-color fluorescence viability assay. Adhered cells were found on all matrices after 24 h, with almost no dead cells. Additionally, at an early time point of 3 h, the cells on the RGD membrane showed many distinct focal adhesion points and well-organized actin stress fibers, which were similar to those on fibronectin, indicating an excellent cell attachment activity [26]. However, the cell types and their sensitivity to growth conditions should certainly be considered with respect to the evaluation of RGD-based materials for adhesion [27].

To explore the interaction between cells and morphology/topology of various forms of spider silk-based materials, Aldo et al. characterized the films, hydrogels, and electrospun nonwoven meshes made of the recombinant spider silk protein eADF4(C16) on the adhesion and proliferation of fibroblasts. The films and hydrogels had high hydration

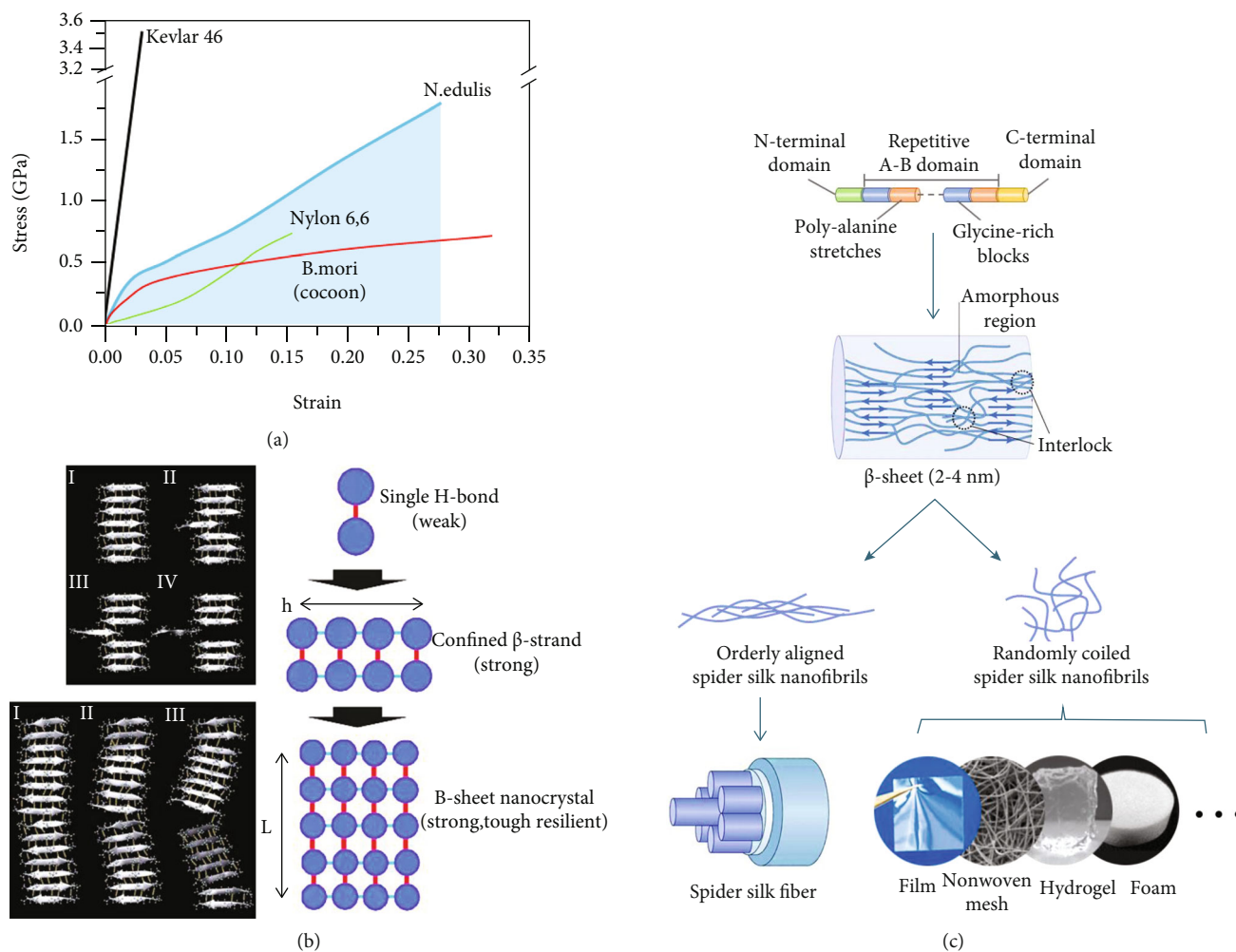


FIGURE 3: (a) The strain-stress curve of different fiber materials including Kevlar 46, dragline fiber of *N. edulis*, Nylon 6,6, and cocoon silk fiber from *B. mori*; the toughness of *N. edulis* dragline fiber is illustrated by a colored area. Reproduced from C. Fu et al., 2009, Copyright © 2009, Royal Society of Chemistry. (b) Hierarchical organization of spider silk nanocrystals and deformation profiles of β -sheet crystals at different sizes. Reproduced from S. Keten et al., 2009, Copyright © 2021, Nature Publishing Group. (c) Hierarchical structure of spider silk fiber and nonfiber spidroin materials. Based on the nanofibril network topology and internanofibril interaction strength, silk fibers and nonfiber silk materials are of different fibril arrangements: among silk fibers, silk nanofibrils are bundled along the fibrous axis, while for nonfiber silk materials, silk nanofibrils are interconnected in a nearly random manner. Reproduced from S. Ling et al., 2018, Copyright © 2021, Macmillan Publishers Limited and W. Qiu et al., 2019, Copyright © 2021, Wiley-VCH Verlag GmbH & Co. KGaA, Weinheim.

and a low contact angle. They produced a thin layer of water on their surface, which inhibits proteins' adhesion, reducing cell attachment. In comparison, the nonwoven meshes displayed a defined surface topology of high surface area, which is conducive to the filopodia protrusion and the posterior spreading around the fibers. This phenomenon usually occurs in the absence of specific binding sequences/ligands to enhance cell adhesion. With the increase in fiber diameter, the distance between fibers also increases, making the filopodia protrude more efficiently [28].

2.3. Mechanical Properties of Spider Silk: From Sequence to Structure. Natural spider silk, especially the major ampullate silk, has impressive comprehensive mechanical properties, including high tensile strength (0.9~1.4 GPa) and excellent extensibility (25%~40%), which endow spider silks with

excellent toughness (colored area under the curve in Figure 3(a), $160\sim 250 \text{ MJ cm}^{-3}$) which is even higher than that of steel and Kevlar fibers [7, 29, 30]. In addition to the excellent comprehensive mechanical properties, the fine hierarchical structure of spider silk has also been widely researched. The well-known dragline silk is mainly composed of two fibrous proteins MaSp1 and MaSp2, which are secreted from the major ampullate silk gland. According to the amino acid sequence, the dragline spidroin molecular chain is composed of three blocks, including two nonrepetitive domains N-/C-terminals and repetitive regions made of poly-alanine stretches (A_n , $n = 4\text{--}10$ for MaSp1 and $n = 3\text{--}9$ for MaSp2) and glycine-rich blocks (GGX ($X = A, Q, \text{ or } Y$) and GX ($X = Q, A, \text{ or } R$) for MaSp1 and GPX ($X = G \text{ or } S$), QQ, GGX (X is usually A), and GSG for MaSp2) [31–33]. During the natural spinning process, N-/C-terminals perform

a response to pH gradient, dehydration, ion exchange, and shear stress, thereby inducing the assembly of aligned protein molecular chains and the elongation of silk fibers [34].

On the molecular scale, poly-alanine (A_n) stretching compounds are pressed together and tightly connected through H-bonds to form the hard β -sheet nanocrystals with high modulus. Poly-alanine stretching compounds commonly include 4-12 Ala with 1-3 nm in length ($h = 1 \sim 3$ nm in Figure 3(a)), and the nanocrystal size is precisely controlled at a critical length about 2-4 nm (Figure 3(c)). When nanocrystals of this size are tensioned, the molecular chains begin to slip stickily due to the hydrogen bonds breaking down and regeneration in this process. These phenomena not only dramatically increase the total dissipated energy of fibril deformation but also prevent the internal defects of nanocrystals from being exposed to the surrounding water and finally result in high strength, stiffness, and toughness. For nanocrystals with length larger than critical length, nanocrystals tend to be in bending mode rather than the favorable slipping mode during tension. The crack caused by unbalanced stress will be attacked by surrounding water, which leads to large-scale breaking down of hydrogen bonds followed by fiber failure [35, 36]. As shown in Figure 3(c), glycine-rich (GGX) blocks of each protein molecular chain have α -helix and random coil structure acting as the amorphous region within spider silk nanofibrils and established elastic connections between β -sheet nanocrystals. When the fiber is stretched, the amorphous region will deform due to its low modulus, and the interlocking between molecular chains effectively limits the crack propagation. Therefore, the amorphous regions composed of α -helix and random coil are generally regarded as the main contribution to the elasticity and ductility of spider silks [37].

The complex β -sheet nanocrystal and amorphous region network form spider silk nanofibrils, and the crosslinking ways of these nanofibrils will ultimately determine the product formation. For natural and artificial spider silks, fibers are spun from silk glands or artificial spinning facilities. Under the traction of the spinning process, bundles of nanofibrils are orderly aligned along the long axis of the fiber. A large number of interlocking structures between nanofibrils further strengthen the toughness of the nanofibril network and the whole spider silk fiber. Furthermore, the self-healing outer layers of natural spider silks made of lipid and glycoprotein act as shields that protect core fibers from the invasion of water, protease, and environmental microorganisms [38, 39]. As for the 2D and 3D formation of spider silk-based biomaterials, various preparation methods can be utilized via controlling the distribution and self-assembly behavior of randomly crimped spider silk nanofibers, thereby adjusting the mechanical properties to satisfy the requirement of tissue regeneration in different locations.

3. Spidroin-Based Biomaterials in Different Dimensions

3.1. One-Dimensional (1D) Spidroin-Based Biomaterials (Fiber). The spider silk fiber is a unique biomaterial with excellent mechanical properties. Compared with silk from

the silkworm, spider silk shows better biocompatibility due to the lack of sericin coating, which is a kind of high immunogenic protein that may cause serious hypertensives [40-43]. In tissue engineering, natural spider silk is usually collected from living spiders. More researchers also use recombinant spidroins to prepare recombinant spider silks through artificial spinning methods. Additionally, spider silk fibers are usually orientated in parallel as a scaffold to guide the regeneration of fibrous tissues and cells along the fiber direction [44, 45]. According to the research from Fredriksson et al., the implanted recombinant 4RepCT spider silk fiber illustrated better ability that promotes ingrowth of fibroblasts and formation of new capillaries in rats compared to the commercial medical implant Mersilk™ fiber, which shows the great potential for spider silk fiber as scaffold material in tissue engineering [46].

The strain-stress curve of spider silk illustrates a similar variation tendency like that of the tendon, and the curve has both low-strain modulus and high-strain modulus stages. Interestingly, spider silk also shows the shape memory effect which allows it to recover the initial form after deformation, such as tendon [47, 48]. Hennecke et al. reported their study of using bundles braided from natural spider silk single fiber (from female adult *Nephila* spiders ranging in age from 6 to 15 months) as sutures for tendon surgery and characterized the mechanical properties of these sutures produced using different braiding methods. Compared with conventional sutures, spider silk sutures demonstrated an excellent fatigue response and maintained high tensile strength compared to conventional ones even after 1000 fatigue cycles without any reduction [49].

Due to the outstanding tensile strength, good elasticity and long-term biodegradability of natural spider silk, especially the favorable quick adhesion of cultivated Schwann cells on silks, spider silk has become an ideal biomaterial for the construction of nerve scaffolds [50]. Radtke et al. reported their research about sheep tibial nerve defect reparation using nerve constructs composed of decellularized vein grafts and spider silk fibers. The experiment results exhibited that spider silk fibers can promote nerve tissue regeneration, axon regeneration, remyelination, and potential Schwann cells recruitment ability [51]. Roloff et al. firstly described in detail the adhesion and growth condition of human (NT2) model neurons on crossed spider silk fiber scaffolds *in vitro*. Human neurons cultured on spider silk arrays were grown along fiber direction due to the increased migration and adhesion. The newly extending neurites bridged gaps between single fibers and were elongated on neighbor fibers. Within three to four weeks, the neuron cluster and ganglion-like cell structures were observed, suggesting that the spider silk could be an excellent candidate biomaterial for enhancing neural repair in the injured central nervous system because of the neuron affinity and non-immunogenicity of the spider silks [52]. The research from Millesi et al. demonstrated a similar result that native spider silk fibers possess excellent adhesive properties and promote cell alignment, proliferation, and migration, as shown in Figure 4(a). Native spider silk fibers provide framework SCs to form Bungner bands for regrowing axons by

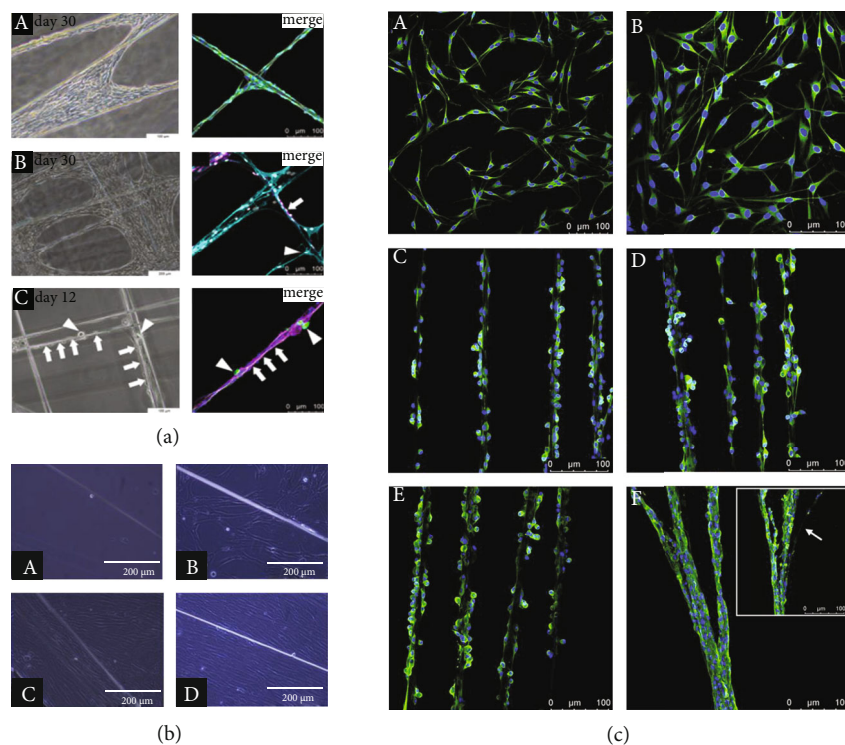


FIGURE 4: Adhesion of different cells on spider silk fibers. (a) Representative phase contrast versus confocal and immunostaining images of (A) rSCs, (B) rFBs, and (C) rDRG neurons cultured on spider silk. The merged channels of rSCs were S100 (green), VIME (grey), and DAPI (blue); the merged channels of rFBs were NGFR (magenta), THY1 (cyan), and DAPI (grey); and the merged channels of rDRG neurons were TUJ1 (beta-3-tubulin) (green), NGFR (magenta), and DAPI (blue). Arrows (left) indicate elongated rDRGs along the silk fibers, and arrows (right) indicate rFBs and rDRG neuron bodies. Reproduced from F. Millesi et al., 2021, under the Creative Commons Attribution License. (b) Images showed the proliferation and alignment of DPSCs on the spider silk over time (10x magnification). Reproduced from K. Hafner et al., 2017, Copyright © 2021, Elsevier B.V. All rights reserved. (c) Immunostaining images of rSCs cultured on (A and B) PLL/laminin-coated dishes and (C) dragline, (D) cocoon, (E) connecting, and (F) attaching silk showing S100 (green) and DAPI (blue) staining. The white arrow points towards the single silk strands that were barely perceivable. Reproduced from A. Naghilou et al., 2020, under the Creative Commons Attribution License.

supporting the repair of the inherent properties of SCS, replacing the basal laminar tube as a terrain guiding structure [53]. To further explore the potential of spider silk in tissue regeneration of the nervous system, Hafner et al. evaluated the response of human dental pulp stem cells (DPSCs) to spider dragline silk fibers, and the result is illustrated in Figure 4(b). The outcomes implied that the spider silk fiber substrate may induce stem cells to differentiate into more extended cell morphology lineages for subsequent neural differentiation applications [44].

The study from Naghilou et al. partially explained the induction mechanism of spider silk fiber on cells. They collected natural dragline silk and cocoon silk from *N. edulis* and the connecting and attaching silk from *A. avicularia*, investigated the material characteristics of each kind of silk samples, and correlated their ability to act as a guiding structure for rat Schwann cells (rSCs) during *in vitro* experiments. Compared to other three kinds of spider silk fibers, the β -sheet content of attaching silks decreased significantly, which led to severe adhesion of fibers in the medium and the production of cell aggregates. Meanwhile, the successful guiding behaviors of rSCs on dragline silk, cocoon silk, and connecting silk are observed, as shown in Figure 4(c). The

experiment result exhibited the necessity of higher β -sheet content in spider silk fiber for fabricating nerve guidance conduits by guaranteeing the fiber to be straight and stiff in the medium [54].

Kornfeld et al. repeated the sheep tibial nerve defect reparation experiment using the similar spider silk-based implant, quantified the axonal regeneration rate, and determined the *in vivo* degradation mechanism and rate of spider silk fibers. Surprisingly, the axonal regeneration rate occurred on a spidroin-based implant with a directional velocity of 1.309 mm/d, close to that of autologous nerve transplant (1.57 mm/d, the ideal axonal regeneration rate). The implanted spider silks could be fully degraded through the photoimmune response mainly mediated by Langerhans giant cells within 3 months, so that the constructs could be replaced by an autologous matrix [55].

3.2. Two-Dimensional (2D) Spidroin-Based Biomaterials

3.2.1. Nonwoven Mesh. Electrospinning is widely used in tissue engineering and usually has good compatibility with biological tissues. Unlike the weaving method, electrospinning can produce ultrathin nonwoven textile with a large specific

surface [56, 57] and even mimic the histological structures through electrospinning process design [58]. Limited by the yield of natural spidroin, the recombinant spidroin produced by genetically engineered bacteria (e.g., *Escherichia coli*) or yeasts (e.g., *Pichia pastoris*) is adopted as raw material [59]. In order to inhibit the self-assembly of spidroin molecular chains, the strongly polar solvent hexafluoroisopropanol (HFIP) and formic acid are generally selected for distributing purified spidroins [60]. However, a more mild and biocompatible Tris/HCl buffer plus PEO400 is suggested as a solvent for biomedical use nonwoven mesh to avoid the tissue irritation brought from polar solvent [61]. After spinning, posttreatment is also required, such as methanol or ethanol steam bath, since they can transform α -helix structures into β -sheet structures to endow mesh with better water resistance and water stability [60, 62].

Leal-Egaña et al. examined nonwoven mesh, film, and hydrogel scaffolds made of eADF4(C16) and evaluated the cell adhesion and proliferation on these substrates. Among the three candidate materials, the nonwoven mesh showed the highest potential on fibroblast adhesion and proliferation, which was attributed to the higher availability of cell attachment surface in the daedal surface structure of nonwovens, allowing faster production of filaments around fibers. Furthermore, their experiment also described the proper fiber diameter ranges, i.e., ideal cell adhesion of 500~1500 nm and good proliferation of 1000~2000 nm [28]. This research provides valuable information for the surface design of nonwoven mesh. The research about using pNSR16/PVA nonwoven mesh as a wound dressing to accelerate wound healing was reported by Zhao et al. [63]. During the healing period, the nonwoven mesh could effectively promote cell adhesion, proliferation, and migration, and faster formation of granular groups and wound contraction were also observed in the experimental group.

In addition, the recombinant spidroin-based nonwoven mesh also has broad application prospects in the field of nerve repair. In the study of Pawar et al., aligned collagen fibers were packaged with eADF(C16) nonwoven mesh to prepare a nerve catheter, and the spidroin shell was also chemically modified to enhance its cellular accessibility. In this research, the aligned fibers caused no cell toxicity during the 3-week incubation period. The surface structure of spidroin mesh provided ideal attaching sites for cells required for nerve regeneration. This porous shell also maintained the transportation of nutrition, gases, and waste metabolites around nerve defects [64].

3.2.2. Film. Spidroin films can be manufactured through the conventional film-forming methods, e.g., casting and spin coating, and the choice of solvent will significantly influence secondary structure change in the film; for instance, the films made from formic acid or aqueous solution demonstrate higher β -sheet concentration, while using HFIP as solvent will lead to high α -helix concentration in the film after solvent evaporation and posttreatments are required [60, 65, 66]. Generally, the water annealing (121°C hot steam treatment), salt solutions (e.g., 1 M K_2PO_4 solution), and primary alcohol solution or steam are used to transform part of α -

helix into β -sheet to enhance the water stability and mechanical properties of films [18, 67, 68].

Various physical-chemical and genetic modifications can be applied to the film's surface structure to achieve better cell adhesion and cell fate control or to import specific properties. Micropatterns could improve cell adhesion and adjust cell orientation on the film surface [28, 69]. Meanwhile, micropatterns on the film surface can also prevent microbial infestation as antibacterial layers [70]. Commonly, microscale patterns are created through capillary transfer lithography (CTL) and solvent-assisted microcontact molding (SAMIM) using a PDMS mold as shown in Figure 5(a) [70, 71], and Figure 5(b) illustrates the research from Molina et al., where they reported a technology utilizing the directing ability of complementary DNA strands and spidroin self-assembly induced by phosphate ions to form nanoscale patterns on the inorganic surface [72].

Besides surface micropatterns, different kinds of cell bonding peptides were also researched to promote the cell adhesion capability of the spidroin molecular chain. The integrin-binding motif RGD from fibronectin was firstly investigated and connected to the spidroin sequence through genetic editing. The RGD-modified film surface demonstrated enhanced cell adhesion, which may be due to the interaction of nonspecific cells in protein molecules with charged residues [26, 73, 74]. Furthermore, different cells also illustrated various responses on different motif-modified films. For example, Schwann cells have been shown to adhere to matrices with IKVAV motifs, with dispersed morphology and improved viability [26, 75]. Silk materials can also be functionalized with oligosaccharides, acrylates, and other synthetic polymers to improve cell adhesion [76]. The alkyne-capped-PMAGal derivatives were linked with the azidopropylamine-modified eADF4(C16) film, showing up to 80% cell attachment compared with 69% of the unmodified membrane [77].

3.3. Three-Dimensional (3D) Spidroin-Based Biomaterials

3.3.1. Hydrogel. Hydrogels are three-dimensional (3D) cross-linked polymer networks with high water content (above 95% *w/w*) and high adsorption capacity [78, 79]. Various natural and synthetic-derived polymers, such as sodium alginate, collagen, hyaluronic acid, chitosan, silk, gelatin, polyvinyl alcohol (PVA), and polyacrylic acid (PAA), have been processed into hydrogels via physical or chemical crosslinking for a wide range of biomedical applications [45, 80]. Due to the excellent mechanical properties and similarity to ECM, hydrogels based on spider silk proteins have been widely explored and utilized, especially in the fields of tissue engineering, drug delivery, and biomanufacturing.

The hydrogel structure can be generated from spider silk protein solutions through a sol-gel transformation. In the process of gelation, spider silk proteins are driven by hydrophobic interactions and hydrogen bonds to self-assemble into β -sheets [81–83]. Generally, adjusting physical crosslinking conditions, such as the concentration of the spidroin solution and additives, pH value, ionic composition of the solution, or shear force, can control the gelation time and

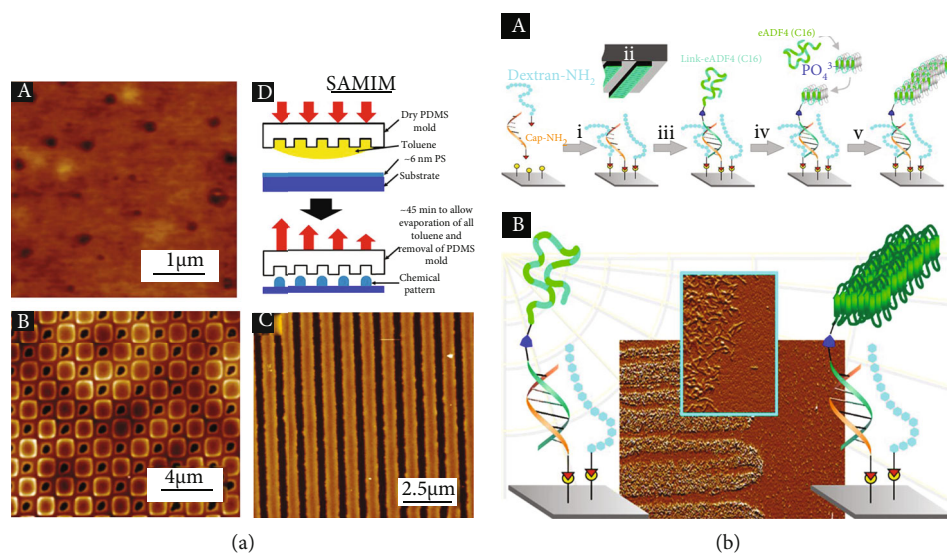


FIGURE 5: Using different techniques for patterning materials of recombinant spider silk proteins. (a) AFM images showing the morphology of C16 films from HFIP: (A) surface morphology with a Z scales of 10 nm, (B) square pattern with a Z scale of 60 nm, (C) line pattern using the SAMIM technique with a Z scale of 60 nm, and (D) representation of the SAMIM technique. Reproduced from S. L. Young et al., 2012, Copyright © 2012, American Chemical Society. (b) (A) Schematic representation of soft lithography-based patterning for localized fibril self-assembly. The silicon surface was activated by the epoxy group, enabling the simultaneous introduction of the capture 5'-amino oligonucleotides (cap-NH₂) and passivation agents (i). A microcontact printing technique (ii) was used to pattern DNA-spider silk conjugates (link-eADF4(C16)) (iii). The surfaces were treated with phosphate ions and monomeric spider silk protein eADF4(C16) to nucleate (iv) which led to the growth of surface bound β -sheet rich fibrils on the spotted conjugates. (B) Schematic diagram of surface microstructure formed by self-assembly of spidroin molecular chains. Reproduced from A. Molina et al., 2019, Copyright © 2018, American Chemical Society.

enhance the stability of the hydrogel [84]. Schacht and Scheibel explored a duplicable approach for hydrogel formation of engineered and recombinantly produced the spider silk protein eADF4(C16), in which the low-concentration protein was denatured in 6 M GdmSCN and then dialyzed against 10 mM Tris/HCl (pH 7.5). With increasing protein concentration, the formation of β -sheet-rich nanofibrils of eADF4(C16) is accompanied by gelation [85].

The use of chemical crosslinkers is also an effective method to stabilize the three-dimensional structure of hydrogels. To prevent hydrogel from being damaged by agitation or shearing, Rammensee et al. treated the surface of C16 hydrogels with ammonium peroxodisulfate (APS) and tris(2,2'-bipyridyl)dichlororuthenium (II) (Rubpy) to connect the tyrosine side chains of the spidroins. The shear modulus of the noncrosslinked C16 silk hydrogel and cross-linked hydrogel was about 38 Pa and 820 Pa, respectively [86]. Neubauer et al. demonstrated the recombinant spider silk protein eADF4(C16) assembly into fibrils in the presence of DMSO/DMF in water-soluble organic cosolvents. The tris-hydrogels and gels in DMSO blend exhibited the highest β -sheet content ($39 \pm 1\%$), whereas the gels in the presence of water and DMF blends showed far fewer β -sheets of $24 \pm 5\%$ and $22 \pm 4\%$, respectively. In addition, the above-mentioned recombinant spider silk hydrogel exhibited excellent shear-thinning characteristics with respect to the protection of encapsulated cells or drugs from corrosive shear stress. The authors further used the 3D printing method to fabricate multilayer scaffolds with high

shape stability, which could be applied to a 3D printing drug storehouse [87]. The addition of nanoparticles has recently been proven to be an important factor in enhancing hydrogels' adhesion and mechanical properties [88]. Liu's group reported on artificial spider silks produced by the water evaporation-induced self-assembly of hydrogel fiber consisting of polyacrylic acid and silica nanoparticles. The mechanical properties of the ultimate fiber were comparable to those of spider silk, presenting a tensile property of 44.3%, a tensile strength of 895 MPa, a toughness of 370 MJ m^{-3} , and a damping capacity of 95% [89].

3.3.2. Porous Sponge. Matrix stiffness is increasingly appreciated as a critical mediator of cell behavior to regulate cell signaling, with effects on growth, survival, and motility [90, 91]. Hydrogel showed poor stability in cell and tissue culture, whereas the 3D scaffolds with a particular content of stiffness can promote cell adhesion and proliferation, generate a new extracellular matrix, promote tissue growth, and promote the transport of nutrients and metabolites. Although a number of methods have been used to prepare silk-based scaffolds [17, 92–95], the salt leaching method is widely used due to its effectiveness, efficiency, and ease of the process. NaCl crystals allowed the production of β -sheet-rich scaffolds with a high porosity without the need of additives or crosslinkers for mechanical stabilization, as well as leaving a gap in practicability for some soft tissues. Therefore, choosing a porous and mechanically stable silk salt-leached matrix to match the stiffness of soft tissue will provide

additional options for developing spider silk biomaterials in soft tissue regeneration.

In Agapov's study, the three-dimensional scaffold based on recombinant protein 1 was produced by leaching. After 24 h of cultivation, the cells were mainly distributed on the surface of the scaffold, and only a few cells were detected at depths over 200 μm from the scaffold surface. The cell density averaged for all layers was 355 ± 64 cells per 1 mm of the scaffold. After 4 days of cultivation, fibroblast nuclei were detected in the deep pore wall of the scaffold, indicating that the scaffold had good compatibility and could provide efficient cell adhesion and proliferation over a long time period [96]. Moisenovich et al. have previously generated porous scaffolds from a genetically engineered protein, an analog of *N. clavipes* spidroin 1 known as rS1/9. The salt leaching technique was used to make the rS1/9 scaffolds of interconnected porous structures with spontaneously formed micropores. The 3T3 fibroblasts proliferated in the rS1/9 scaffold and distributed uniformly between the surface and deeper layers (about 27% and 33%, respectively), whereas the initial distribution was about 58% and 11%, respectively [97]. In the 8-week subcutaneous transplantation experiment, compared with the control group, the nerve fibers on rS1/9 scaffolds showed deeper penetration in the process of vascularization and regeneration of connective tissue in BALB/c mice [98].

Surface modification of various biomaterials is a promising method to endow the biofunctionality at the material-tissue interface to modulate biological responses [99, 100]. Schacht et al. fabricated highly porous foams made of the recombinant spider silk protein eADF4(C16) containing an RGD-binding motif to prepare highly porous foam through the salt leaching method, thereby obtaining mechanically robust scaffolds. The results showed an improved adhesion and proliferation of fibroblast on eADF4(C16)-RGD foam, indicating the potential applications in soft tissue engineering and tissue repair [101]. These studies confirmed that the combination of salt leaching and spidroins pretreatment was a practical approach to tune the scaffolds to produce a mechanical system closer to softer natural tissues.

4. Spidroin-Based Biomaterials for Regenerative Therapies

The existing knowledge of spidroin-based biomaterials in terms of structure and function provides a theoretical basis for the design and synthesis of new spider silk protein biomaterials. In addition, genetic engineering techniques can also be used to add gene sequences of new peptides or domains to the coding sequence of spider silk proteins to endow new functions. In this section, we discussed the potential of genetic engineering of spider silk protein in the preparation and drug delivery of lung tissue engineering and also discussed the application status of combining stem cells and spider protein-based biomaterials in the field of tissue engineering.

4.1. Lung Tissue Engineering. An effective strategy for the development of the tissue-engineered lung is to simulate

the architecture of capillary conduits in the lung tissue, which are covered with monolayer epithelial cells and have a large surface area conducive to gas diffusion between the external environment and blood [102]. The spider silk membrane (thickness $> 3 \mu\text{m}$) has been extensively investigated for the replacements of the retinal pigment epithelium, bone grafts, and corneal implants due to its biocompatibility, degradability, and molecular permeability, but this micro-scaled structure is not suitable for the replacement of ultrathin alveoli tissue. Bearing in mind such limitations, Gustafsson et al.'s group fabricated ultrathin nanofilms ($\sim 250 \text{ nm}$) based on the self-assembly of recombinant spider silk proteins at the liquid-air interface of a standing aqueous solution (as shown in Figure 6(a)). The nanomembrane displayed a high elasticity and toughness, contributed to the permeability of human plasma proteins, and promoted cells to form a confluent monolayer within three days [103]. In addition, the thickness of nanofilms could be tightly controlled by adjusting silk concentration, and those well-designed structures show encouraging prospects in terms of the cocultured system with the different types of cells, which opens the door to develop an *in vitro* lung tissue model based on the coculturing cells upon the ultrathin membrane [104].

Pulmonary surfactant (PS) is a surface-active lipoprotein complex with hydrophilic and hydrophobic properties, which reduces the expansion force by adsorbing on the liquid and air interface of the alveoli, thereby avoiding the alveoli collapse. Nowadays, the lack of PS has been proven to be the leading cause of neonatal and pediatric respiratory diseases, so the research and development of PS artificial preparation have become a research hotspot. However, PS is prone to aggregate due to the unstable secondary structure [105], which may severely impede the production of recombinant PS proteins. In the process of producing high-viscosity spider silk proteins, spiders will separate protein regions with aggregation tendency into micellar structures, and the shell of micellar structure is the N-terminal domain (NT) of protein. Inspired by this idea, Kronqvist et al.'s group designed a mutant spider silk protein domain, NT*, exhibiting markedly increased solubility, stability, and refolding capacity. They further developed the recombinant PS with an NT* fusion tag, which showed low cost, high yield, and few purification steps. By comparing the synthetic PS with the analog biological products on the market, it is found that it can effectively reduce the lung surface tension of the animal model of infant respiratory distress syndrome, which provides a promising prospect for the artificial production of low-cost PS for the treatment of various lung diseases [106].

Compared with tissue engineering scaffolds for other organs, besides the conventional requirements for scaffolds, lung tissue engineering puts forward higher needs, such as sufficient mechanical strength and elasticity to provide tensile stress similar to the natural lung, thereby offering the necessary distensibility of the lung when breathing. Meanwhile, an appropriate microcirculation structure is also required to achieve gas and nutrition exchange. Surprisingly, the research of Gustafsson et al.'s

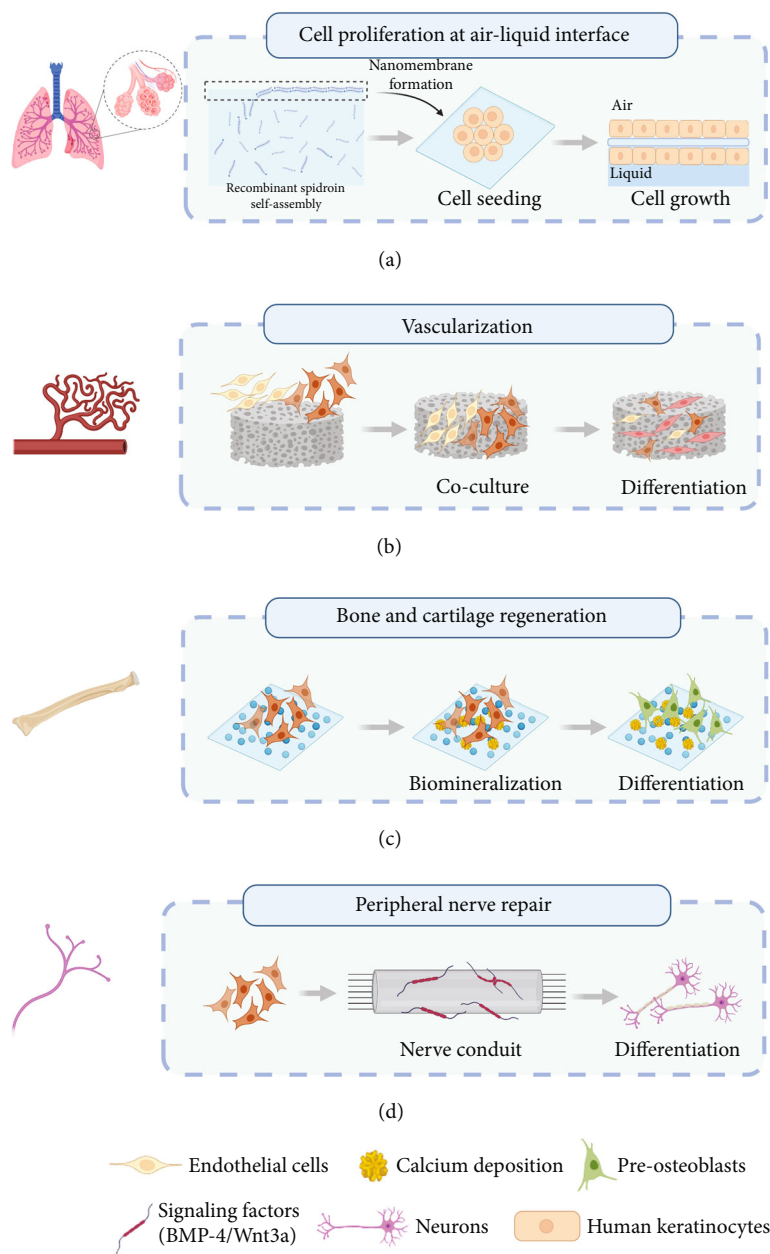


FIGURE 6: Schematic illustration of spidroin-based biomaterials for various tissue engineering applications. (a) For lung tissue engineering, FN-4RepCT silk protein forms a layer of nanofibrils via self-assembling at the liquid-air interface. The membrane enables the rapid formation of a confluent cell layer of human keratinocytes on either side. (b) For vascularization, the endothelial cells (ECs) and mesenchymal stem cells (MSCs) were cocultured on the recombinant spider silk (4RepCT) foams, and it was found that MSCs grew millimeter long branched sprouts in the foam within two weeks. (c) For bone and cartilage regeneration, the bone marrow mesenchymal stem cells (hMSCs) cultured on recombinant protein films can promote osteogenic differentiation by enhancing biomineralization. (d) For peripheral nerve repair, the neural stem cells (NSCs) cultured on the 4RepCT matrices differentiated efficiently into neurons after processing the recombinant protein including the extracellular signaling factor BMP4 or a combination of BMP4 and the signaling factor Wnt3a.

and Kronqvist et al.'s groups has achieved partial functions that scaffolds for lung tissue engineering need, including recombinant pulmonary surfactant and cell proliferation at the air-liquid interface, which indicates the great possibility of using a spidroin-based scaffold for lung tissue engineering.

4.2. Vascularization. The investigation of tissue-engineered vascular constructs (TEVs) is being vigorously pursued by converging multidisciplinary approaches in recent years. The goal of producing engineered blood vessels is to construct a living neovessel with similar architecture and biological functions to the native blood vessel. However, the

artificial blood vessels in the early phase generally exhibited instability due to the lack of vascular resistance and poor mechanical strength of the vessel walls. Spider silks have been shown in various studies due to their improved mechanical properties, inherent biocompatibility and biodegradability, relative ease of processing [49, 107], and weaker immunological reactions compared to other materials (e.g., PLA and collagen) [108]. These features recommend spider silk-based scaffolds as suitable alternatives for the development of vascular tissue engineering. Although a variety of cell types have been utilized to fabricate TEVs, approaches to using stem cells can overcome the limitations of using differentiated vascular phenotypes and reduce the preparation time of TEVs. Johansson et al. developed 3D foams based on a recombinant spider silk protein (4RepCT; consisting of the C-terminal domain and four tandem repeats of the major ampullate spidroin-1). The pluripotent and multipotent stem cells were seeded on the 3D culture to investigate their applicability for efficient differentiation. The outcomes demonstrated that the human embryonic stem cells (hESC) were aggregated and integrated within the 3D structure of silk foam after culturing 48 h. Endodermal differentiation was further examined by the mRNA expression experiment, confirming robust upregulation of the endodermal progenitor marker SOX17 and downregulation of pluripotency (NANOG). Figure 6(b) shows a further examination of organizational capacity for generating microvessels; the endothelial cells (ECs) and mesenchymal stem cells (MSCs) were cocultured, and it was found that MSCs grew millimeter long branched sprouts in the silk within two weeks [109].

4.3. Bone and Cartilage Regeneration. The mechanical strength, resilience, and flexibility of spider silk are superior to those of other natural polymers and most synthetic materials, exhibiting even high-performance fibers such as Kevlar, holding great promise for the development of a bone-related functional scaffold [110]. Many studies have focused on enhancing bone regeneration of spider silk-based composite materials by improving the mineralization of the bone matrix. Dinjaski et al. fused the hydroxyapatite-binding domain VTKHLNQLSISQSY (VTK) separately to the N-, C-, or both terminals of the spider silk to investigate the effect of VTK position on the properties of biomaterials and biomineralization. The hMSCs were cultured on the surface of the silk-VTK fusion protein films to verify the effect of the recombinant protein membrane on promoting osteogenesis *in vitro*. As shown in Figure 6(c), the elongated morphology of hMSCs was observed on all test surfaces after 14 days, indicating that hMSCs grew healthily and an absence of cytotoxicity to the recombinant silk-VTK proteins. The outcomes also showed that the recombinant fusion harboring VTK domains on both the N- and C-termini produced the highest amount of bone sialoprotein deposition and calcium deposition, indicating the potential to induce hMSC differentiation [111]. Hardy et al. fabricated films consisting of poly(butylene terephthalate) (PBT) or poly(butylene terephthalate-co-poly(alkylene glycol) terephthalate) (PBTAT) and an engineered spider silk protein (eADF4(C16)). The

calcium phosphate mineralized films possessed multiple carboxylic acid moieties capable of binding calcium ions, which can facilitate biomineralization with calcium carbonate or calcium phosphate. Qualitative analysis of alkaline phosphatase (ALP) activity showed that hMSCs on the membrane could differentiate into osteoblasts [112]. The authors further explored the effect of photochemical modification on spider silk protein-based films. The eADF4(C16) films were firstly immersed in pure monomers (e.g., allylamine, acrylic acid, and methacrylic acid), exposed to ultraviolet light for 48 h, and then washed and dried in a vacuum. This approach led to the generation of free radicals on the silk protein backbone and produced a functional polymer coating after grafting the synthetic polymers, thereby further enhancing the mineralization of calcium carbonate [113].

4.4. Peripheral Nerve Repair. In the clinical management of nerve gap repair, the treatment effect of injured patients is not as good as expected. Effective repair also becomes progressively more difficult with the increase in the nerve gap. To overcome these limitations, nerve conduit strategies based on spider silk scaffolds were proposed to meet the clinical demands and requirements of large-gap nerve repair. Lewicka et al. proved that the recombinant spider silk protein 4RepCT offered a suitable substrate for the culture of rodent cortical neural stem cells (NSCs). These cells can proliferate, survive, and efficiently differentiate into a variety of cell types on the 4RepCT-based membrane structure without any additional coating or animal-derived components [114]. They further processed recombinant proteins with the extracellular signaling factor BMP-4 or a combination of the signaling factor Wnt3a and BMP-4. As shown in Figure 6(d), it was found that cultured cortical NSCs in 4RepCT foam-like structures could be effectively and efficiently differentiated into neurons responsive to glutamate receptor agonists (such as AMPA) [115]. Astrand et al. created a centimeter-sized foam as an ideal stem cell niche by using recombinant spider silk protein modifying fibronectin- (FN-silk-) binding motif and a human recombinant laminin 521 (LN-521). In this 3D structure, human pluripotent stem cells (hPSC) developed into 3D cell constructs supported by a microfibrillar network. After the initial expansion, neurons will be induced to differentiate into a continuous layer of neuroectodermal tissue and further differentiate into neuronal subtypes [116].

Another ideal source of stem cells proposed for neural regeneration is DPSCs because of their close relationship with the embryonic origin of neurons and easily available properties. Hafner et al. explored the effects of dragline silks on cellular attachments and proliferation of DPSCs. The outcomes demonstrated that the spider silk fibers have good biocompatibility and are free of an immunogenic sericin coat [117]. The *in vitro* cell experiment results showed that DPSCs had a larger tendency of arrangement and extension on the spider silk matrix, while fibroblasts and osteoblasts had a smaller tendency of arrangement and extension, suggesting that these fibers may also be recognized as an effective matrix for DPSCs to differentiate along more elongated cell morphology under appropriate growth environment [44].

5. Conclusion and Perspective

Good biocompatibility, nonimmunogenicity, biodegradability, and comprehensive mechanical properties endow spidroin material with great potential in tissue engineering. At present, a small amount of spidroin can be obtained directly from nature. The use of genetically modified bacteria or fungi is still the primary way to produce recombinant spidroin on a large scale. Recombinant spidroin can be processed into materials of different dimensions to meet the requirements of different tissue morphology, structures, and mechanical properties. This review briefly introduced the characteristics of spidroin materials, the preparation methods of different dimensional scaffolds, and their applications in lung tissue engineering, vascular tissue engineering, bone tissue engineering, and nerve repair tissue engineering. Although there are few *in vivo* studies of spidroin materials in the lung tissue engineering area, we still make a brief overview and summary. For the spidroin-based scaffold used for different tissue engineering, there are still a lot of functions and characteristics to be realized, such as the complex multilevel structure and stability and selective permeability under certain mechanical properties. We still firmly believe that these goals can be achieved by applying new manufacturing methods and further understanding the relationship between the structure, component, and properties of spidroin-based biomaterials.

The ECM of each organ possesses a very complex and unique structure, components, and unique cell regulatory mechanism. Therefore, in order to fully simulate the structure and function of the engine control module, it is necessary to design a multidimensional framework structure to realize the multilevel regulation of cell growth, differentiation, and migration. The framework material can respond to multiple fields (such as force, heat, light, electricity, and magnetism) to enhance the interaction between scaffold and tissue cells. In the future, a variety of processing methods can be conjunctively used to realize the precision manufacturing of complex structures, which is conducive to the preparation of complex structures with performance gradients and anisotropy [118, 119]. For example, 4D printing technology can make the scaffold respond to stimulation and provide more ways for cell fate regulation, which involves a full understanding and fine control of various components of spider silk protein.

In addition, the ultrahigh production cost of recombinant spidroin may become the major obstacle to the industrial production and large-scale application of the recombinant spidroin-based fiber or scaffold. As AMSilk [120] (a German company specializing in high-performance spidroin-based biopolymer) claimed in 2011, the cost of per-kilogram of recombinant spidroin is around €100,000 (~\$137,500) if there is no complete reinvention on production processes, and it is also close to the estimation from Kraig Biocraft Lab [121] in 2018 that the high yield of 20 grams of protein per liter of fermentation broth is \$35,000~\$37,500. Meanwhile, the environmental and health impacts and costs of solvents in the manufacturing process cannot be ignored. The corrosive, irritant, and environmentally harmful solvents (e.g., HFIP

[28, 64], GdmSCN [74, 122], and formic acid [63]) are frequently adopted to dissolve recombinant spidroins for subsequent procedures due to their excellent ability to anti-self-assembly of spidroins, which definitely increases the operational risk and environmental issues. Fortunately, there is a new trend that uses gentle and environmentally friendly aqueous solvent when preparing a spidroin-based film or scaffold used for tissue engineering [57], such as Tris-HCl, SDS, and PEO400. Correspondingly, increasing the protein concentration within these solvents becomes a new challenge. Based on the above reasons, preparing polymers to simulate the various characteristic components and hierarchical structure of natural spider silk through chemical synthesis methods will also become a research hotspot, which is expected to reduce the production cost of preparing artificial spider silk significantly [123, 124]. However, the biocompatibility, degradation performance, immunogenicity, and processability of artificial spider silk protein prepared by chemical methods still need to be further studied.

Data Availability

The figures and data supporting this review are adopted from previously reported studies and datasets, these studies have been cited, and permissions have been obtained.

Conflicts of Interest

The authors declare that they have no conflicts of interest.

Authors' Contributions

Jinlian Hu, Qi Zhang, and Min Li contributed to the conception of this review. Qi Zhang and Min Li performed the literature research, prepared the original draft, and created figures. Qi Zhang, Min Li, Jinlian Hu, Wenbo Hu, and Xin Wang participated in revising and finalizing the paper. All authors read and approved the final manuscript. Qi Zhang and Min Li contributed equally to this work. Qi Zhang and Min Li are the co-first authors.

Acknowledgments

The authors gratefully acknowledge the financial support from the General Research Fund ("Developing Spider-Silk-Model Artificial Fibers by A Chemical Synthetic Approach," Grant No. 9042934), the National Natural Science Foundation of China ("High-Performance Fiber Material with Hierarchical Structure Imitating Spider Silk," Grant No. 52073241), the National Natural Science Foundation of China ("Study of Multiresponsive Shape Memory Polyurethane Nanocomposites Inspired by Natural Fibers," Grant No. 51673162), and the Startup Grant of CityU ("Laboratory of Wearable Materials for Healthcare," Grant No. 9380116).

References

- [1] R. Lewis, "Unraveling the Weave of Spider Silk," *Bioscience*, vol. 46, no. 9, pp. 636–638, 1996.

- [2] S. Heimer, *Wunderbare Welt Der Spinnen*, Urania Verlag, 1988.
- [3] S. Wright and S. L. Goodacre, "Evidence for antimicrobial activity associated with common house spider silk," *BMC Research Notes*, vol. 5, no. 1, p. 326, 2012.
- [4] T. A. Blackledge and C. Y. Hayashi, "Silken toolkits: biomechanics of silk fibers spun by the orb web spider *Argiope argentata* (Fabricius 1775)," *The Journal of Experimental Biology*, vol. 209, no. 13, pp. 2452–2461, 2006.
- [5] F. Vollrath, "Strength and structure of spiders' silks," *Reviews in Molecular Biotechnology*, vol. 74, no. 2, pp. 67–83, 2000.
- [6] J. R. Griffiths and V. R. Salaniti, "The strength of spider silk," *Journal of Materials Science*, vol. 15, no. 2, pp. 491–496, 1980.
- [7] F. Vollrath and D. P. Knight, "Liquid crystalline spinning of spider silk," *Nature*, vol. 410, no. 6828, pp. 541–548, 2001.
- [8] M. P. Nikolova and M. S. Chavali, "Recent advances in biomaterials for 3D scaffolds: A review," *Bioactive Materials*, vol. 4, pp. 271–292, 2019.
- [9] R. Lanza, R. Langer, J. P. Vacanti, and A. Atala, *Principles of Tissue Engineering*, Academic Press, 2020.
- [10] B. Alberts, D. Bray, K. Hopkin et al., *Essential Cell Biology*, Garland Science, 2015.
- [11] C. A. van Blitterswijk, *Tissue Engineering*, Academic, London, 2007.
- [12] R. O. Hynes and A. Naba, "Overview of the Matrisome—An Inventory of Extracellular Matrix Constituents and Functions," *Cold Spring Harbor Perspectives in Biology*, vol. 4, no. 1, article a004903, 2012.
- [13] J. K. Mouw, G. Ou, and V. M. Weaver, "Extracellular matrix assembly: a multiscale deconstruction," *Nature Reviews Molecular Cell Biology*, vol. 15, no. 12, pp. 771–785, 2014.
- [14] A. Przekora, "The summary of the most important cell-biomaterial interactions that need to be considered during in vitro biocompatibility testing of bone scaffolds for tissue engineering applications," *Materials Science and Engineering: C*, vol. 97, pp. 1036–1051, 2019.
- [15] S. Naahidi, M. Jafari, M. Logan et al., "Biocompatibility of hydrogel-based scaffolds for tissue engineering applications," *Biotechnology Advances*, vol. 35, no. 5, pp. 530–544, 2017.
- [16] C. F. Guimarães, L. Gasperini, A. P. Marques, and R. L. Reis, "The stiffness of living tissues and its implications for tissue engineering," *Nature Reviews Materials*, vol. 5, no. 5, pp. 351–370, 2020.
- [17] M. Zhu, Q. Feng, and L. Bian, "Differential effect of hypoxia on human mesenchymal stem cell chondrogenesis and hypertrophy in hyaluronic acid hydrogels," *Acta Biomaterialia*, vol. 10, no. 3, pp. 1333–1340, 2014.
- [18] H.-J. Jin and D. L. Kaplan, "Mechanism of silk processing in insects and spiders," *Nature*, vol. 424, no. 6952, pp. 1057–1061, 2003.
- [19] F. M. Chen and X. Liu, "Advancing biomaterials of human origin for tissue engineering," *Progress in Polymer Science*, vol. 53, pp. 86–168, 2016.
- [20] B. P. Chan and K. W. Leong, "Scaffolding in tissue engineering: general approaches and tissue-specific considerations," *European Spine Journal*, vol. 17, Supplement 4, pp. 467–479, 2008.
- [21] A. I. Teixeira, O. Hermanson, and C. Werner, "Designing and Engineering Stem Cell Niches," *MRS Bulletin*, vol. 35, no. 8, pp. 591–596, 2010.
- [22] N. R. Blumenthal, O. Hermanson, B. Heimrich, and V. P. Shastri, "Stochastic nanoroughness modulates neuron–astrocyte interactions and function via mechanosensing cation channels," *Proceedings of the National Academy of Sciences of the United States of America*, vol. 111, no. 45, pp. 16124–16129, 2014.
- [23] Z. Gao, S. Wang, H. Zhu, C. Su, G. Xu, and X. Lian, "Using selected uniform cells in round shape with a micropipette to measure cell adhesion strength on silk fibroin-based materials," *Materials Science and Engineering: C*, vol. 28, no. 8, pp. 1227–1235, 2008.
- [24] J. Y. Kim, "Low molecular weight silk fibroin increases alkaline phosphatase and type I collagen expression in MG63 cells," *Journal of Oral and Maxillofacial Surgery*, vol. 72, no. 9, article e174, 2014.
- [25] L. Jeong, I. S. Yeo, H. N. Kim et al., "Plasma-treated silk fibroin nanofibers for skin regeneration," *International Journal of Biological Macromolecules*, vol. 44, no. 3, pp. 222–228, 2009.
- [26] M. Widhe, U. Johansson, C. O. Hillerdahl, and M. Hedhammar, "Recombinant spider silk with cell binding motifs for specific adherence of cells," *Biomaterials*, vol. 34, no. 33, pp. 8223–8234, 2013.
- [27] J. Johansson and A. Rising, "Evaluation of Functionalized Spider Silk Matrices: Choice of Cell Types and Controls are Important for Detecting Specific Effects," *Frontiers in Bioengineering and Biotechnology*, vol. 2, p. 50, 2014.
- [28] A. Leal-Egaña, G. Lang, C. Mauerer et al., "Interactions of Fibroblasts with Different Morphologies Made of an Engineered Spider Silk Protein," *Advanced Engineering Materials*, vol. 14, no. 3, pp. B67–B75, 2012.
- [29] J. M. Gosline, P. A. Guerette, C. S. Ortlepp, and K. N. Savage, "The mechanical design of spider silks: from fibroin sequence to mechanical function," *The Journal of Experimental Biology*, vol. 202, no. 23, pp. 3295–3303, 1999.
- [30] G. Yang, K. Gu, and Z. Shao, "The Investigation from Animal Silks to Silk Protein-based Materials," *Acta Polymerica Sinica*, vol. 52, p. 16, 2021.
- [31] A. Rising and J. Johansson, "Toward spinning artificial spider silk," *Nature Chemical Biology*, vol. 11, no. 5, pp. 309–315, 2015.
- [32] W. A. Gaines IV and W. R. Marcotte Jr., "Identification and characterization of multiple *Spidroin* 1 genes encoding major ampullate silk proteins in *Nephila clavipes*," *Insect Molecular Biology*, vol. 17, no. 5, pp. 465–474, 2008.
- [33] D. N. Breslauer and D. L. Kaplan, "9.04 - Silks," in *Polymer Science: A Comprehensive Reference*, K. Matyjaszewski and M. B. T.-P. S. A. C. R. Möller, Eds., pp. 57–69, Elsevier, Amsterdam, 2012.
- [34] L. Eisoldt, A. Smith, and T. Scheibel, "Decoding the secrets of spider silk," *Materials Today*, vol. 14, no. 3, pp. 80–86, 2011.
- [35] S. Ling, D. L. Kaplan, and M. J. Buehler, "Nanofibrils in nature and materials engineering," *Nature Reviews Materials*, vol. 3, no. 4, p. 1, 2018.
- [36] S. Keten, Z. Xu, B. Ihle, and M. J. Buehler, "Nanoconfinement controls stiffness, strength and mechanical toughness of β -sheet crystals in silk," *Nature Materials*, vol. 9, no. 4, pp. 359–367, 2010.
- [37] W. Qiu, A. Patil, F. Hu, and X. Y. Liu, "Hierarchical Structure of Silk Materials Versus Mechanical Performance and Mesoscopic Engineering Principles," *Small*, vol. 15, no. 51, p. 1903948, 2019.


- [38] K. Yazawa, A. D. Malay, H. Masunaga, and K. Numata, "Role of Skin Layers on Mechanical Properties and Supercontraction of Spider Dragline Silk Fiber," *Macromolecular Bioscience*, vol. 19, no. 3, p. 1970006, 2019.
- [39] A. Sponner, W. Vater, S. Monajembashi, E. Unger, F. Grosse, and K. Weisshart, "Composition and Hierarchical Organisation of a Spider Silk," *PLoS One*, vol. 2, no. 10, p. e998, 2007.
- [40] G. H. Altman, F. Diaz, C. Jakuba et al., "Silk-based biomaterials," *Biomaterials*, vol. 24, no. 3, pp. 401–416, 2003.
- [41] F. Vollrath, P. Barth, A. Basedow, W. Engström, and H. List, "Preface," *In Vivo*, vol. 16, no. 4, p. 229, 2002.
- [42] C. Allmeling, A. Jokuszies, K. Reimers et al., "Spider silk fibres in artificial nerve constructs promote peripheral nerve regeneration," *Cell Proliferation*, vol. 41, no. 3, pp. 408–420, 2008.
- [43] H. Venkatesan, J. Chen, and J. Hu, "Fibers Made of Recombinant Spidroins — A Brief Review," *AATCC Journal of Research*, vol. 6, no. 3, pp. 37–40, 2019.
- [44] K. Hafner, D. Montag, H. Maeser et al., "Evaluating adhesion and alignment of dental pulp stem cells to a spider silk substrate for tissue engineering applications," *Materials Science and Engineering: C*, vol. 81, pp. 104–112, 2017.
- [45] S. Salehi, K. Koeck, and T. Scheibel, "Spider Silk for Tissue Engineering Applications," *Molecules*, vol. 25, no. 3, p. 737, 2020.
- [46] C. Fredriksson, M. Hedhammar, R. Feinstein et al., "Tissue Response to Subcutaneously Implanted Recombinant Spider Silk: An in Vivo Study," *Maternité*, vol. 2, no. 4, pp. 1908–1922, 2009.
- [47] O. Emile, A. le Floch, and F. Vollrath, "Shape memory in spider draglines," *Nature*, vol. 440, no. 7084, p. 621, 2006.
- [48] H. Venkatesan, J. Chen, H. Liu et al., "Artificial spider silk is smart like natural one: having humidity-sensitive shape memory with superior recovery stress," *Materials Chemistry Frontiers*, vol. 3, no. 11, pp. 2472–2482, 2019.
- [49] K. Hennecke, J. Redeker, J. W. Kuhbier et al., "Bundles of Spider Silk, Braided into Sutures, Resist Basic Cyclic Tests: Potential Use for Flexor Tendon Repair," *PLoS One*, vol. 8, no. 4, article e61100, 2013.
- [50] S. Yi, L. Xu, and X. Gu, "Scaffolds for peripheral nerve repair and reconstruction," *Experimental Neurology*, vol. 319, article 112761, 2019.
- [51] C. Radtke, C. Allmeling, K. H. Waldmann et al., "Spider Silk Constructs Enhance Axonal Regeneration and Remyelination in Long Nerve Defects in Sheep," *PLoS One*, vol. 6, no. 2, article e16990, 2011.
- [52] F. Roloff, S. Strauss, P. M. Vogt, G. Bicker, and C. Radtke, "Spider Silk as Guiding Biomaterial for Human Model Neurons," *BioMed Research International*, vol. 2014, Article ID 906819, 7 pages, 2014.
- [53] F. Millesi, T. Weiss, A. Mann et al., "Defining the regenerative effects of native spider silk fibers on primary Schwann cells, sensory neurons, and nerve-associated fibroblasts," *The FASEB Journal*, vol. 35, no. 2, article e21196, 2021.
- [54] A. Naghilou, L. Pöttschacher, F. Millesi et al., "Correlating the secondary protein structure of natural spider silk with its guiding properties for Schwann cells," *Materials Science and Engineering: C*, vol. 116, article 111219, 2020.
- [55] T. Kornfeld, J. Nessler, C. Helmer et al., "Spider silk nerve graft promotes axonal regeneration on long distance nerve defect in a sheep model," *Biomaterials*, vol. 271, article 120692, 2021.
- [56] M. Bognitzki, W. Czado, T. Frese et al., "Nanostructured Fibers via Electrospinning," *Advanced Materials*, vol. 13, no. 1, pp. 70–72, 2001.
- [57] C. Belbéoçh, J. Lejeune, P. Vroman, and F. Salaün, "Silkworm and spider silk electrospinning: a review," *Environmental Chemistry Letters*, vol. 19, no. 2, pp. 1737–1763, 2021.
- [58] S. K. Nune, K. S. Rama, V. R. Dirisala, and M. Y. Chavali A.M.B.T.-N. for N.T. Grumezescu, *Micro Nano Technol*, D. Ficaí, Ed., Elsevier, 2017.
- [59] D. R. Whittall, K. V. Baker, R. Breitling, and E. Takano, vol. 39, no. 6, pp. 560–573, 2020.
- [60] G. Lang, S. Jokisch, and T. Scheibel, "Air Filter Devices Including Nonwoven Meshes of Electrospun Recombinant Spider Silk Proteins," *JoVE*, no. 75, 2013.
- [61] E. DeSimone, T. B. Aigner, M. Humenik, G. Lang, and T. Scheibel, "Aqueous electrospinning of recombinant spider silk proteins," *Materials Science and Engineering: C*, vol. 106, article 110145, 2020.
- [62] C. C. Berry, G. Campbell, A. Spadiccino, M. Robertson, and A. S. G. Curtis, "The influence of microscale topography on fibroblast attachment and motility," *Biomaterials*, vol. 25, no. 26, pp. 5781–5788, 2004.
- [63] L. Zhao, D. Chen, Q. Yao, and M. Li, "Studies on the use of recombinant spider silk protein/polyvinyl alcohol electrospinning membrane as wound dressing," *International Journal of Nanomedicine*, vol. 12, pp. 8103–8114, 2017.
- [64] K. Pawar, G. Welzel, C. Haynl, S. Schuster, and T. Scheibel, "Recombinant Spider Silk and Collagen-Based Nerve Guidance Conduits Support Neuronal Cell Differentiation and Functionality in Vitro," *ACS Applied Bio Materials*, vol. 2, no. 11, pp. 4872–4880, 2019.
- [65] K. Spiess, R. Ene, C. D. Keenan, J. Senker, F. Kremer, and T. Scheibel, "Impact of initial solvent on thermal stability and mechanical properties of recombinant spider silk films," *Journal of Materials Chemistry*, vol. 21, no. 35, p. 13594, 2011.
- [66] C. L. Tucker, J. A. Jones, H. N. Bringhurst et al., "Mechanical and Physical Properties of Recombinant Spider Silk Films Using Organic and Aqueous Solvents," *Biomacromolecules*, vol. 15, no. 8, pp. 3158–3170, 2014.
- [67] E. Agostini, G. Winter, and J. Engert, "Scale-up of water-based spider silk film casting using a film applicator," *International Journal of Pharmaceutics*, vol. 532, no. 1, pp. 13–20, 2017.
- [68] K. Spieß, S. Wohlrab, and T. Scheibel, "Structural characterization and functionalization of engineered spider silk films," *Soft Matter*, vol. 6, no. 17, p. 4168, 2010.
- [69] F. Bauer, S. Wohlrab, and T. Scheibel, "Controllable cell adhesion, growth and orientation on layered silk protein films," *Biomaterials Science*, vol. 1, no. 12, pp. 1244–1249, 2013.
- [70] S. Kumari, G. Lang, E. DeSimone et al., "Engineered spider silk-based 2D and 3D materials prevent microbial infestation," *Materials Today*, vol. 41, pp. 21–33, 2020.
- [71] S. L. Young, M. Gupta, C. Hanske, A. Fery, T. Scheibel, and V. V. Tsukruk, "Utilizing Conformational Changes for Patterning Thin Films of Recombinant Spider Silk Proteins," *Biomacromolecules*, vol. 13, no. 10, pp. 3189–3199, 2012.
- [72] A. Molina, T. Scheibel, and M. Humenik, "Nanoscale Patterning of Surfaces via DNA Directed Spider Silk Assembly," *Biomacromolecules*, vol. 20, no. 1, pp. 347–352, 2019.

- [73] E. Bini, C. W. P. Foo, J. Huang, V. Karageorgiou, B. Kitchel, and D. L. Kaplan, "RGD-Functionalized Bioengineered Spider Dragline Silk Biomaterial," *Biomacromolecules*, vol. 7, no. 11, pp. 3139–3145, 2006.
- [74] S. Wohlrab, S. Müller, A. Schmidt et al., "Cell adhesion and proliferation on RGD-modified recombinant spider silk proteins," *Biomaterials*, vol. 33, no. 28, pp. 6650–6659, 2012.
- [75] U. Johansson, M. S. García-Gutiérrez, M. Moscoso-Castro, J. Manzanares, and O. Valverde, "Reduced Contextual Discrimination following Alcohol Consumption or MDMA Administration in Mice," *PLoS One*, vol. 10, no. 11, p. 1, 2015.
- [76] J. Chen, H. Venkatesan, and J. Hu, "Chemically Modified Silk Proteins," *Advanced Engineering Materials*, vol. 20, no. 7, p. 1700961, 2018.
- [77] J. G. Hardy, A. Pfaff, A. Leal-Egaña, A. H. E. Müller, and T. R. Scheibel, "Glycopolymer Functionalization of Engineered Spider Silk Protein-based Materials for Improved Cell Adhesion," *Macromolecular Bioscience*, vol. 14, no. 7, pp. 936–942, 2014.
- [78] W. A. Laftah, S. Hashim, and A. N. Ibrahim, "Polymer Hydrogels: A Review," *Polymer-Plastics Technology and Engineering*, vol. 50, no. 14, pp. 1475–1486, 2011.
- [79] B. H. Cipriano, S. J. Banik, R. Sharma et al., "Superabsorbent Hydrogels That Are Robust and Highly Stretchable," *Macromolecules*, vol. 47, no. 13, pp. 4445–4452, 2014.
- [80] Z. Li and Z. Lin, "Recent advances in polysaccharide-based hydrogels for synthesis and applications," *Aggregate*, vol. 2, no. 2, p. 1, 2021.
- [81] U. K. Slotta, S. Rammensee, S. Gorb, and T. Scheibel, "An Engineered Spider Silk Protein Forms Microspheres," *Angewandte Chemie*, vol. 47, no. 24, pp. 4592–4594, 2008.
- [82] Z. H. Ayub, M. Arai, and K. Hirabayashi, "Quantitative structural analysis and physical properties of silk fibroin hydrogels," *Polymer (Guildf)*, vol. 35, no. 10, pp. 2197–2200, 1994.
- [83] G.-D. Kang, J. H. Nahm, J. S. Park, J. Y. Moon, C. S. Cho, and J. H. Yeo, "Effects of poloxamer on the gelation of silk fibroin," *Macromolecular Rapid Communications*, vol. 21, no. 11, pp. 788–791, 2000.
- [84] U. J. Kim, J. Park, C. Li, H. J. Jin, R. Valluzzi, and D. L. Kaplan, "Structure and Properties of Silk Hydrogels," *Biomacromolecules*, vol. 5, no. 3, pp. 786–792, 2004.
- [85] K. Schacht and T. Scheibel, "Controlled Hydrogel Formation of a Recombinant Spider Silk Protein," *Biomacromolecules*, vol. 12, no. 7, pp. 2488–2495, 2011.
- [86] S. Rammensee, D. Huemmerich, K. D. Hermanson, T. Scheibel, and A. R. Bausch, "Rheological characterization of hydrogels formed by recombinantly produced spider silk," *Applied Physics A: Materials Science & Processing*, vol. 82, no. 2, pp. 261–264, 2006.
- [87] V. J. Neubauer, V. T. Trossmann, S. Jacobi, A. Döbl, and T. Scheibel, "Recombinant Spider Silk Gels Derived from Aqueous–Organic Solvents as Depots for Drugs," *Angewandte Chemie*, vol. 60, no. 21, pp. 11847–11851, 2021.
- [88] M. C. Arno, M. Inam, A. C. Weems et al., "Exploiting the role of nanoparticle shape in enhancing hydrogel adhesive and mechanical properties," *Nature Communications*, vol. 11, no. 1, p. 1420, 2020.
- [89] Y. Dou, Y. M. Yang, J. You et al., "Author Correction: Solution-processed hybrid perovskite photodetectors with high detectivity," *Nature Communications*, vol. 10, no. 1, p. 1, 2019.
- [90] R. G. Wells, "The role of matrix stiffness in regulating cell behavior," *Hepatology*, vol. 47, no. 4, pp. 1394–1400, 2008.
- [91] A. J. Engler, S. Sen, H. L. Sweeney, and D. E. Discher, "Matrix Elasticity Directs Stem Cell Lineage Specification," *Cell*, vol. 126, no. 4, pp. 677–689, 2006.
- [92] L. D. Koh, Y. Cheng, C. P. Teng et al., "Structures, mechanical properties and applications of silk fibroin materials," *Progress in Polymer Science*, vol. 46, pp. 86–110, 2015.
- [93] X. Zhang, C. B. Baughman, and D. L. Kaplan, "In vitro evaluation of electrospun silk fibroin scaffolds for vascular cell growth," *Biomaterials*, vol. 29, no. 14, pp. 2217–2227, 2008.
- [94] Q. Lu, X. Zhang, X. Hu, and D. L. Kaplan, "Green Process to Prepare Silk Fibroin/Gelatin Biomaterial Scaffolds," *Macromolecular Bioscience*, vol. 10, no. 3, pp. 289–298, 2010.
- [95] D. Yao, S. Dong, Q. Lu et al., "Salt-Leached Silk Scaffolds with Tunable Mechanical Properties," *Biomacromolecules*, vol. 13, no. 11, pp. 3723–3729, 2012.
- [96] I. I. Agapov, O. L. Pustovalova, M. M. Moisenovich et al., "Three-dimensional scaffold made from recombinant spider silk protein for tissue engineering," *Doklady. Biochemistry and Biophysics*, vol. 426, no. 1, pp. 127–130, 2009.
- [97] M. M. Moisenovich, O. L. Pustovalova, A. Yu Arhipova et al., "In vitro and in vivo biocompatibility studies of a recombinant analogue of spidroin 1 scaffolds," *Journal of Biomedical Materials Research Part A*, vol. 96A, no. 1, pp. 125–131, 2011.
- [98] M. M. Moisenovich, O. Pustovalova, J. Shackelford et al., "Tissue regeneration in vivo within recombinant spidroin 1 scaffolds," *Biomaterials*, vol. 33, no. 15, pp. 3887–3898, 2012.
- [99] H. Shin, S. Jo, and A. G. Mikos, "Biomimetic materials for tissue engineering," *Biomaterials*, vol. 24, no. 24, pp. 4353–4364, 2003.
- [100] J. Hubbell, "Bioactive biomaterials," *Current Opinion in Biotechnology*, vol. 10, no. 2, pp. 123–129, 1999.
- [101] K. Schacht, J. Vogt, and T. Scheibel, "Foams Made of Engineered Recombinant Spider Silk Proteins as 3D Scaffolds for Cell Growth," *ACS Biomaterials Science & Engineering*, vol. 2, no. 4, pp. 517–525, 2016.
- [102] E. A. Calle, M. Ghaedi, S. Sundaram, A. Sivarapatna, M. K. Tseng, and L. E. Niklason, "Strategies for Whole Lung Tissue Engineering," *IEEE Transactions on Biomedical Engineering*, vol. 61, no. 5, pp. 1482–1496, 2014.
- [103] L. Gustafsson, C. P. Tasiopoulos, R. Jansson et al., "Recombinant Spider Silk Forms Tough and Elastic Nanomembranes that are Protein-Permeable and Support Cell Attachment and Growth," *Advanced Functional Materials*, vol. 30, no. 40, p. 2002982, 2020.
- [104] C. P. Tasiopoulos, L. Gustafsson, W. van der Wijngaart, and M. Hedhammar, "Fibrillar Nanomembranes of Recombinant Spider Silk Protein Support Cell Co-culture in an In Vitro Blood Vessel Wall Model," *ACS Biomater Sci Eng*, vol. 7, no. 7, pp. 3332–3339, 2021.
- [105] M. Landreh, A. Rising, J. Presto, H. Jörnvall, and J. Johansson, "Specific Chaperones and Regulatory Domains in Control of Amyloid Formation," *The Journal of Biological Chemistry*, vol. 290, no. 44, pp. 26430–26436, 2015.
- [106] N. Kronqvist, M. Sarr, A. Lindqvist et al., "Efficient protein production inspired by how spiders make silk," *Nature Communications*, vol. 8, no. 1, 2017.
- [107] I. Agnarsson, M. Kuntner, and T. A. Blackledge, "Bioprospecting Finds the Toughest Biological Material: Extraordinary Silk

- from a Giant Riverine Orb Spider,” *PLoS One*, vol. 5, no. 9, p. 1, 2010.
- [108] C. Vepari and D. L. Kaplan, “Silk as a biomaterial,” *Progress in Polymer Science*, vol. 32, no. 8-9, pp. 991–1007, 2007.
- [109] U. Johansson, H. Vallhov, T. Holm et al., “Author Correction: Extracellular nanovesicles released from the commensal yeast *Malassezia sympodialis* are enriched in allergens and interact with cells in human skin,” *Scientific Reports*, vol. 9, no. 1, p. 1, 2019.
- [110] T. Scheibel, “Spider silks: recombinant synthesis, assembly, spinning, and engineering of synthetic proteins,” *Microbial Cell Factories*, vol. 3, no. 1, p. 14, 2004.
- [111] N. Dinjaski, R. Plowright, S. Zhou, D. J. Belton, C. C. Perry, and D. L. Kaplan, “Osteoinductive recombinant silk fusion proteins for bone regeneration,” *Acta Biomaterialia*, vol. 49, pp. 127–139, 2017.
- [112] J. G. Hardy, J. Torres-Rendon, A. Leal-Egaña et al., “Biomimetalization of Engineered Spider Silk Protein-Based Composite Materials for Bone Tissue Engineering,” *Materials (Basel)*, vol. 9, no. 7, p. 560, 2016.
- [113] J. G. Hardy, A. Bertin, J. G. Torres-Rendon et al., “Facile Photochemical Modification of Silk Protein-Based Biomaterials,” *Macromolecular Bioscience*, vol. 18, no. 11, p. 1800216, 2018.
- [114] M. Lewicka, O. Hermanson, and A. U. Rising, “Recombinant spider silk matrices for neural stem cell cultures,” *Biomaterials*, vol. 33, no. 31, pp. 7712–7717, 2012.
- [115] M. Lewicka, P. Rebellato, J. Lewicki, P. Uhlén, A. Rising, and O. Hermanson, “Recombinant Spider Silk Protein Matrices Facilitate Differentiation of Neural Stem Cells Into Mature and Functional Neurons,” *Front. Mater.*, vol. 7, 2021.
- [116] C. Åstrand, V. Chotteau, A. Falk, and M. Hedhammar, “Assembly of FN-silk with laminin-521 to integrate hPSCs into a three-dimensional culture for neural differentiation,” *Biomaterials Science*, vol. 8, no. 9, pp. 2514–2525, 2020.
- [117] H. Wendt, A. Hillmer, K. Reimers et al., “Artificial Skin – Culturing of Different Skin Cell Lines for Generating an Artificial Skin Substitute on Cross-Weaved Spider Silk Fibres,” *PLoS One*, vol. 6, no. 7, p. e21833, 2011.
- [118] C. Guo, C. Li, X. Mu, and D. L. Kaplan, “Engineering silk materials: From natural spinning to artificial processing,” *Applied Physics Reviews*, vol. 7, no. 1, p. 011313, 2020.
- [119] C. Guo, C. Li, H. V. Vu et al., “Thermoplastic moulding of regenerated silk,” *Nature Materials*, vol. 19, no. 1, pp. 102–108, 2020.
- [120] ““Munich firm develops synthetic spider silk,” can be found under,” 2011, <https://www.thelocal.de/20110913/37547/>.
- [121] ““Comparing spider silk production technologies,” can be found under,” 2018, https://www.kraiglabs.com/comparison/#_ftnref4.
- [122] S. Müller-Herrmann and T. Scheibel, “Enzymatic Degradation of Films, Particles, and Nonwoven Meshes Made of a Recombinant Spider Silk Protein,” *The Sciences and Engineering*, vol. 1, no. 4, pp. 247–259, 2015.
- [123] L. Gu, Y. Jiang, and J. Hu, “Scalable Spider-Silk-Like Super-tough Fibers using a Pseudoprotein Polymer,” *Advanced Materials*, vol. 31, no. 48, p. 1904311, 2019.
- [124] K. Tsuchiya and K. Numata, “Chemical Synthesis of Multi-block Copolypeptides Inspired by Spider Dragline Silk Proteins,” *ACS Macro Letters*, vol. 6, no. 2, pp. 103–106, 2017.

Research Article

Stable Long-Term Culture of Human Distal Airway Stem Cells for Transplantation

Yueqing Zhou,¹ Yujia Wang,^{1,2} Dandan Li,¹ Ting Zhang,² Yu Ma,² and Wei Zuo ^{1,2,3,4}

¹East Hospital, Tongji University School of Medicine, Shanghai 200120, China

²Regend Therapeutics, Shanghai 200127, China

³Ningxia Medical University, Yinchuan 750004, China

⁴The First Affiliated Hospital, Guangzhou Medical University, Guangzhou 510120, China

Correspondence should be addressed to Wei Zuo; zuow@tongji.edu.cn

Received 4 March 2021; Revised 21 June 2021; Accepted 23 August 2021; Published 17 September 2021

Academic Editor: Dunfang Zhang

Copyright © 2021 Yueqing Zhou et al. This is an open access article distributed under the Creative Commons Attribution License, which permits unrestricted use, distribution, and reproduction in any medium, provided the original work is properly cited.

There is a population of p63⁺/Krt5⁺ distal airway stem cells (DASCs) quiescently located in the airway basal epithelium of mammals, responding to injury and airway epithelial regeneration. They hold the ability to differentiate into multiple pulmonary cell types and can repopulate the epithelium after damage. The current study aims at gaining further insights into the behavior and characteristics of the DASCs isolated from the patient lung and exploring their clinical translational potential. Human DASCs were brushed off through the bronchoscopic procedure and expanded under the pharmaceutical-grade condition. Their phenotype stability in long-term cell culture was analyzed, followed by safety evaluation and tumorigenic analysis using multiple animal models including rodents and nonhuman primate. The chimerism of the human-mouse lung model indicated that DASC pedigrees could give rise to multiple epithelial types, including type I alveolar cells as well as bronchiolar secretory cells, to regenerate the distal lung. Taken together, the results suggested that DASC transplantation could be a promising therapeutic approach for unmet needs in respiratory medicine including the COVID-19-related diseases.

1. Introduction

The lung is a complex organ that takes responsibility for gas exchange, including filtering and delivering inhaled and exhaled air [1]. Lung diseases constitute a serious threat to human public health worldwide, with high morbidity and mortality [2–6]. Despite that mitigating therapies contribute to control deterioration, it remains limited to repair and recover the pulmonary function of lung disease particularly such as bronchiectasis, idiopathic pulmonary fibrosis (IPF) [7], and chronic obstructive pulmonary disease (COPD) [8, 9], which involves the progressive and inexorable destruction of oxygen exchange surfaces and airways.

Multiple stem/progenitor populations [10–15] in the lung with the capability to reconstruct lung epithelium have been identified in the last decade, which can be regarded as a potential candidate for therapeutic strategies targeted to damages of airway and alveolar tissues. Previously, we showed that a rare population of distal airway stem cells

(DASCs) identified coexpressing p63⁺/Krt5⁺, quiescently located at the airway basal epithelium of mammals, responding to injury and airway epithelial regeneration [16–21]. They hold the ability to differentiate into multiple pulmonary cell types and repopulate the epithelium after damage. DASCs undergo a proliferative expansion and migration in response to influenza-induced or bleomycin-induced lung damage and assemble into nascent alveoli at sites of interstitial lung inflammation [17, 20, 21]. Human DASCs can be cloned *in vitro* and xenotransplanted into the murine lung, giving rise to “human-mouse chimeric lung” [16].

In the current study, to gain further insights into the behavior and character of the DASCs isolated from the patient lung, we first analyzed their stability in cell culture under the pharmaceutical-grade condition as a cell therapeutic candidate, followed with valuation of their safety and efficacy using multiple animal models, including a rodent model and nonhuman primate model. Taken together, we provide an all-around evaluation of human DASCs for

further clinical trials utilizing autologous lung stem/progenitor cells as a therapeutic intervention in multiple respiratory diseases.

2. Method

2.1. Animals. Cynomolgus macaque (*M. fascicularis*), aged 60 months and originating from Guangdong Qianyan Biological Science and Technology Co. Ltd., was used in this study. Macaque was housed in JOINN Laboratories infrastructure facilities (Suzhou) in compliance with Animal Welfare Act and Regulations (Public Law 99-198) promulgated by USDA. The protocols were approved by the institutional ethical committee under statement number ACU18-959. NOD-SCID mice (6–8 weeks old) purchased from Shanghai SLAC Laboratory Animal Co. Ltd. (China), maintained in SPF animal facilities, were used for human DASC transplantation.

2.2. Isolation and Culture of Human Distal Airway Stem Cells. Patients diagnosed with or without chronic lung diseases (COPD, bronchiectasis, and ILD), through the ATS/ERS guideline, were recruited. All individuals went through thorough medical examination before sampling. Human distal airway stem cells located were brushed off through bronchoscopic procedure performed by board-certified respiratory physicians using a flexible fiberoptic bronchoscope (Olympus, Japan) [16]. Briefly, after oropharyngeal and laryngeal anesthesia, the bronchoscope was advanced through the vocal cords with 2 mL 2% lidocaine solution instilled into the trachea and both main bronchi. A disposable 2 mm brush was advanced through the working channel of the bronchoscope and used to collect lung epithelial samples by gently brushing back and forth 1–2 times in the 4~6th-order bronchi. Samples were digested, passed through a 70 μ m cell strainer, and washed with cold DMEM medium supplemented with clinically approved antibiotics. The cell suspension was plated onto irradiated 3T3 fibroblast feeder cells from ATCC CCL-92 and cultured in pharmaceutical-grade culture medium, including DMEM/F12, 10% FBS (HyClone, Australia), Pen/Strep, amphotericin, and growth factor cocktail as previously described [16] with 7.5% CO₂ for DASC-selective growth and expansion. DASCs were grown in primary cultures with antibiotics and continuously propagated in the following feeder-free cultures in the absence of antibiotics. Then, cells were harvested, washed, and suspended in clinically approved 0.9% w/v of NaCl. The harvested cells were directly used for preclinical experiments.

2.3. In Vitro Monolayer Differentiation. The monolayer differentiation system *in vitro* was described previously [20]. Cells from two donors were first cultured in culture medium for 1 day and then transferred to serum-free DMEM/F12 medium supplemented with FGF10 (50 ng/mL, PeproTech, USA), transferrin (5 μ g/mL, PeproTech, USA), HGF (20 ng/mL, PeproTech, USA), and 5% BSA for 5 days to induce distal lung differentiation [22].

2.4. Immunofluorescence. Fresh tissue was fixed in 4% paraformaldehyde (PFA) overnight at 4°C and then settled by 30% sucrose before embedding into the Tissue-Tek O.C.T. compound (Sakura, Japan). All the samples were sliced into 5–7 μ m thickness using a microtome (Leica Microsystems, Germany).

Immunofluorescence staining was conducted by the standard protocol described previously [16]. Cells attached on a plate or tissue sections were fixed by 3.7% formaldehyde and then incubated with 0.2% Triton X-100 to improve the cell permeability for 10 min. Tissue slices were subjected to antigen retrieval in citrate buffer (pH 6.0, Sigma, USA) in the microwave oven for 20 min before staining. Primary antibodies were incubated overnight at 4°C, following 10% donkey serum blocking for 2 h at RT. Antibodies used in the current study were anti-KRT5 (1:200, EP1601Y, Thermo Fisher Scientific, USA), anti-P63 (1:500, 4A4, Abcam, USA), anti-Ki67 (1:500, B126.1, Abcam, USA), anti-SCGB1A1 (1:200, T-18, Santa Cruz Biotechnology, USA), anti-human specific Lamin A+C (1:200, ab108595, Abcam, USA), anti-AQP5 (1:500, EPR3747, Abcam, USA), anti-HOPX (1:200, ab230544, Abcam, USA), anti-PDPN (1:200, 18H5, Santa Cruz Biotechnology, USA), anti-GFP (1:200, ab290, Abcam, USA), and anti-GFP (1:500, ab6673, Abcam, USA). Alexa Fluor-conjugated 488/594 (1:500, Life Technologies, USA) antibodies were used as secondary antibodies.

2.5. Tumorigenic Assay. For anchorage-independent growth assay, 0.75×10^4 cells from 2 donors were seeded in 1 mL of a 0.375% upper agar (Sigma) layer on a 0.5% under agar layer in the DMEM supplemented with 10% FBS. Cultures were usually maintained for 14 days, and then, gels were stained by crystal violet-methanol solution (SolarBio) [19, 23].

A total of 15 male NOD-SCID mice (6–8 weeks old) were used for *in vivo* tumorigenic assay. Mice were equally divided into 3 groups and received a subcutaneous injection of either 10^7 DASCs from 2 donors, 10^7 human embryonic lung fibroblast cell line MRC-5, or 10^6 HeLa cells. Tumor sizes were measured with a caliper at the injection site on indicated time points. The tumor volume was calculated using the formula $\text{volume} = 0.5 \times \text{length (mm)} \times (\text{width [mm]})^2$. Mice that had tumors with the longest diameter of 20 mm or with a sign of physiological decondition were euthanized, necropsied, and subjected for gross observation and histopathological examination. The last measurement was carried forward for the mice euthanized on day 112.

2.6. DASC Transplantation Experiment. NOD-SCID mice (6–8 weeks old) purchased from Shanghai SLAC Laboratory Animal Co. Ltd. (China), maintained in SPF animal facilities, were used for human DASC transplantation. The mouse lung was injured by intratracheally instilling with bleomycin (3 U/kg body weight, SelleckChem, USA) 8 days before cell transplantation. Then, mice were anesthetized by intraperitoneal injection of 1.25% avertin and rested on a stand gesture. One million DASCs suspended in 50 μ L of PBS were intratracheally instilled into the injured lung. On indicated day posttransplantation, mice were euthanized and the

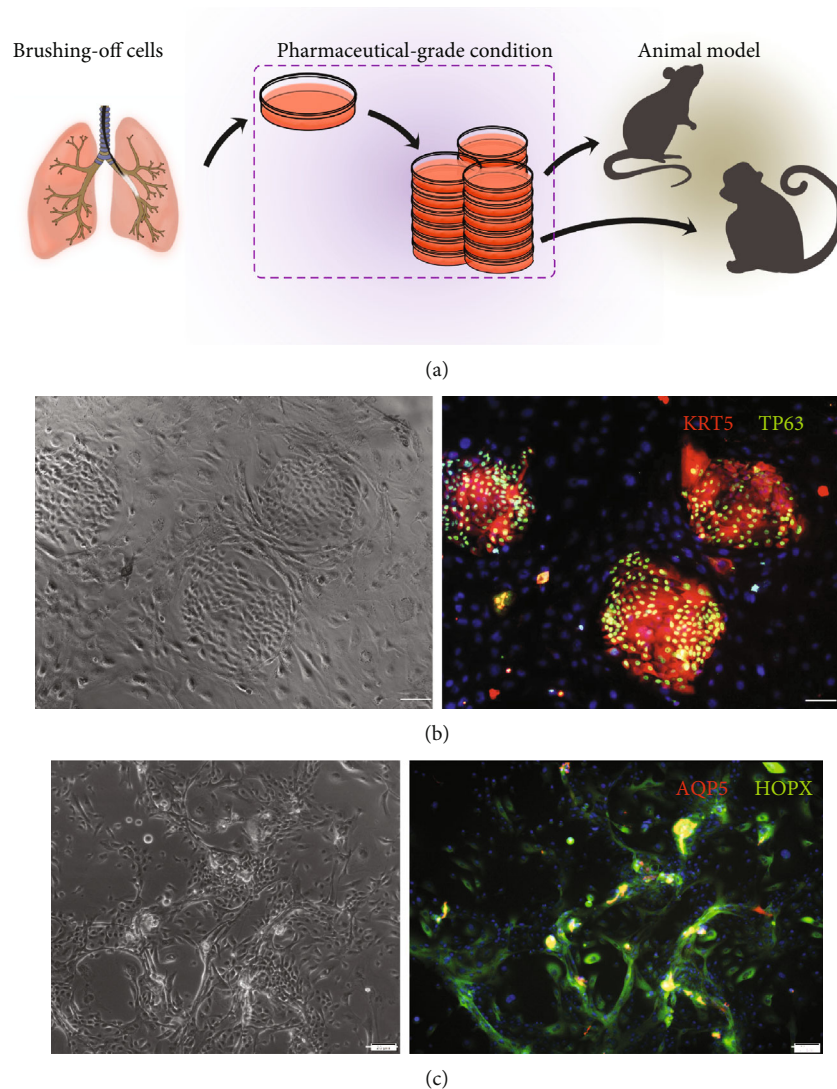


FIGURE 1: Bronchoscopic isolation of hDASCs from the patient lung. (a) Schematic illustrating the process of clonogenic hDASC isolation and expansion. (b) Clonogenic cells immunostained with hDASC markers KRT5 and P63. (b1) Bright-field imaging. (b2) Immunofluorescence imaging. Scale bar, $100\ \mu\text{m}$. (c) Differentiation culture of hDASCs in the monolayer on day 7. (c1) Bright-field imaging. (c2) Immunofluorescence imaging. Scale bar, $50\ \mu\text{m}$.

lung samples were harvested for immunofluorescence analysis. Bright-field and direct fluorescence images of the transplanted lung were acquired under the fluorescence stereomicroscope (MVX10, Olympus, Japan).

In Vivo Safety Assay of hDASCs

To test the potential acute toxicity of cells *in vivo*, a pre-clinical short-term safety assay was conducted by single intratracheal administration of hDASCs from 2 donors, containing at least 35-fold higher than the intentional clinical dose in male mice (8–9 weeks old). In detail, 20 mice were equally divided into the three hDASC groups, which received cell transplantation at a dose level of 6×10^6 cells/kg (low dose), 3×10^7 cells/kg (medium dose), and 1.5×10^8 cells/kg (high dose), and a control group received normal saline. The morbidity, mortality, abnormal behavior, and toxic reactions, if any, were observed for 14 days after the transplantation. After the 14-day observation period, all

mice were euthanized, necropsied, and subjected for gross observation and histopathological examination.

For the preclinical long-term safety assay, a total of 80 male mice were equally divided into two groups: a cell treatment group that received hDASCs from 3 donors or a control group that received normal saline. Mice in the cell treatment group received two deliveries of hDASCs at a dose level of 6×10^7 cells/kg/delivery on day 0 and day 28. Changes in fur, skin, limbs, mouth, nose, and eyes; abnormal behavior in physical, physiological, or neurological activities; and changes in reactivity to handling or sensory stimuli, if any, were recorded daily. Bodyweight and food/water intake were recorded weekly. Twenty mice from each group were necropsied and subjected to multiple examinations by the end of the administration period (day 30), and the left mice were necropsied and subjected for examination by the end of the observation period (day

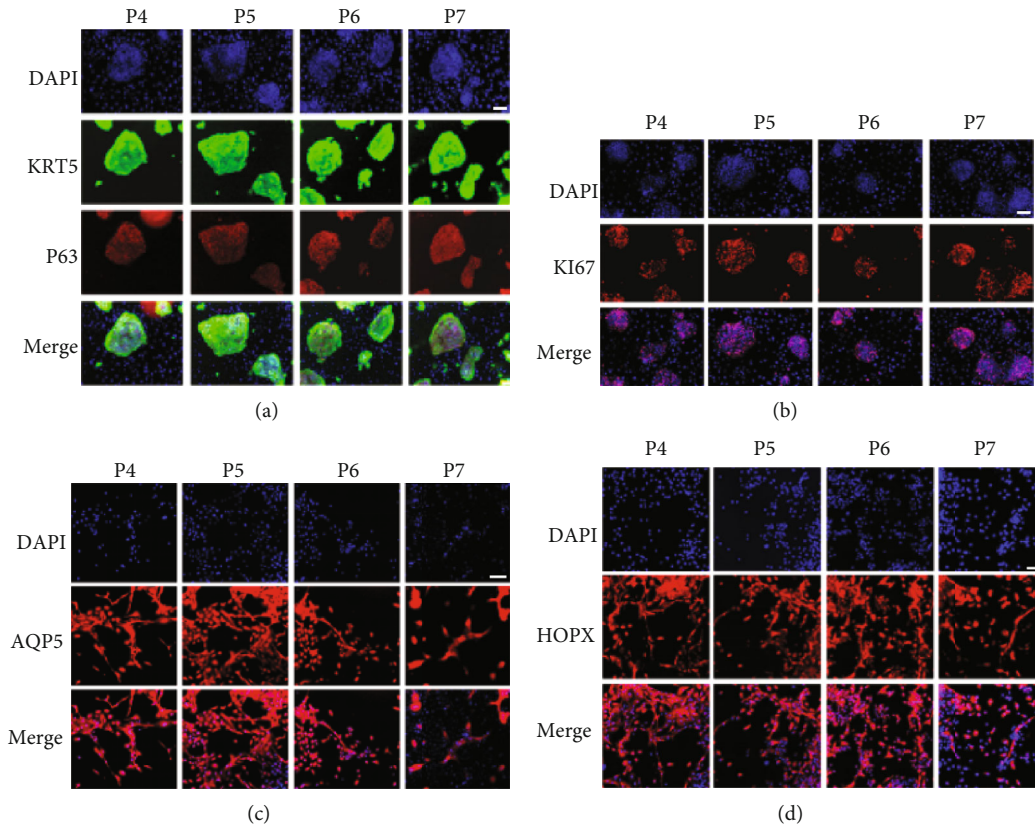


FIGURE 2: Expansion of hDASCs under the pharmaceutical-grade condition. (a) Clonogenic cells immunostained with hDASC markers KRT5 and P63 among P4 to P7. Scale bar, $100\ \mu\text{m}$. (b) Clonogenic cells immunostained with proliferative markers KI67 among P4 to P7. Scale bar, $100\ \mu\text{m}$. (c, d) Immunostaining of indicated AEC1 markers AQP5 and HOPX on monolayer-differentiated DASCs. Scale bar, $100\ \mu\text{m}$.

57). A whole set of the examination includes hematologic profiling, lymphocyte subset counting, blood coagulation test, serum biochemistry analysis, and quantification of serum immunoglobulin, complement, and inflammatory cytokines. The gross necropsy and histopathological examination of organs, which included the brain, heart, lungs, trachea, kidneys, liver, spleen, testis, and bone marrow, were carried out.

2.7. Nonhuman Primate Model for Transplantation. One macaque was pretreated by the electron linear accelerator radiation ($3.12\ \text{Gy}$ and $1.55\ \text{Gy/min}$) [24] 7 days prior to cell transplantation, using ketamine ($10\ \text{mg/mL}$) and pentobarbital sodium ($15\ \text{mg/mL}$) as anesthesia. Cell suspension ($10^7\ \text{cells/mL}$ and $5\ \text{mL/kg}$) was infused into lobes through bronchoscopy performed by respiratory physicians. Seven days posttransplantation, Macaque was euthanized and all organ samples were harvested for immunofluorescence analysis. During the experiment, food intake and general clinical observation were daily monitored and detailed clinical observation, such as limbs, breathing, and skin, was weekly examined. Bright-field and direct fluorescence images of the transplanted lung were acquired under the fluorescence stereomicroscope (MVX10, Olympus, Japan).

2.8. Statistics. Continuous data are presented as mean \pm standard deviation and categorical data as an absolute number and percentage of patients in each category. Preclinical data were first assessed by Levene's test for normality. Comparison between groups was assessed through unpaired t -test or Mann-Whitney U -test according to normality. Changes in tumor volume in the tumorigenic assay were analyzed by repeated measurement ANOVA, with a p value showing the significance of between-subjects effects.

3. Results

3.1. Bronchoscopic Isolation and Stable Expansion of hDASC from Patient Lung. The distal airway stem/progenitor cells (DASCs), expressing $\text{Krt5}^+/\text{P63}^+$, have been shown to have a potent regenerative capacity [16, 20, 25]. Here, we isolated human $\text{P63}^+/\text{KRT5}^+$ DASCs (hDASCs) from the 6th-order airway of lung disease patients by bronchoscopic brushing and then expanded in a culture system as previously described [16] (Figure 1(a)). Briefly, the brush-off sample was dissociated and digested into single-cell suspension that is successfully cloned and propagated under the irradiated 3T3 feeder system with the expression of KRT5^+ and P63^+ (Figure 1(b)).

Furthermore, to explore the differentiation potency of hDASCs *in vitro*, they were transferred into a feeder-free

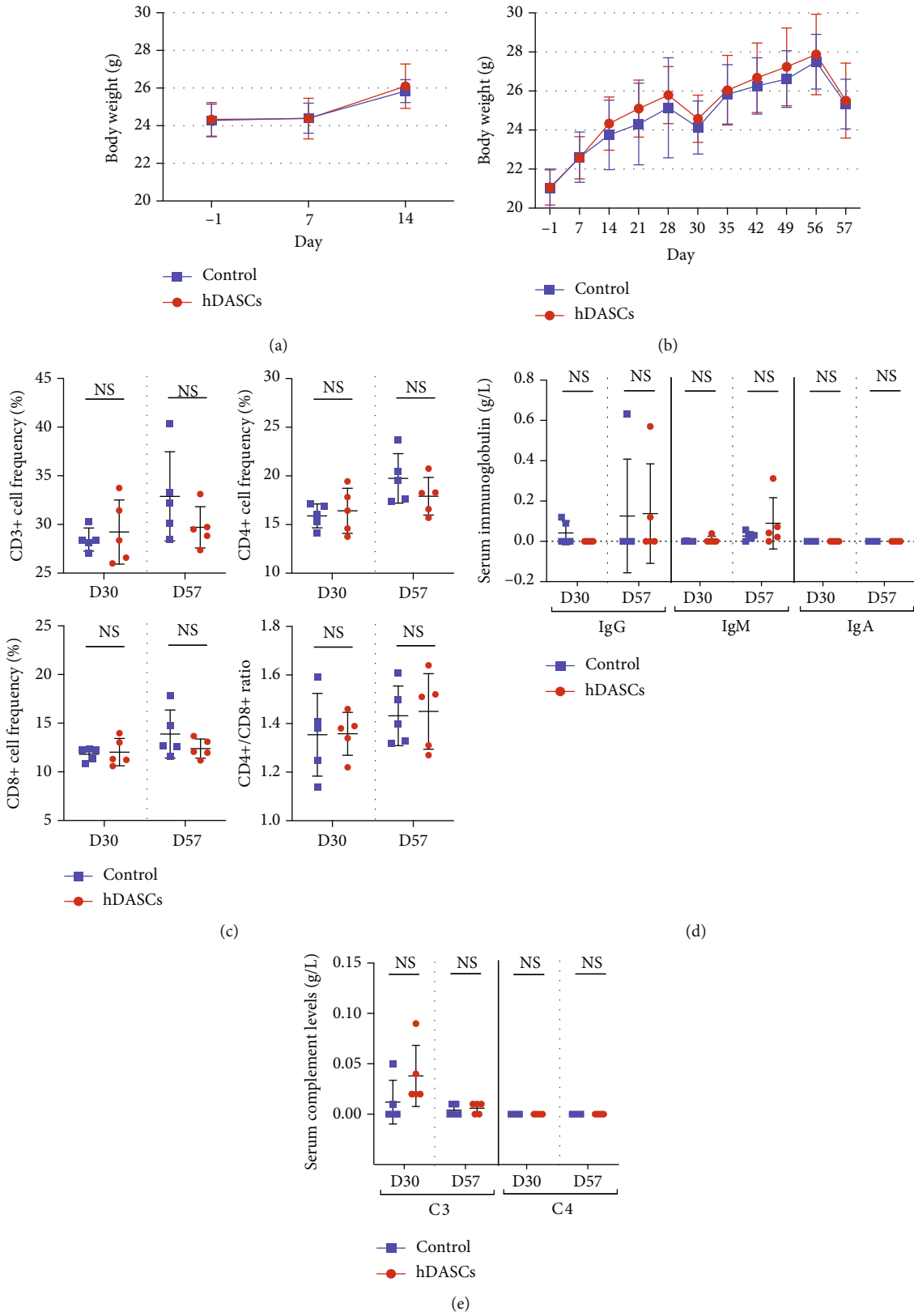


FIGURE 3: Safety evaluation of hDASC transplantation in mice. (a) Changes in mouse body weight at indicated days in short-term safety assay. $n = 10$ in each group. (b) Changes in body weight at indicated days in long-term safety assay. $n = 20$ in each group. (c) Quantification of lymphocyte subsets (CD3+, CD4+, and CD8+) and CD4+/CD8+ ratio on day 30 and day 57 in long-term safety assay. $n = 5$ in each group. (d, e) Quantification of serum immunoglobulin and serum complement levels on day 30 and day 57 in long-term safety assay. For each test, $n = 5$ in each group.

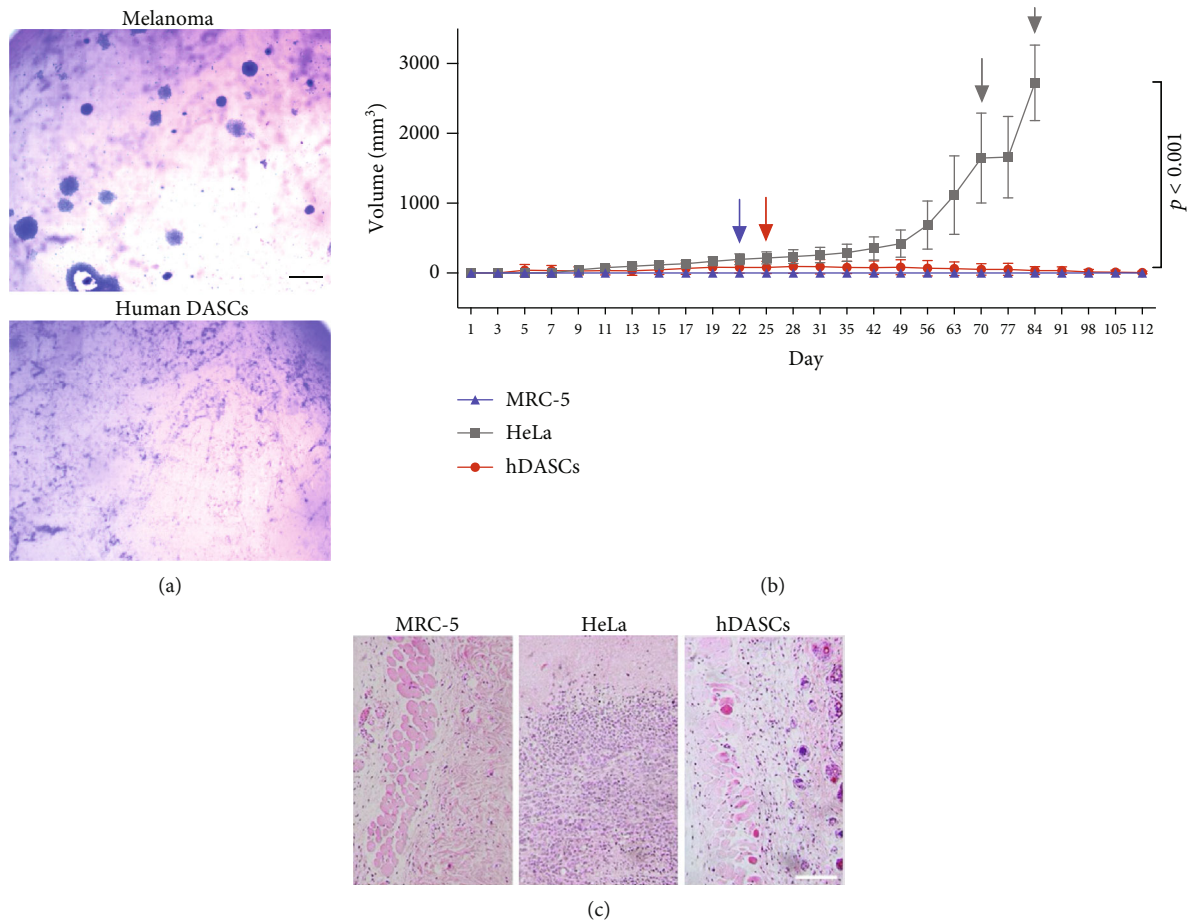
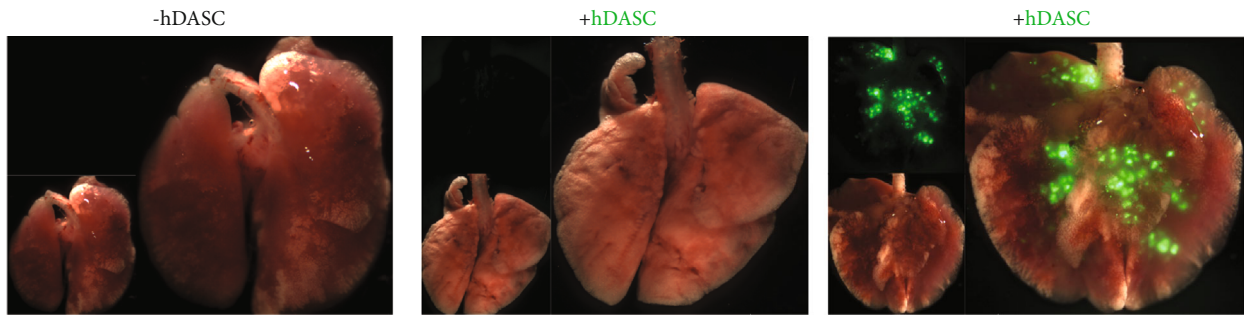


FIGURE 4: Evaluation of the tumorigenic potential of hDASCs. (a) Soft agar assay of melanoma and hDASCs. Scale bar, $200\ \mu\text{m}$. (b) Growth curves of subcutaneous tumors in NOD-SCID mice formed by inoculation with either 10^7 human embryonic lung fibroblast cell MRC-5, 10^6 HeLa cells, or 10^7 hDASCs. The blue arrow indicates that 2 mice of the MRC-5 group were euthanized for gross observation and histopathological examination. The red arrow indicates that 2 mice of the hDASC group were euthanized for gross observation and histopathological examination. Grey arrows indicate that 4 mice and 6 mice of the HeLa group were euthanized on day 70 and day 84, respectively, because the longest tumor diameter exceeded 20 mm. $n = 5$ in each group. (c) Representative H&E staining of different subcutaneous grafts. Scale bar, $100\ \mu\text{m}$.

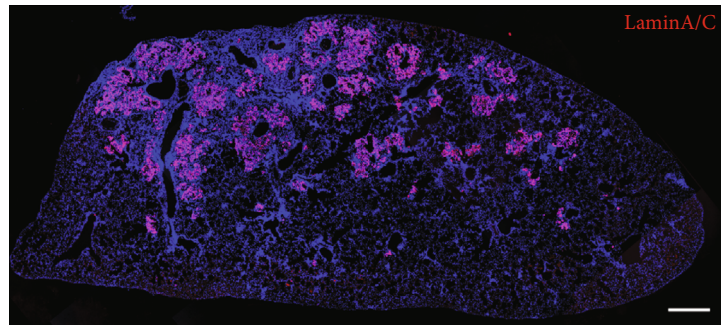
monolayer differentiation system and gave rise to a few alveolus-like structures lined by thin, highly elongated cells exhibiting AQP5 and HOPX expression, consistent with their type I alveolar epithelial cell (AEC1) identity (Figure 1(c)). To evaluate their clinical potential, isolation, expansion, and quality control of hDASCs were performed under the pharmaceutical-grade condition with all the related components in the culture medium replaced with GMP-grade ones. We have serially monitored the expression of KRT5 and KI67 from passage 4 (P4) to passage 7 (P7) *in vitro*. Among diverse passages, the gross morphology of hDASCs appeared similar and the capacity to express critical identity markers was generally maintained (Figures 2(a) and 2(b)). Consistent with this, amplified human DASCs preserved differentiation potency among serial passage (Figures 2(c) and 2(d)). The above data indicated that the current pharmaceutical-grade DASC expansion system is able to produce an autologous cell population from the lungs under pathophysiological conditions, which maintains robust differentiation capacity.

3.2. Safety Evaluation of hDASC Transplantation in Mice. Our contracted third-party collaborators performed short-term and long-term safety preclinical studies of DASCs according to Good Laboratory Practice (GLP) regulations. A 14-day short-term safety assay showed no mortality or morbidity in NOD-SCID mice after single intratracheal administration of human DASCs at various dose levels ($6 \times 10^6 - 5 \times 10^8$ cells/kg). There were no obvious abnormalities in the physical, physiological, or neurological activities of mice. Bodyweight and food/water intake demonstrated weekly fluctuations within the range of control animals (Figure 3(a)).

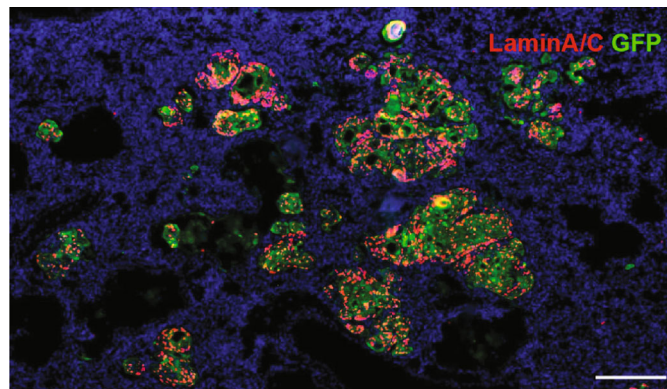
For the long-term safety study, during the entire 57-day observation period, no mortality was seen in the cell treatment group. Daily recording in physical, physiological, or neurological characteristics demonstrated no appreciable changes in treated animals. Bodyweight demonstrated no significant differences compared to control animals (Figure 3(b)). Quantification of lymphocyte subpopulation, serum immunoglobulins, and complement demonstrated



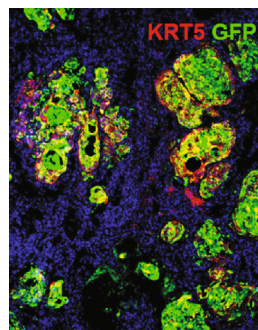
(a)



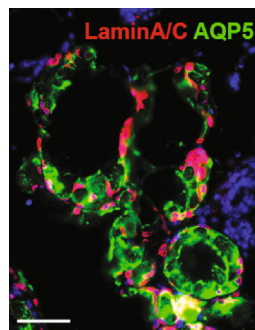
(b)



(c)



(d)



(e)

FIGURE 5: Continued.

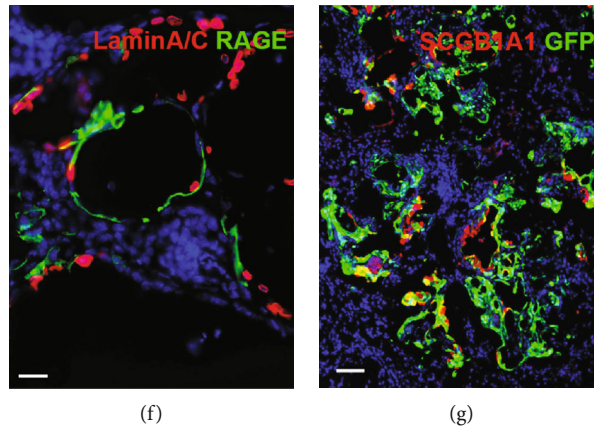


FIGURE 5: Alveolar regeneration by intrapulmonary transplantation of hDASCs. (a) Bright field and direct fluorescent images of the chimeric lung after GFP+ hDASC transplantation. (a1) Mock-transplanted. (a2) Uninjured lung. (a3) GFP-labeling hDASCs transplanted. (b) Immunofluorescence images of the chimeric lung of anti-Lamin A/C (red) with DNA counterstain (DAPI, blue). Scale bar, 1000 μm . (c, d) Immunofluorescence images of the chimeric lung with GFP and human-specific Lamin A/C and hDASC marker KRT5 Abs. Scale bar, 200 μm . (e, f) Immunofluorescence images of the chimeric lung with human-specific Lamin A/C and AEC1 marker AQP5 and RAGE. Scale bar, 30 μm . (g) Immunofluorescence images of the chimeric lung with human-specific Lamin A/C and SCGB1A1. Scale bar, 50 μm .

comparable levels in control and experimental groups (Figures 3(c)–3(e)).

3.3. Evaluation of the Tumorigenic Potential of hDASC. To evaluate that whether the hDASCs were tumorigenic *in vitro*, we assessed the anchorage-independent growth potential of these cells. The data showed that human DASCs were unable to grow in soft agar medium, in contrast that mouse melanoma cells (B16) exhibited robust colony-forming efficiency under identical conditions (Figure 4(a)).

To confirm the tumorigenicity of human DASCs *in vivo*, cells were subcutaneously injected into NOD-SCID mice. The normal human fetal lung fibroblast cell line MRC-5 and cervical cancer cell line HeLa were also injected as the negative and positive controls, respectively. During the 16 weeks of the observation period, all mice implanted with HeLa cells that developed tumors at the injection site, including 4 mice and 6 mice in this group, were euthanized on day 70 and day 84, respectively, due to the chest compression from their large tumors. 8 mice (80%) in the hDASC-implanted group developed subcutaneous nodules with a spontaneous regression by the end of the observation period (Figure 4(b)). Mice with the nodules were sacrificed and histopathological examination confirmed that they were cyst lesions, but not tumors (Figure 4(c)). Altogether the above data indicated that human DASCs produced in the pharmaceutical-grade condition facilities under current protocol are nontumorigenic and safe to be tested in human patients.

3.4. Alveolar Regeneration by Intrapulmonary Transplantation of hDASCs. To determine whether cloned hDASCs could contribute to lung tissue regeneration *in vivo*, we labeled the cultured cells by GFP-expressing lentivirus and transplanted them into immune-deficient NOD-SCID mouse lungs. Bleomycin was intratracheally instilled to mouse lungs prior to the transplantation. 21 days after the cell transplantation, large-scale GFP+ cell incorporation

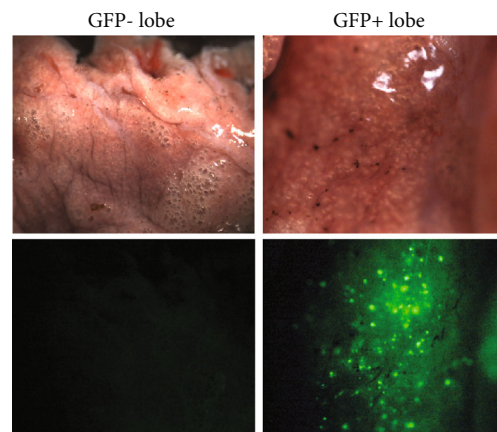


FIGURE 6: Bronchoscopic delivery of hDASCs into the macaque lung.

was observed in parenchymal areas of mouse lungs (Figure 5(a)). Meanwhile, lungs without bleomycin injury showed no incorporation of GFP+ cells posttransplantation, indicating that damage of the lung parenchyma is one of the prerequisites of exogenous hDASC incorporation (Figure 5(a)). After transplantation, the chimerism was further confirmed by human-specific Lamin A/C Ab costaining with GFP in mouse lungs (Figures 5(b) and 5(c)) [26]. The identity of KRT5 expression was also maintained in some engrafted cells 7 days posttransplantation (Figure 5(d)).

Next, we directly assessed the differentiation status of the hDASCs and their progeny by performing immunofluorescence detection of functional lung epithelial cells. 21 days posttransplantation, mature AEC1 markers AQP5 and RAGE [27, 28] were extensively expressed in engrafted human cells, which occupied bleomycin-denuded areas of existent alveoli and formed structures analogous to air sacs in the mouse lung parenchyma (Figures 5(e) and 5(f)). Since

AEC1s are the main functional cells that constitute the interface overlying the vascular endothelium essential for gas exchange, the above observations suggested that intratracheal delivery of exogenous hDASCs held potential as a strategy for lung function restoration. In addition, the engrafted cells could also incorporate into the bronchiolar region, where some of them gave rise to SCGB1A1+ Club cells (Figure 5(g)).

3.5. Bronchoscopic Delivery of hDASC into the Macaque Lung. To assess the safety and efficacy of the clinical cell delivery, human DASCs were transplanted into a nonhuman primate, cynomolgus macaque (*Macaca fascicularis*) pretreated with a single low dose of total body irradiation (3.2 Gy), causing immune suppression, such as neutropenia and lymphopenia. GFP-labelled DASCs, a total of 40 million cells suspended in PBS, were orthotopically infused into the macaque lung through bronchoscopy following clinical protocols. There was no obvious variety in weight and food-intake during the whole treatment. Also, vital signs and clinical observation of macaque all appeared normal. Seven days posttransplantation, macaque was euthanatized and all organs of it were harvested and the distribution of the GFP signal was monitored. The positive GFP+ cell signal scattered distributed in the transplanted lung lobe area was observed. No discernible GFP signal was detected under a fluorescence stereomicroscope in other organs/tissues such as the liver and kidney (Figure 6 and Table 1). DASC transplantation did not contribute to tumor development, aberrant cell growth, or other related adverse events, suggesting that DASC transplantation procedure might be safe in primates under the quantitative limitation of the rare subject.

4. Discussion

The lung, as one of the few organs exposed to the outside, is vulnerable to attack by pathogens, consequently triggering the progressive and inexorable destruction of oxygen exchange surfaces and airway, which is a major threat to human health. Recently, the outbreak of COVID-19, caused by the SARS-CoV-2 virus, has emerged, resulting in death primarily via respiratory failure [29–31]. It is hard to reconstruct the gas exchange surface and respiratory function by the means of current mitigating treatments. Given the scarcity of donor organs, as well as severe sides resulted from immune rejection, the application of lung transplant surgery is constrained [32]. Our previous studies demonstrated lung regeneration in mice following H1N1 influenza virus infection and bleomycin injury, involves distal airway stem cells expressing Trp63 (P63) and Keratin 5, called P63⁺/KRT5⁺ DASCs, to this process. Besides this, other adult lung-specific stem/progenitor cell lineages were also reported to hold great potential as cell therapy candidates, including SCGB1A1+SFTPC+ bronchioalveolar stem cells in the bronchioalveolar duct and SCGB1A1+ Club cells in trachea and upper airways and AEC2 in the alveolar bed [10, 12–15]. Compared with the relatively mature regeneration field, therapeutic potential of lung stem/progenitor cells will be more noteworthy in the future. Here, we only test the human

TABLE 1: Fluorescent examination of macaque organs.

Organs	GFP signal
Adrenal glands	NA
Aorta	NA
Bladder	NA
Bone and marrow (femur and sternum)	NA
Brain	NA
Epididymis	NA
Esophagus	NA
Eye and optic nerve	NA
Heart	NA
Kidney	NA
Lacrimal gland	NA
Large intestine (cecum, colon, and rectum)	NA
Larynx	NA
Liver	NA
Lung and bronchi	+
Mammary glands	NA
Pancreas	NA
Peyer patch	NA
Pituitary gland	NA
Prostate gland	NA
Salivary glands	NA
Sciatic nerve	NA
Skeletal muscles (biceps femoris)	NA
Skin (perimammary glands)	NA
Small intestine (duodenum, jejunum, and ileum)	NA
Spermathecal glands	NA
Spinal cord (cervical, thoracic, lumbar)	NA
Spleen	NA
Stomach (pancreatic stomach and nonpancreatic stomach)	NA
Submandibular and mesenteric lymph nodes	NA
Testes	NA
Thymus	NA
Thyroid and parathyroid glands	NA
Tongue	NA
Trachea	NA

DASCs as a targeted subject and highlight the remarkable generation stability and regenerative capacity of the cloned DASCs *in vitro*.

Stem cell therapy is an emerging therapeutic strategy, as an alternative therapeutical method of organ transplantation [33, 34]. Generally, the autologous cell is the best choice in transplantation, avoiding being attacked by immunocytes. An enormous number of human DASCs are needed in clinical transplantation, considering rare numbers of hDASCs *in vivo*; their extensive *in vitro* expansion is required. Whereas, such expansion raises simultaneously some risks such as genetic and epigenetic changes. Cell proliferation

in vitro could result in the occurrence of mutations and chromosomal aberrations, eventually leading to tumorigenicity. Thus, the safety and stability evaluation of expansion was elaborated *in vitro* and *in vivo*. Clones under the pharmaceutical-grade culture maintained their self-renewal, potency properties, and uniform identification *in vitro* amongst passages, which is crucial for cell quality control in further clinical application.

Immune-deficient mouse NOD-SCID and irradiated nonhuman primate cynomolgus macaque were the receptors of human DASCs to ameliorate the immunological rejection from disparate species. The chimeric of human-mouse lung indicates that hDASC pedigrees contributed multiple epithelial types, including AEC1 as well as bronchiolar secretory cells, to the regenerating distal lung, which is a general species-crossing repair manner following large-scale, acute lung damage. Moreover, an unconventional route of cell administration utilizing a portable fiberoptic bronchoscope in macaque was applied in the current study. Engraftment of hDASCs into macaque did not cause anaphylaxis or tumorigenic. Admittedly, only a relatively small number of macaque subject was used for the sake of animal welfare. Whether human DASCs could generate to the chimeric of the human-macaque lung would be the problem that we will address.

In summary, our data highlighted the hDASCs maintaining stem cell/progenitor properties during expansion *in vitro* under the pharmaceutical-grade condition as a candidate of cellular therapy. The chimeric of the human-mouse lung indicated hDASC pedigrees contributed multiple epithelial types, including AEC1 as well as bronchiolar secretory cells, to the regenerating distal lung.

Data Availability

The data used to support the findings of this study are available from the corresponding author upon request.

Conflicts of Interest

Regend Therapeutic Ltd. owns the patent and intelligence property interest related with this current work.

Acknowledgments

The authors gratefully thank Prof. Tao Ren for helping with the bronchoscopic procedure in macaque. A part of this work was funded by the Sino-German Bilateral Collaborative Grant in COVID-19-related research (C-0025 to W. Zuo), National Science Foundation of China (81770073 to W. Zuo), the National Key Research and Development Program of China (2017YFA0104600 to W. Zuo), Shanghai Science and Technology Talents Program (19QB1403100 to W. Zuo), Tongji University (Basic Scientific Research Interdisciplinary Fund and 985 Grant to W. Zuo), and Guangzhou Medical University annual grant to W. Zuo.

References

- [1] C. C. Hsia, D. M. Hyde, and E. R. Weibel, "Lung structure and the intrinsic challenges of gas exchange," *Comprehensive Physiology*, vol. 6, no. 2, pp. 827–895, 2016.
- [2] J. Sullivan, V. Pravosud, D. M. Mannino, K. Siegel, R. Choate, and T. Sullivan, "National and state estimates of COPD morbidity and mortality-United States, 2014-2015," *Chronic Obstructive Pulmonary Diseases: Journal of the COPD Foundation*, vol. 5, no. 4, pp. 324–333, 2018.
- [3] Y. Yan, W. I. Shin, Y. X. Pang et al., "The first 75 days of novel coronavirus (SARS-CoV-2) outbreak: recent advances, prevention, and treatment," *International Journal of Environmental Research and Public Health*, vol. 17, no. 7, p. 2323, 2020.
- [4] M. Zhou, H. Wang, X. Zeng et al., "Mortality, morbidity, and risk factors in China and its provinces, 1990-2017: a systematic analysis for the Global Burden of Disease Study 2017," *The Lancet*, vol. 394, no. 10204, pp. 1145–1158, 2019.
- [5] G. Bellani, J. G. Laffey, T. Pham et al., "Epidemiology, patterns of care, and mortality for patients with acute respiratory distress syndrome in intensive care units in 50 countries," *JAMA*, vol. 315, no. 8, pp. 788–800, 2016.
- [6] J. Hutchinson, A. Fogarty, R. Hubbard, and T. McKeever, "Global incidence and mortality of idiopathic pulmonary fibrosis: a systematic review," *The European Respiratory Journal*, vol. 46, no. 3, pp. 795–806, 2015.
- [7] P. Spagnolo, N. Sverzellati, G. Rossi et al., "Idiopathic pulmonary fibrosis: an update," *Annals of Medicine*, vol. 47, no. 1, pp. 15–27, 2015.
- [8] A. M. Menezes, R. Perez-Padilla, J. R. B. Jardim et al., "Chronic obstructive pulmonary disease in five Latin American cities (the PLATINO study): a prevalence study," *The Lancet*, vol. 366, no. 9500, pp. 1875–1881, 2005.
- [9] C. Wang, J. Xu, L. Yang et al., "Prevalence and risk factors of chronic obstructive pulmonary disease in China (the China Pulmonary Health [CPH] study): a national cross-sectional study," *The Lancet*, vol. 391, no. 10131, pp. 1706–1717, 2018.
- [10] C. E. Barkauskas, M. J. Cronic, C. R. Rackley et al., "Type 2 alveolar cells are stem cells in adult lung," *The Journal of Clinical Investigation*, vol. 123, no. 7, pp. 3025–3036, 2013.
- [11] P. A. Kumar, Y. Hu, Y. Yamamoto et al., "Distal airway stem cells yield alveoli *in vitro* and during lung regeneration following H1N1 influenza infection," *Cell*, vol. 147, no. 3, pp. 525–538, 2011.
- [12] J. L. McQualter, K. Yuen, B. Williams, and I. Bertoncello, "Evidence of an epithelial stem/progenitor cell hierarchy in the adult mouse lung," *Proceedings of the National Academy of Sciences of the United States of America*, vol. 107, no. 4, pp. 1414–1419, 2010.
- [13] J. R. Rock, C. E. Barkauskas, M. J. Cronic et al., "Multiple stromal populations contribute to pulmonary fibrosis without evidence for epithelial to mesenchymal transition," *Proceedings of the National Academy of Sciences of the United States of America*, vol. 108, no. 52, pp. E1475–E1483, 2011.
- [14] I. Salwig, B. Spitznagel, A. I. Vazquez-Armendariz et al., "Bronchioalveolar stem cells are a main source for regeneration of distal lung epithelium *in vivo*," *The EMBO Journal*, vol. 38, no. 12, 2019.
- [15] W. J. Zacharias, D. B. Frank, J. A. Zepp et al., "Regeneration of the lung alveolus by an evolutionarily conserved epithelial progenitor," *Nature*, vol. 555, no. 7695, pp. 251–255, 2018.

- [16] Q. Ma, Y. Ma, X. Dai et al., "Regeneration of functional alveoli by adult human SOX9⁺ airway basal cell transplantation," *Protein & Cell*, vol. 9, no. 3, pp. 267–282, 2018.
- [17] Y. Shi, M. Dong, Y. Zhou et al., "Distal airway stem cells ameliorate bleomycin-induced pulmonary fibrosis in mice," *Stem Cell Research & Therapy*, vol. 10, no. 1, p. 161, 2019.
- [18] Y. Wang, Y. Lu, Y. Wu et al., "Alveolar differentiation potency of human distal airway stem cells is associated with pulmonary pathological conditions," *Stem Cells International*, vol. 2019, 7123011 pages, 2019.
- [19] Y. Q. Zhou, Y. Shi, L. Yang et al., "Genetically engineered distal airway stem cell transplantation protects mice from pulmonary infection," *EMBO Molecular Medicine*, vol. 12, no. 1, article e10233, 2020.
- [20] W. Zuo, T. Zhang, D. Z. A. Wu et al., "p63⁺Krt5⁺ distal airway stem cells are essential for lung regeneration," *Nature*, vol. 517, no. 7536, pp. 616–620, 2015.
- [21] Z. Zhao, Y. Zhao, Y. Zhou, X. Wang, T. Zhang, and W. Zuo, "Single-cell analysis identified lung progenitor cells in COVID-19 patients," *Cell Proliferation*, vol. 53, no. 12, article e12931, 2020.
- [22] L. B. Ware and M. A. Matthay, "Keratinocyte and hepatocyte growth factors in the lung: roles in lung development, inflammation, and repair," *American Journal of Physiology. Lung Cellular and Molecular Physiology*, vol. 282, no. 5, pp. L924–L940, 2002.
- [23] S. Borowicz, M. van Scoyk, S. Avasarala et al., "The soft agar colony formation assay," *Journal of Visualized Experiments*, vol. 92, no. 92, article e51998, 2014.
- [24] A. M. Farese, M. V. Cohen, B. P. Katz et al., "A nonhuman primate model of the hematopoietic acute radiation syndrome plus medical management," *Health Physics*, vol. 103, no. 4, pp. 367–382, 2012.
- [25] A. E. Vaughan, A. N. Brumwell, Y. Xi et al., "Lineage-negative progenitors mobilize to regenerate lung epithelium after major injury," *Nature*, vol. 517, no. 7536, pp. 621–625, 2015.
- [26] A. Sanchez-Herrero, I. A. Calvo, M. Flandes-Iparraguirre et al., "Engineering a humanised niche to support human haematopoiesis in mice: novel opportunities in modelling cancer," *Cancers*, vol. 12, no. 8, p. 2205, 2020.
- [27] K. J. Travaglini, A. N. Nabhan, L. Penland et al., "A molecular cell atlas of the human lung from single-cell RNA sequencing," *Nature*, vol. 587, no. 7835, pp. 619–625, 2020.
- [28] X. Han, Z. Zhou, L. Fei et al., "Construction of a human cell landscape at single-cell level," *Nature*, vol. 581, no. 7808, pp. 303–309, 2020.
- [29] D. Wang, B. Hu, C. Hu et al., "Clinical characteristics of 138 hospitalized patients with 2019 novel coronavirus-infected pneumonia in Wuhan, China," *JAMA*, vol. 323, no. 11, pp. 1061–1069, 2020.
- [30] Q. Ruan, K. Yang, W. Wang, L. Jiang, and J. Song, "Clinical predictors of mortality due to COVID-19 based on an analysis of data of 150 patients from Wuhan, China," *Intensive Care Medicine*, vol. 46, no. 5, pp. 846–848, 2020.
- [31] A. Carfi, R. Bernabei, F. Landi, and for the Gemelli Against COVID-19 Post-Acute Care Study Group, "Persistent symptoms in patients after acute COVID-19," *JAMA*, vol. 324, no. 6, pp. 603–605, 2020.
- [32] F. Venuta and D. Van Raemdonck, "History of lung transplantation," *Journal of Thoracic Disease*, vol. 9, no. 12, pp. 5458–5471, 2017.
- [33] B. Lukomska, L. Stanaszek, E. Zuba-Surma, P. Legosz, S. Sarzynska, and K. Dreła, "Challenges and controversies in human mesenchymal stem cell therapy," *Stem Cells International*, vol. 2019, 9628510 pages, 2019.
- [34] S. Liu, J. Zhou, X. Zhang et al., "Strategies to optimize adult stem cell therapy for tissue regeneration," *International Journal of Molecular Sciences*, vol. 17, no. 6, p. 982, 2016.